DEVELOPMENT OF NANOSCALE BIOSENSORS FOR CANCER RELATED PROTEASES AND BLOOD-BORNE PATHOGENS BASED ON ELECTROCHEMICAL AND OPTICAL METHODS

by

LUXI ZHANG SWISHER

B.S., Northwest University, 2010

AN ABSTRACT OF A DISSERTATION

submitted in partial fulfillment of the requirements for the degree

DOCTOR OF PHILOSOPHY

Department of Chemistry
College of Arts and Sciences

KANSAS STATE UNIVERSITY
Manhattan, Kansas

2015

Abstract

A lot of materials exhibit novel properties when scaled down to nanoscale. Here we explore nanoelectrode arrays (NEAs) and nanoparticles in the application of high performance biosensors.

We have developed an electrochemical (EC) method for measuring the activity of proteases using vertically aligned carbon nanofiber (VACNF) NEAs. VACNFs were grown on conductive substrates and encapsulated in SiO_2 matrix. After polishing and plasma etching, controlled VACNF tips are exposed to form an embedded NEA. Tetrapeptides specific to cancer-mediated proteases are covalently attached to the exposed tip, with a ferrocene (Fc) moiety linked at the distal end. The redox signal of Fc can be measured with AC voltammetry (ACV) at ~1 kHz frequency, showing distinct properties from macro-electrodes due to VACNF's unique interior structure. The enhanced ACV properties enable the kinetic measurements of proteolytic cleavage of the surface-attached tetrapeptides by proteases. The well-defined regular VACNF NEAs by e-beam lithography show a much faster kinetics for cathepsin B proteolysis.

This EC method was further applied in whole lysate of human breast tissue and breast cells. The detected protease activity was found increased in cancer cells, with the metastatic cancer cell lysate showing the highest cathepsin B activity. The results indicated the potential of this technique as a portable multiplex electronic device for cancer diagnosis and treatment monitoring through rapid profiling of the activity of specific cancer-relevant proteases.

In another exploratory study, we modified nanoparticles with luminol and viral nucleic acid to develop chemiluminescence (CL) biosensors for blood-borne pathogens. Luminol-labeled 10-nm-diameter gold nanoparticles (GNPs) served as a nanocarrier for enhancing CL signal. The CL signal can be observed over 8 orders of magnitude variations in GNP concentration. Using

the same number of particles, luminol-labeled 30-nm-diameter latex beads showed ~3 orders of magnitude higher CL compared to 10-nm-diameter GNPs. Hybridization of target H1N1 nucleic acid on the latex beads and probe nucleic acid on the glass or optical fiber surface has been achieved. This assay will be incorporated into a simple hand-held device for routine assays in hospitals and clinics, or for large-scale screening of human populations as diagnostic tools to identify specific viral strains.

DEVELOPMENT OF NANOSCALE BIOSENSORS FOR CANCER RELATED PROTEASES AND BLOOD-BORNE PATHOGENS BASED ON ELECTROCHEMICAL AND OPTICAL METHODS

by

LUXI ZHANG SWISHER

B.S., Northwest University, 2010

A DISSERTATION

submitted in partial fulfillment of the requirements for the degree

DOCTOR OF PHILOSOPHY

Department of Chemistry
College of Arts and Sciences

KANSAS STATE UNIVERSITY
Manhattan, Kansas

2015

Approved by:

Major Professor
Dr. Jun Li

Copyright

Abstract

A lot of materials exhibit novel properties when scaled down to nanoscale. Here we explore nanoelectrode arrays (NEAs) and nanoparticles in the application of high performance biosensors.

We have developed an electrochemical (EC) method for measuring the activity of proteases using vertically aligned carbon nanofiber (VACNF) NEAs. VACNFs were grown on conductive substrates and encapsulated in SiO_2 matrix. After polishing and plasma etching, controlled VACNF tips are exposed to form an embedded NEA. Tetrapeptides specific to cancer-mediated proteases are covalently attached to the exposed tip, with a ferrocene (Fc) moiety linked at the distal end. The redox signal of Fc can be measured with AC voltammetry (ACV) at ~1 kHz frequency, showing distinct properties from macro-electrodes due to VACNF's unique interior structure. The enhanced ACV properties enable the kinetic measurements of proteolytic cleavage of the surface-attached tetrapeptides by proteases. The well-defined regular VACNF NEAs by e-beam lithography show a much faster kinetics for cathepsin B proteolysis.

This EC method was further applied in whole lysate of human breast tissue and breast cells. The detected protease activity was found increased in cancer cells, with the metastatic cancer cell lysate showing the highest cathepsin B activity. The results indicated the potential of this technique as a portable multiplex electronic device for cancer diagnosis and treatment monitoring through rapid profiling of the activity of specific cancer-relevant proteases.

In another exploratory study, we modified nanoparticles with luminol and viral nucleic acid to develop chemiluminescence (CL) biosensors for blood-borne pathogens. Luminol-labeled 10-nm-diameter gold nanoparticles (GNPs) served as a nanocarrier for enhancing CL signal. The CL signal can be observed over 8 orders of magnitude variations in GNP concentration. Using

the same number of particles, luminol-labeled 30-nm-diameter latex beads showed ~3 orders of magnitude higher CL compared to 10-nm-diameter GNPs. Hybridization of target H1N1 nucleic acid on the latex beads and probe nucleic acid on the glass or optical fiber surface has been achieved. This assay will be incorporated into a simple hand-held device for routine assays in hospitals and clinics, or for large-scale screening of human populations as diagnostic tools to identify specific viral strains.

Table of Contents

List of Figures

List of Tables

List of Abbreviations

ACV	Alternating Current Voltammetry
AIDS	Acquired Immune Deficiency Syndrome
APTES	3-Aminopropyl-Triethoxysilane
AEP	Asparaginyl Endopeptidase
ATR	Attenuated Total Reflectance
CL	Chemiluminescence
CNTs	Carbon Nanotubes
CNF	Carbon Nanofiber
CV	Cyclic Voltammetry
cDNA	Complementary DNA
DL	Detection Limit
DPV	Differential Pulse Voltammetry
DC	Direct Current
DTT	Dithiothreitol
DI	Deionized
DMF	Dimethylformamide
DNA	Deoxyribonuleic Acid
EIA	Enzyme Immunoassay
ELISA	Enzyme-Linked Immunosorbent Assay

EC	Electrochemical
EIS	Electrochemical Impedance Spectroscopy
ECM	Extracellular Matrix
EDC	1-ethyl-3-(3-dimethylaminopropyl)carbodiimide hydrochloride
FL	Fluorescence
FRET	Fluorescence Resonance Energy Transfer
Fc	Ferrocene
FWHM	Full Width at Half Maximum
FESEM	Field-Emission Scanning Electron Microscopy
GNPs	Gold Nanoparticles
GCE	Glassy Carbon Electrode
HA	Hemagglutinin
HIV	Human Immunodeficiency Virus
HGP	Human Genome Project
HPLC	High-Performance Liquid Chromatography
IP	Immunoprecipitation
IR	Infrared spectroscopy
LSPR	Localized Surface Plasmon Resonance
LUM	Luminol
MES	2-(4-Morpholino)ethane Sulfonic Acid

MMP-7	Matrix Metalloproteinase-7
MUA	Mercaptoundecanoic Acid
NEAs	Nanoelectrode Arrays
NEEs	Nanoelectrode Ensembles
PCR	Polymerase Chain Reaction
PECVD	Plasma Enhanced Chemical Vapor Deposition
PBS	Phosphate Buffer Saline
PMMA	Polymethyl-Methacrylate
PMT	Photomultiplier Tube
QDs	Quantum Dots
QCM	Quartz Crystal Microbalance
RT	Reverse Transcription
RNA	Ribonuleic Acid
RIA	Radioimmunoassay
RIE	Reactive Ion Etching
SPR	Surface Plasmon Resonance
SERS	Surface-Enhanced Raman Scattering
sulfo-NHS	1-Hydroxy-2,5-Dioxopyrrolidine-3-Sulfonic Acid Sodium Salt
TEOS	Tetraethyl Orthosilicate
TME	Tumor Microenvironment

VA	Vertically Aligned
WHO	World Health Organization
WCE	Whole Cell Extract
Z-Arg-Arg-AMC	Benzyloxycarbonyl-Arginine-Arginine-7-Amino-4-Methylcoumarin

Acknowledgements

First of all, I would like to thank my advisor, Dr. Jun Li, for his patience, understanding, and encouragement all the way through this long journey, and for pushing me further than I thought I could go.

I would also like to thank former and present members in Dr. Jun Li's group: Dr. Lateef Syed, Steven Klankowski, Foram Madiyar, Yiqun Yang, Emery Brown, Dr. Gaind Pandey, Tao Liu, Dr. Yifen Li, Yichen Zheng. Thanks Dr. Lateef Syed for guiding me in both projects of protease and chemiluminescence biosensor. Thanks Steven Klankowski for helping me on SEM images and carbon nanofiber growth. Thanks the help from Foram Madiyar in the nanoelectrode fabrication and for the great support and encouragement as a friend.

I express my gratitude to my supervisory committee Professors Duy Hua, Daniel Higgins, Annelise Nguyen (former committee) for the guidance and help on my doctoral program. I am also thankful to Professor Anna Zolkiewska to serve in my supervisory committee in my last year and Professor Peying Fong to serve as an outside chair in my final defense exam.

I would also like to thank Professor Duy Hua, Dr. Allan Pior and Professor Annelise Nguyen for the great assistance and discussion on protease biosensor project. Thanks Professor Judy Wu, Professor Mark Richter, Dr. Jianwei Liu, Cas LeMaster and Caleb Christianson for the valuable discussion and help on chemiluminescence biosensor project.

Special thanks to Professor Dan Boyle from biology department for helping me to complete SEM/TEM course after I was back from maternity leave.

I would also like to thank Kansas State University and chemistry department for giving me a chance to become one of the proud K-Staters and providing me financial support as a graduate teaching assistant.

I am also grateful for the staffs in the chemistry department who have given me great assistance: Ron Jackson, Leila Maurmann, Tobe Eggers, Michael Hinton, Earline Dikeman (former lab instructor), Tingting Liu, Mary Dooley and Kim Ross.

I would like to acknowledge doctoral research fellowship (2014-2015) from Kansas State University Research Foundation (KSURF), and financial support from National Cancer Institute (R15CA159250-01), Terry C. Johnson Center for Basic Cancer Research at KSU and Institute of Advanced Medical Innovation (IAMI) at University of Kansas.

Finally, I would like to give thanks to my family for their unconditional love and support. Without my parents' love, guidance and discipline, I would have no chance to go this far. Special thanks to my husband, Andrew Swisher and daughter Lili. Thank you for making my days brighter.

Dedication

“To my wonderful husband Andrew and daughter Lili”

Preface

This dissertation consists of the following major sections:

Chapter 1 – A brief introduction of the principle of biosensors and the use of nanoscale materials for biosensing application. Some traditional biosensing techniques for proteases and DNA detection are discussed. This forms the basis and motivation to develop protease and DNA biosensor based on nanomaterials.

Chapter 2 – A brief description of the procedures of the fabrication and characterization of vertically aligned carbon nanofiber (VACNF) nanoelectrode arrays (NEAs). General experimental details for protease detection are also described.

Chapter 3 – An accepted paper, published in *Journal of Physical Chemistry C*[1]. This chapter demonstrates that high-frequency ACV can be applied on embedded VACNF NEAs to measure the redox reaction of Fc attached to the exposed CNF tip through a tetrapeptide and a linker molecule. The kinetics of proteolysis of the surface-attached peptides by cancer-related proteases, legumain and cathepsin B, is measured and analyzed with a heterogeneous Michaelis-Menten model to derive the "specificity constant" k_{cat}/K_m. This is the first example of the use of VACNF NEAs on protease activity study. The study demonstrates that these VACNF NEA based electrochemical enzymatic biosensors can be potentially developed into portable multiplex electronic devices for rapid cancer diagnosis and treatment monitoring.

Chapter 4 – An accepted paper, published in *Biosensors and Bioelectronics*[2]. This chapter further investigates the kinetics of cathepsin B activity in complex tissue lysates. A normalization algorithm is introduced to extract the proteolysis signal from the largely varied raw data, which enabled the consistent comparison of the results from the kinetic study. Moreover, the study of using regular VACNF NEAs fabricated with precise e-beam lithography

exhibits faster kinetics of cathepsin B proteolysis, illustrating the potential for further improving detection sensitivity by using this EC technique.

Chapter 5 – A manuscript submitted to *Nanomedicine: nanotechnology, biology and medicine*. This chapter brings the application of EC biosensor based on VACNF NEAs to a further stage – study of cathepsin B activity in breast cell lysates and the specificity study by using cathepsin B inhibitor GC-373. It is illustrated that this EC method is a reliable tool to measure the proteolytic kinetics and quantify the protease activity in complex breast cell lysates. The activity of cathepsin B was found to increase from normal to cancer cell lysates. Moreover, the clear inhibition effects by GC-373 compound indicate that this method may also be used as an effective technique for inhibitor screening in the complex biological samples.

Chapter 6 – Part of the content of this chapter is from an accepted paper, published in *Analyst*[3]. This chapter discusses the development of ultrasensitive blood-borne pathogen biosensor based on nanoparticles using chemiluminecence (CL) method. It describes the methods of modification of gold nanoparticles and latex beads with luminol and/or viral nucleic acid and the immobilization of nanoparticles on the optical fibers through nucleic acid hybridization. CL measurements are conducted by commercial luminometer in 96-well plates. This work explores a new biosensor direction for future studies.

Finally, chapter 7 summarizes the major findings of the work and discusses the future direction for both the EC protease biosensor and CL pathogen biosensor.

Chapter 1 - Introduction

1.1 Principles and significance of biosensors

Principles

Biosensors are analytical devices incorporating a biological sensing element connected to physicochemical transducers that generate measureable signals proportional to the concentration of a specific chemical or a set of chemicals (Figure 1.1).[4-9] Based on the type of the receptor, biosensors can be classified as enzymatic biosensors, genosensors, immunosensors, etc. Biosensors can also be divided into several categories according to the type of the transducer. Three of the most common transduction principles for sensing include mass, electrochemical and optical detection. Mass biosensor can produce a signal depending on the mass of the chemicals that interact with the sensing film. Piezoelectric biosensor is the most common sensor in this class, which is based on that the resonant frequency of an oscillating piezoelectric crystal can be affected by a small change in mass at the crystal surface.[10] Electrochemical (EC) sensor is to use electrodes to measure the electrochemical changes that occur when chemicals interact with the sensing surface. Transduction of the chemical signal into an electrical signal can be done by amperometry, voltammetry, potentiometry, impedance spectroscopy etc. Optical sensors often involve optical fibers to direct light to the sensing film. The optical signals can be absorbance, fluorescence (FL), chemiluminescence (CL), surface plasmon resonance or light reflectivity. For biosensor development, there are a number of aspects to be considered, such as the generation of transduction signal (increase of signal, decrease of noise, etc.), sensor design (sample injection and drainage, reduction of sample consumption, reduction in detection time, etc.), surface immobilization (analyte binding efficiency, elimination of non-specific binding, etc.), binding

format (direct binding, sandwich-type binding, etc.), and data analysis (extraction of information regarding analyte concentration, binding kinetics, etc.).[11]

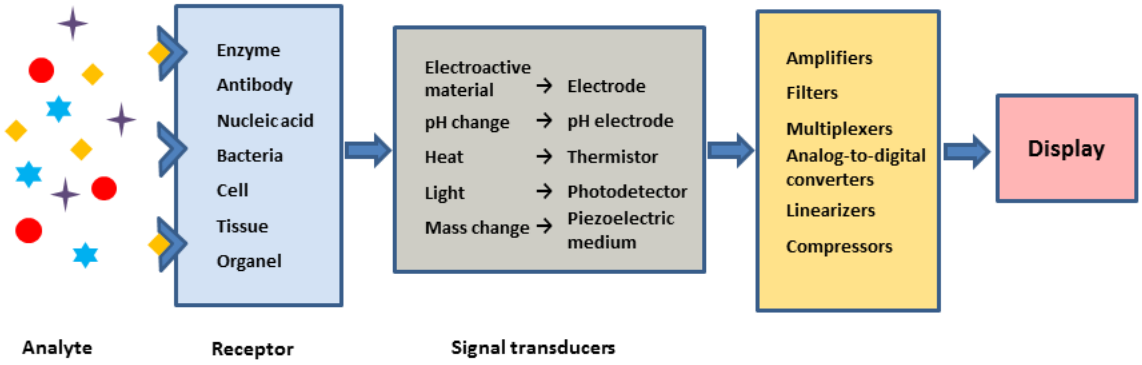

Figure 1.1 Schematic showing the principle and main components of a biosensor.

To characterize the sensor performance, sensitivity, detection limit (DL) and linear concentration range are important parameters to consider. Sensitivity is defined as the change of the magnitude of the sensor transduction signal in response to the change of the analyte.[11] DL can be deduced by the ratio of the noise in the transduction signal and the sensitivity. It is usually desired to increase sensitivity and decrease DL as much as possible. Finally, the linear concentration range is determined by the lower and upper limits of the quantification.

The recent development in nanotechnology has generated a number of new materials and devices that have desirable properties and useful functions for numerous biosensor applications.[12-15] Various kinds of nanomaterials, such as carbon nanotubes (CNTs)[16-18], gold nanoparticles (GNPs)[19-20], magnetic nanoparticles[21] and quantum dots[22-23] have been broadly applied in biosensor development due to their unique physical, chemical, mechanical, optical and magnetic properties. The high surface to volume ratio of nanomaterials commonly leads to remarkable enhancement of sensitivity and specificity of the detection.

Significance

Although great advances have been made against cancer, in 2012 alone, 8.2 million people worldwide died of cancer.[24] This number will rise to 14.6 million cancer deaths in 2035 if no significant advances in cancer prevention, detection, and treatment is made.[25] Cancer is also one of the costliest diseases globally. It has been estimated that 13.3 million new cases of cancer in 2010 have cost $290 billion worldwide. Thus, there is an urgent need for more efficient and economic prevention and treatment approaches due to the increasingly economic and personal burden of cancer. Regarding cancer research, biosensors have been intensively studied and found in many applications in early diagnosis and screening of cancers. For example, Yuan et al. reported clinical diagnostic application of the localized surface plasmon resonance (LSPR) biosensor in ovarian cancer. The results of detection of biomarker human epididymis secretory protein 4 demonstrated that this LSPR biosensor can serve as an effective alternative for the clinical serological diagnosis of ovarian cancer with fast detection speed, good specificity, effective reproducibility and long-term stability.[26] Jin et al. developed an EC biosensor based on label-free graphene for detection of cancer biomarker and carcinoembryonic antigen.[27] The high sensitivity, good specificity, ease of fabrication and operation plus the short analysis time make this EC biosensor a promising candidate for the clinical diagnosis of cancer.

Blood-borne pathogens are microorganisms such as viruses or bacteria in human blood or body fluids that cause disease in people. The most common ones are hepatitis B, hepatitis C and human immunodeficiency virus (HIV) which causes acquired immune deficiency syndrome (AIDS). In 2009, close to 2 million people died from AIDS worldwide and the epidemic continues to grow rapidly. The United Nations' UNAIDS office and World Health Organization (WHO) estimate that in certain areas of Africa over 33% of adults are living with HIV. Millions

of children have been orphaned in Africa due to the epidemic. More than 34 million people worldwide are infected with HIV. The epidemic is also spreading rapidly in Eastern Europe and Asia.[28] Hepatitis C virus can cause hepatitis C, a liver disease. 130-150 million people globally are diagnosed with chronic hepatitis C infection. 350,000 to 500,000 people die each year worldwide due to hepatitis C-related liver diseases. Unlike hepatitis B disease, there is currently no vaccine for hepatitis C.[29] Early and accurate diagnosis of those diseases is critical in increasing the survival rate and enhancing patients' life quality. Various biosensing techniques for blood-borne pathogens detection with high sensitivity have been extensively studied and successfully applied. Based on antigen/antibody-binding affinity, there are pathogen sensing techniques such as enzyme immunoassay (EIA)[30] and enzyme-linked immunosorbent assay (ELISA)[31]. Pathogens can also be detected through their unique nucleic acid chain, such as deoxyribonuleic acid (DNA) and ribonuleic acid (RNA). DNA sensing methods include polymerase chain reaction (PCR) and DNA microarray.[32] Depending on the type of the output signal, DNA microarray can also be classified into several categories, such as fluorescence and colorimetric methods, Raman spectroscopy[33], electrochemical method[14], SPR spectroscopy[34] etc. Electrochemical biosensor for rapid, convenient and cost-effective pathogen detection has also been reported.[35] Both immunoassay and nucleic acid hybridization can be applied on electrochemical platforms.

1.2 Nanoscale materials for biosensing: advantages and challenges

When scaled down to nanoscale, a lot of materials exhibit novel properties which cannot be extrapolated from their bulk behavior.[36] In recent years, with the development of nanotechnology and the discovery of the nanomaterials with novel properties, the application of nanoscale materials in biosensor field has advanced greatly. For example, gold nanoparticles

(GNPs) have strong absorption of the incident light in the UV-vis range when the amplitude of electron oscillation around the particle surface reaches maximum at a specific frequency– an unique phenomenon called surface plasmon resonance (SPR).[37] SPR frequency can be affected by the size and shape of nanoparticles, surface charges, dielectric constant of surrounding medium etc. SPR biosensors based on GNPs are one of the most advanced label-free optical biosensor technologies and have great potentials in numerous fields, such as environmental monitoring, disease diagnosis and food safety.[38-39] GNPs are also biocompatible with biomolecules, thus greatly increasing the number of biomolecules immobilized on the surface of electrodes, leading to the enhancement of sensitivity.[40] Another example of successfully applying nanomaterial into biosensing field is carbon nanotubes (CNTs) based bionsensors. Since the discovery in 1991, CNTs have attracted extensive interest due to their unique structural, mechanical, electrical and chemical properties. CNTs are able to mediate fast electron-transfer kinetics for numerous electroactive species, such as hydrogen peroxide[41], NADH[42-43], cytochrome c[44], ascorbic acid[45] etc. In addition, the large length-to-diameter ratios of CNTs provide high surface-to-volume ratios. Moreover, the results from cell culture of neural cells on carbon nanofiber (CNF) arrays (one type of CNTs) showed the great potential of such nanostructured materials as a 3D interface between the neural tissues and solid-state electronics due to their superior chemical, electrical and mechanical properties.[46] Recently, Syed et al. discovered that electrochemical signal on VACNF nanoelectrode arrays (NEAs) can be greatly improved by using alternating current voltammetry (ACV) due to the unique conically stacked graphitic structure of CNFs which opened a new capacitive pathway for AC current.[47] CNF NEAs with enhanced performance using ACV have later been successfully applied in the quantification of the activity of a cancer related protease, cathepsin B, in complex cell lysates.[1-2]

However, like any emerging field, application of nanomaterials for biosensing is facing many challenges. For example, mechanism of some interaction between biomolecules and nanomaterials still need to be clarified. Due to the special structures and functions that biological molecules possess, how to fully use them to fabricate single molecules multifunctional nanocomposites or nanoelectrode remains as a great challenge. How to enhance the sensitivity and specificity, and realize miniaturization and multiplexing are also challenging. Future work should focus on clarifying the mechanism of interaction between biomolecules and nanomaterials on the surface of electrodes, developing multiplexing system and looking for novel properties to fabricate new generations of biosensors. Nevertheless, nanomaterials-based biosensors have shown prospective properties and will find broader application in food analysis, clinical diagnosis and environmental monitoring in the near future.

1.3 Biosensors for protease detection

1.3.1 Significance

Proteases are ubiquitous in living organisms and regulate a multitude of biological processes.[48-50] In living systems, the unbalance of protease and their inhibitors leads to many diseases such as cancer. Throughout cancer progression, all five classes of protease are involved, which are serine (e.g. urokinase-type plasminogen activator, plasmin, chymase), cysteine (e.g. cathepsin B, L, S, K, Q; caspases; bleomycin hydrolase), aspartate (e.g. cathepsin D and E), threonine (e.g. proteasome) and matrix metalloproteases (e.g. gelatinases A and B, meprin).[49, 51] It is found that proteases are not only expressed by cancer cells, but also found in non-neoplastic neighboring cells which are enslaved to promote tumor growth and invasion.[52-53] Numerous data have demonstrated the role of proteases in promoting tumor growth and progression (Figure 1.2).[49, 52] For example, increased expression and/or activities of cathepsin B was found to

associate with many types of cancers, such as breast[54], colorectal[55], gastric[56], lung[57] and prostate[58] carcinomas. Trypsin, one of the well-known digestive serine protease, has been found to be involved in cancer development and facilitating cancer proliferation, invasion and metastasis.[59-60] Proteases involvement in cancer suggests that they can be useful markers for identifying patients who are suffering from cancer. Thus, there is an urgent need for the development of effective biosensors for protease detection in early diagnosis and treatment monitoring of cancers.

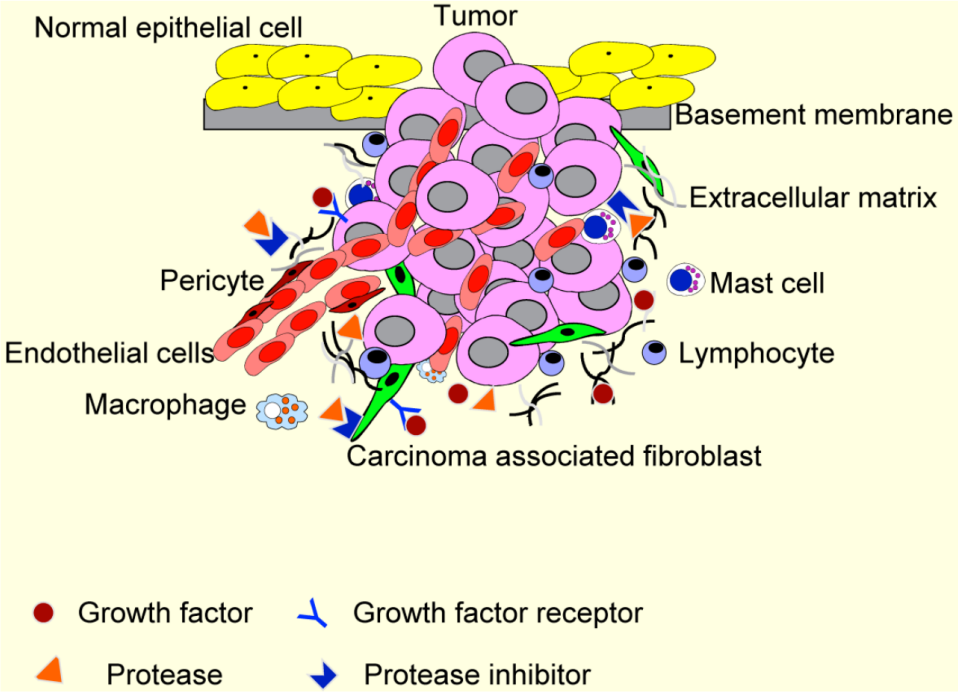

Figure 1.2 The tumor microenvironment (TME). TME comprises different stromal cells in addition to tumor cells. These include vascular or lymphatic endothelial cells, supporting pericytes, fibroblasts, and both innate and adaptive infiltrating immune cells. Moreover, TME contains non-cellular components, including extracellular matrixes, growth factors, proteases, protease inhibitors and other signaling molecules that play important roles in stromal reactions in TME.[52] (Adapted with permission from ref. 52. Copyright © 2013 Ivyspring International Publisher. License link: http://creativecommons.org/licenses/by-nc-nd/4.0/legalcode)

1.3.2 Traditional detection methods for proteases

Traditional methods for protease detection include FL method[61-62], EC method[1-2, 63-65], SPR[66], colorimetric assay[67], ELISA[68], reverse transcription (RT) PCR[69] and high-performance liquid chromatography (HPLC)-MS[70] etc.

With the advance of studying proteolytic process by genomic and proteomic approaches, short peptide substrates for many kinds of proteases have been identified, thus facilitating rapid and facile methods to study the activities of the corresponding proteases.[62, 71-72] By attaching peptide substrates with appropriate reporters, such as FL and bioluminescence, the proteolytic activity of the corresponding proteases can be studied.[73-74] For example, highly selective fluorogenic substrate benzyloxycarbonyl-Arginine-Arginine-7-amino-4-methylcoumarin (Z-Arg-Arg-AMC) has been used to study cathepsin B activity in a 96 well plate.[75] The cleavage between arginine and AMC dye by cathepsin B results in the increase of the fluorescence which was recorded by a fluorescence microplate reader in kinetic mode. In this way, proteolytic activity of cathepsin B can be studied. Another common fluorescent method to assay the protease is based on fluorescence resonance energy transfer (FRET) where two fluorescent molecules are attached to each end of the substrate peptide with a distance less than 10 nm. The excited state donor molecule may transfer energy to an acceptor molecule through nonradiative dipole-dipole coupling.[76] The efficiency of the energy transfer is inversely proportional to the sixth power of the distance between the donor and the acceptor.[77] The energy transfer is disrupted by the cleavage of the peptide substrate by the protease, thus leading to the ratio change of the fluorescence from the donor and the acceptor, or the increase of the fluorescence if the acceptor is a quencher (Figure 1.3a).[62] However, the energy transfer is often hindered by cross-talk between two fluorescent proteins with narrow Strokes shift and the process of genetically

engineered cell lines to express the fluorescence protein is very tedious.[62] Compared to organic dyes and fluorescent proteins, quantum dots (QDs) have superior photophysical properties, such as broad absorption spectra with large molar extinction coefficients at wavelengths from the UV to the visible[78-80], size-dependent emission band spanning from UV to infrared[81-82], excellent photostability and high quantum yield[83-84]. In FRET system, fluorophore or quencher is used in conjunction with QDs (Figure 1.3b). Energy acceptor groups (fluorophore or quencher) were bound to the surface of the QD through a peptide sequence which leads to quenching of the QD emission via FRET. The cleavage of the peptide sequence due to protease activity results in the recovery of the QD fluorescence.[85-86]

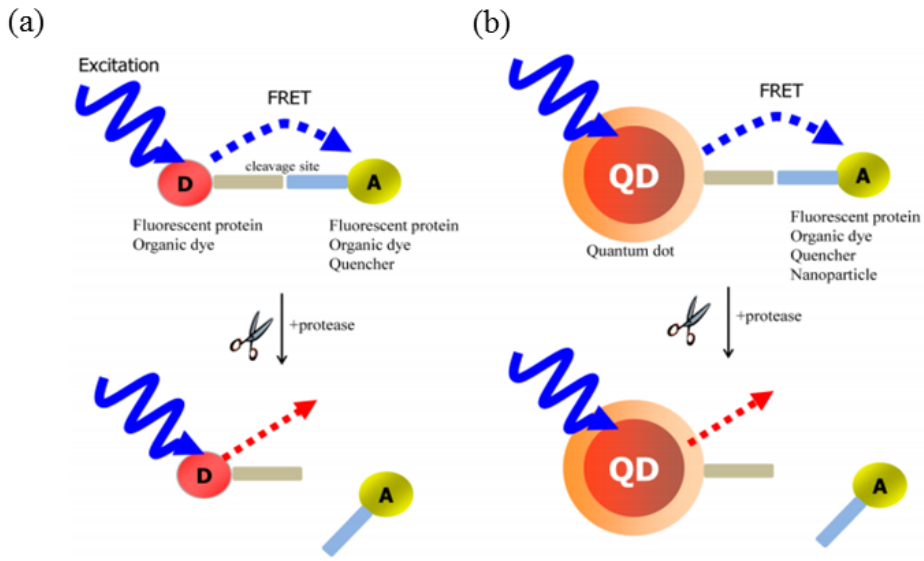

Figure 1.3 Schematic of FRET-based probe for the detection of protease activity. (a) Conventional FRET. (b) QD-based FRET. D and A indicate energy donor and energy acceptor.[62] (Adapted with permission from ref. 62. Copyright © 2012, Ivyspring International Publisher. License link: http://creativecommons.org/licenses/by-nc-nd/4.0/legalcode)

Common EC methods to monitor protease activity include cyclic voltammetry (CV), electrochemical impedance spectroscopy (EIS), differential pulse voltammetry (DPV) and

amperometry. For CV, DPV and amperometry, the redox species-labeled peptide chain was often used. For example, the interaction between ferrocene (Fc)-labeled peptide on the gold electrode and proteolytic enzymes trypsin and α-thrombin was investigated by CV (figure 1.4).[64] Oxidation of the Fc head gave rise to a current passing through the electrode, which was used as a signal reporter for the labeled peptide. The protease activity can be detected by monitoring the loss of the Fc label due to the cleavage of the peptide chain by the proteolytic enzymes. EIS is another common EC method to study protease activity. It is used to characterize the electrode processes and complex interfaces by studying the system response to the application of a periodic small amplitude ac signal. Mahmoud et al. utilized EIS to trace the alteration of the interfacial properties of the electrode due to the interaction between HIV-1 protease and Fc-pepstatin conjugate.[65] The binding of HIV-1 protease to the Fc-pepstatin/carbon nanotube/gold nanoparticle modified electrode surface increased the film thickness, resulting in an increase of the resistance to charge transfer. Our group recently reported detection of cathepsin B proteolytic activity using Fc-labeled tetrapeptide by ACV on vertically aligned (VA) CNFs fabricated NEAs.[1-2] This design enables the use of high AC frequencies (~1 kHz) with enhanced EC signals. The proteolysis of the Fc-tetrapeptide by cathepsin B produces decay in the ACV peak current versus the reaction time. The exponential component of the data can be quantitatively analyzed using a heterogeneous Michaelis-Menten model.[2] Compared to the optical methods, EC approaches are much simple and avoid specific synthesis of FL labels and sophisticated instrumentations.

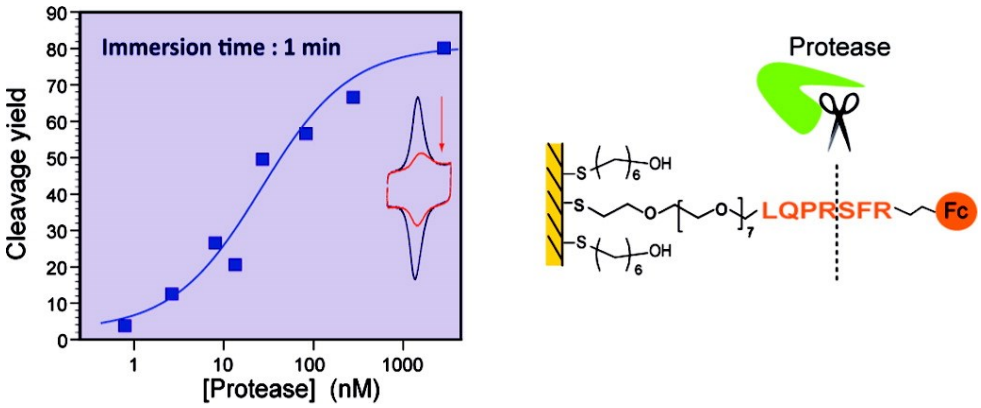

Figure 1.4 Schematic representation of the EC system for the detection of thrombin activity.[64] (Adapted with permission from ref. 64. Copyright © 2010, American Chemical Society.)

Other than FL and EC methods, ELISA and RT-PCR are also commonly used approaches in molecular biology to detect proteases or their mRNA in the fluids. For ELISA, the basic immunology concept of an antigen binding to its specific antibody was used, which allows detection of small quantities of antigens such as proteins, antibody and peptides in the fluid.[87] Taking sandwich type ELISA as an example, the surface is bound with the capture antibody and the protease-containing sample is then added to generate protease binding to the capture antibody. After removing unbound protease, the detecting antibody is added, and binds to a different epitope of the protease. Following that, enzyme-linked secondary antibody is added and binds to the detecting antibody. Finally, the substrate is added, which is converted by the enzyme into a product with a specific color or fluorescent signal. The absorbance or fluorescence signal is measured to determine the quantity of the protease. However, the cross-reactivity might occur with the secondary antibody, leading to false positive results. For RT-PCR, it allows the detection and quantification of mRNA corresponding to the protease and is the most sensitive technique for RNA detection currently available. In RT-PCR, using a reverse transcriptase, the RNA template is first converted into a complementary DNA (cDNA) which is then used as a

template for exponential amplification using PCR. However, RT-PCR is only a semi-quantitative method for determining the mRNA levels of the proteases.[69] In addition, both RT-PCR and ELISA are time-consuming and involve costly instruments. Beyond that, it is not possible to achieve real-time monitoring of protease activity with such methods. HPLC has also been used as a common chemical analysis method to study the proteolysis reactions, but is subjected to similar time and cost constraints.[70]

1.4 Biosensors for DNA detection

DNA is a molecule that encodes the genetic information to instruct the development and function of all living organisms and many viruses.[88] The nucleotide unit consists of nitrogen-containing four different nucleobases (G-guanine, A-adenine, T-thymine or C-cytosine), deoxyribose and a phosphate group. The detection of DNA base sequence or DNA sequencing is critical for disease diagnosis (such as blood-borne pathogen detection), environmental testing for bacterial contamination, forensic analysis, genetic prognosis of disease progress and responses to drug treatment, etc.

Techniques for DNA detection fall into two categories, PCR and DNA microarray. Depending on the type of output signal, different detection approaches have been used in DNA microarray technique, such as raman spectroscopy[33], EC method[14], SPR spectroscopy[34], quartz crystal microbalance (QCM) technique, FL and colorimetric methods. A number of them are combined with GNPs and other nano-structured materials in order to amplify the signal and improve the sensitivity of DNA detection.

PCR enables to produce millions of copies of a specific DNA sequence within hours for molecular and genetic analyses. Most mapping techniques in the Human Genome Project (HGP) relied on PCR. PCR can be applied in DNA fingerprinting/profiling and detection of bacteria or

viruses. General procedure of PCR can be divided into three steps. First, double-stranded DNA is separated at temperatures above 90 °C. Second, oligonucleotide primers are annealed at 50-60 °C. Finally, optimal primer extension occurs at 70-78 °C under the catalysis by DNA polymerases. Once an adequate amount of DNA has been produced with PCR, the sequence of nucleotide pairs in the DNA can be determined by using various biomolecular sequencing methods such as enzymic polymerization[89-90], chemical methods based on DNA degradation[91-92], the Pyrosequencing method[93-95] (DNA sequencing in real time by the detection of released pyrophosphate) and single molecule sequencing with exonuclease[96-97]. Real-time PCR, in which amplified DNA is detected as the reaction progresses in real time, has become more and more popular compared to conventional PCR due to its high speed, high sensitivity, good reproducibility and minimal carryover contamination leading to false-positives.[98]

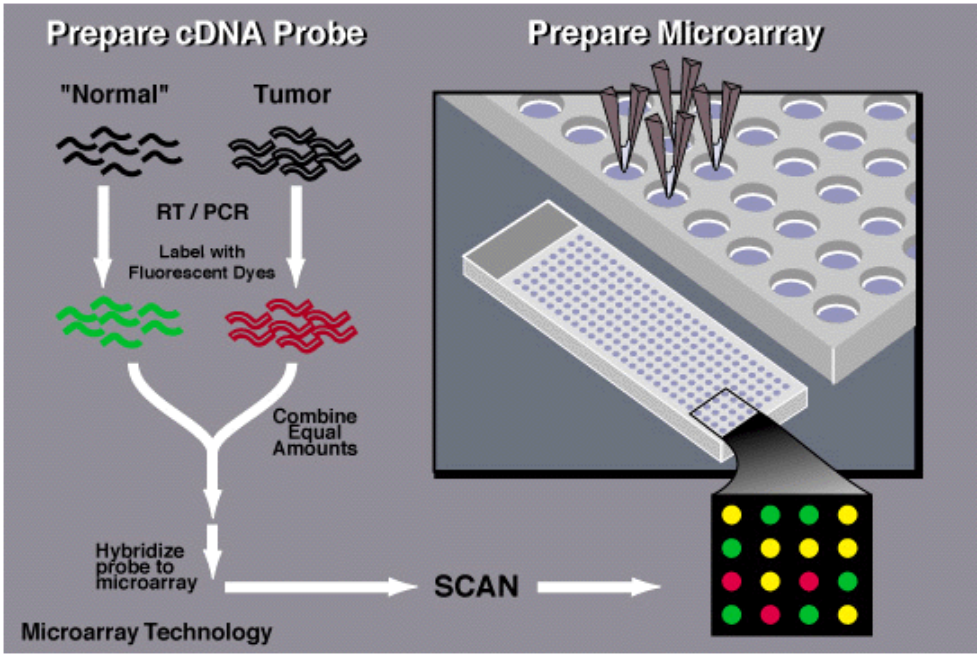

Figure 1.5 Schematic illustration of DNA microarray technology based on FL method. (Courtesy: National Human Genome Research Institute. http://www.genome.gov/10000533)

DNA detection can also be achieved by using DNA microarray technique. Thousands of spotted samples, such as DNA, cDNA and oligonucleotides, are arrayed in orderly rows and columns on a solid support (usually a microscope glass slide). This allows determining thousands of complementary binding of unknown DNA sequences at once. There are many ways to realize the event of complementary binding. The most common way is to rely on FL method, in which unknown DNA sequences are labeled with FL dye (Figure 1.5). As shown in figure 1.5, When co-hybridizing tumor samples (red dye) and normal sample (green dye), they will compete for the spotted synthetic DNAs on the microarray slide. If the spot is red, this means that the specific gene is more expressed in tumor than in normal. The spot is green which means the gene is more expressed in the normal tissue. If the spot is yellow, that means the gene is equally expressed in both normal and tumor tissue.

Raman spectroscopy is another method to detect DNA. Raman spectroscopy provides the information of molecular vibration that is used to identify and quantify the sample. This technique involves shining a monochromatic light source such as laser on the sample and detecting the scattered light. The light interacts with molecular vibrations in the system, resulting in the shift of the photon energy. The shift gives information about the vibration mode of the system. For example, Cao et al. reported multiplexed detection of oligonucleotide targets by GNP probe labeled with oligonucleotides and Raman-active dyes, Cy3.[33] A chip was spotted with 15-nucleotide capture strands which hybridized with 30-nucleotide target sequence. The chip was then treated with nanoparticle probes to hybridize with the overhanging region of the target sequence (Figure 1.6). Finally, the chip was treated with a Ag enhancement solution and studied by a Raman spectrometer. The Ag particles grew around the Cy3-labeled nanoparticle probes, resulting in large Ramen scattering enhancements. The Raman scattering signals are

caused exclusively by the Cy3 dye molecules immobilized on the particles and the scattering frequency for each Raman line remains constant. The reliable surface-enhanced Raman scattering (SERS) signals from the Cy3-labeled nanoparticle probes allow using the Raman spectrum of Cy3 as a spectroscopic fingerprint to detect the target oligonucleotide strand. It was claimed that the detection limit of this method was 20 femtomolar. Compared to the traditional FL detection method, this nanoparticle-based Raman technology has several advantages, such as more selection of non-overlapping probes, higher multiplexing capabilities and higher sensitivities due to GNPs labeling.

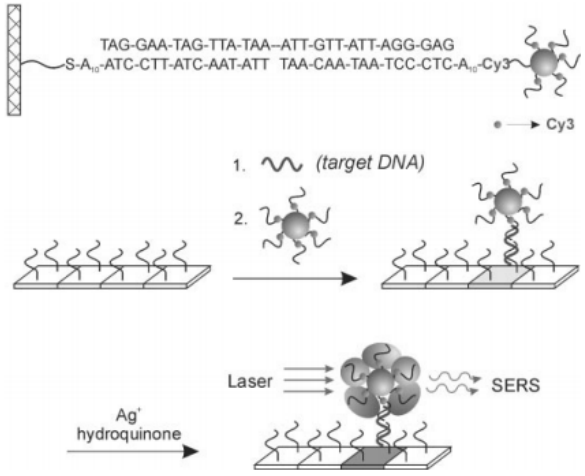

Figure 1.6 The schematic of a three-component sandwich assay for DNA detection using SERS spectroscopy.[33] (Adapted with permission from ref. 33. Copyright © 2002, the American Association for the Advancement of Science.)

EC methods have received considerable attention in recent years in the development of DNA biosensors due to their high sensitivity, low cost, ease to be developed as portable system and on-site monitoring.[99-102] The strategies of EC signaling are based on the oxidation of DNA bases, the redox reactions of reporter molecules on the electrode surface by specific DNA probe-target interactions and by charge transport reactions mediated by π-stacked base pairs. The

earliest EC DNA detection was based on the oxidation and reduction of DNA at a hanging mercury drop electrode.[103] The amount of DNA can be simply reflected by the amount of DNA reduced or oxidized. The methods to oxidize target DNA indirectly have also been explored. Polypyridyl complexes of Ru(II) or Os(II) to mediate the EC oxidation of guanine is often used. For example, Li et al. reported ultrasensitive DNA detection based on VACNF NEAs using CV and ACV.[104] Oligonucleotide probes were selectively functionalized to the open edges of the nanotubes. Since small guanine oxidation peak cannot be resolved by CV measurement due to the high background at potentials above +0.90V, $Ru(bpy)_3^{2+}$ was used to provide amplified signal for DNA detection (figure 1.7). A detection limit of subattomole oligonucleotide targets was achieved by this EC system. EC method has been proven to be a fast, cheap and simple solution for molecular diagnosis, particularly for point-of-care and field application.

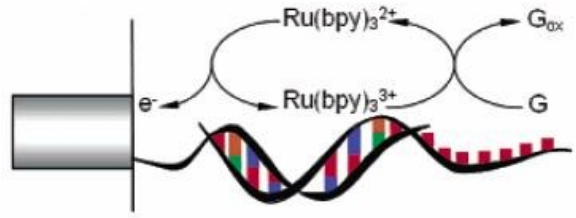

Figure 1.7 The schematic mechanism of $Ru(bpy)_3^{2+}$ mediated guanine oxidation on the DNA attached electrode surface.[104] (Adapted with permission from ref. 104. Copyright © 2003, American Chemical Society.)

SPR technique has been also applied in DNA microarray detection. SPR is an optical technique that measures the changes in the refractive index of the medium near a noble metal surface (within 200 nm).[105-107] The typical sensing surface is a thin film of gold deposited on a glass substrate that forms the floor of a small volume flow cell where an aqueous solution is

passed. The receptor molecule is usually immobilized on the sensing surface and the analytes are injected into the aqueous solution through the flow cell. Monochromatic, p-polarized light is reflected from the back of the glass-gold interface. The reflected light beam is monitored as the reaction occurs at the interface of gold film and solution.[34] Thus, SPR is a highly sensitive method for label-free detection of the interactions of biomolecules. By coating the SPR sensing surface with probe DNA, this technique can be used for the study of affinity binding and detection of DNA target in the sample solution. For example, Kick et al. deposited thiol-modified signal-stranded probe DNA on the gold surface of the microchip and investigated the effect of different parameters on hybridization by means of SPR spectroscopy. A detection limit of 0.5 ng/μL (2.6 nM) was achieved in this study.[108] However, SPR spectroscopy has its own disadvantages. For instance, SPR cannot easily discriminate between the specific and non-specific interactions on the sensor surface.[109] Elaborate washing process is not able to remove the non-specifically bound materials from the surface completely. In addition, SPR is not sensitive enough to detect low molecular weight compounds since it is mass sensitive. Limited sensor area is another challenge in SPR application too.

Chapter 2 - Fabrication and Characterization of Vertically Aligned Carbon Nanofiber Nanoelectrode Array (VACNF NEAs)

2.1 Introduction

CNFs are cylindrical nanostructures having diameters varying from a few to hundreds of nanometers and lengths in the order of micrometers.[110-111] Depending on the stacking arrangement of graphene sheets in the structure, the shape of CNFs can be classified as platelet, ribbon-like and herringbone.[112] The mechanical strength and electric properties of CNFs are similar to CNTs which are allotropes of carbon with a cylindrical nanostructure.[113] The primary distinguishing characteristic of CNFs from CNTs is that their whole surface area can be activated due to the free edge sites on the outer wall of CNFs.[114] CNFs can be activated by nitric acid or EC oxidation without degradation of their backbones structural integrity. The oxygen-containing activated sites are ideal for the immobilization and stabilization of biomaterials, an application that can be utilized for the development of biosensors. At the same time, they can transmit EC signals acting as transducers due to their good electrical conductivity.[115] Vertically aligned structures are typically referred to the structures that are orientated perpendicular to the substrate where they are grown. For a nanofiber, this means that the structure is straight and its axis is normal to the substrate.[110] VACNFs can be prepared as a dense mat or individual freestanding structures (sometimes arranged into a regular array). Van der Waals interaction between CNFs usually generates vertical alignment in a very dense format while an electric field is often required in order to form isolated freestanding CNFs.[116] Here, I briefly introduce synthesis of VACNFs by plasma enhanced chemical vapor deposition (PECVD) method followed by silicon dioxide (SiO_2) encapsulation and reactive ion etching (RIE) to produce VACNF NEAs for biosensor applications.

2.2 Fabrication of VACNF NEAs

Fabrication of CNF NEAs for biosensor application generally involves (1) contact metal and catalyst metal deposition; (2) growth of VACNFs by PECVD; (3) SiO_2 encapsulation and (4) mechanical polishing and RIE etching to expose the tips of the SiO_2 embedded VACNFs. The experimental procedures were detailed in the following sections.

2.2.1 Contact metal and catalyst deposition

Contact metal Cr and catalyst Ni were sputtered on the 1 cm x 2 cm SiO_2 substrate which was sonicated in isopropanol for 10 to 30 min and dried overnight in 100 °C oven. The thicknesses for Cr layer and Ni layer were 100 nm and 20 nm, respectively. An ion beam sputtering coater (Model 681, Gatan, Pleasanton, CA, USA) was used with 10.0 keV beam energy. During ion sputtering, the substrate in the coater chamber was rotated at the speed of 35 rpm, titling angel of 5° and rocking rate of 12 °/s. The coating rate for Cr is about 1.2 Å/s and for Ni is about 0.7 Å/s.

2.2.2 Plasma enhanced chemical vapor deposition (PECVD) for VACNF growth

Brush-like VACNFs were grown on the metal deposited SiO_2 substrate by using a PECVD system (Black Magic, Aixtron, Swavesey ,Cambridge, UK). First, the sample was placed on the cathode plate in the PECVD chamber. Then, the sample was annealed at 500 °C for 60s under the vacuum with a base pressure of ~0.11 mbar. Acetylene and ammonia were then introduced into the chamber at flow rates of 63 and 250 sccm, respectively and with 5.48 mbar processing pressure. At the same time, the temperature of the cathode plate was ramped up to 750 °C while the DC plasma was started (520 V and 45 W). Under above conditions, a 20 min deposition generated a VACNF arrays with fiber diameter of 50 to 100 nm and length of ~5 μm on the SiO_2 substrate.

2.2.3 Silicon dioxide (SiO_2) encapsulation

As-grown CNF arrays were embedded in SiO_2 insulating layer in order to obtain mechanical stability and avoid electrochemical background from the underlying metal film and sidewall of CNFs. A home built CVD system with a tube furnace (Thermo Electron Corporation, Asheville, NC, USA) was used for this purpose. After the base pressure of CVD chamber declined to ~50 mTorr, the chamber with as-grown CNF chip was heated up to 730 °C. Tetraethyl orthosilicate (TEOS) was then introduced into the chamber and deposited between each individual CNF at a vapor pressure of ~350 mTorr for 4 hr and ~400 mTorr for 3 hr. After 7 hr deposition, the VACNF arrays were fully embedded in the SiO_2 layers.

2.2.4 Planarization and reactive ion etching (RIE)

Since the surface of SiO_2 layer covering the top of the VACNF arrays was rough and uneven, mechanical polishing was applied using 0.3 μm alumina slurry to produce a flat surface. RIE with a mixture of CHF_3 and O_2 gases was then performed with NRE-3000 (Nano-Master Inc., Austin, TX) to selectively etch away desired amount of SiO_2. It can be controlled to expose 20% to 60% of the CNF tips based on the length variation of CNFs. A typical VACNF NEA in this study consists of randomly distributed CNF tips with an average CNF diameter of ~100–200 nm and an average spacing over ~1 μm (corresponding to a density of ~(1–10) x 10^7 CNFs-cm^{-2}).

2.3 General experimental details for protease detection

2.3.1 Materials

3-Aminopropyl-triethoxysilane (APTES), 2-(2-methoxyethoxy)ethoxyacetic acid, 1-ethyl-3-(3-dimethylaminopropyl)carbodiimide hydrochloride (EDC), 1-hydroxy-2,5-dioxopyrrolidine-3-sulfonic acid sodium salt (sulfo-NHS), sodium hydroxides, and 6-amino-1-

hexanol were purchased from Sigma-Aldrich (Saint Louis, MO, USA). 2-(4-Morpholino)ethane sulfonic acid (MES) and dithiothreitol (DTT) were purchased from Thermo Fisher Scientific (Fair Lawn, NJ, USA). Recombinant human legumain/asparaginyl endopeptidase (molecular weight of 49 kDa) and recombinant human cathepsin B (molecular weight of 29 kDa) were acquired from R&D Systems Inc. (Minneapolis, MN, USA). Only a few control experiments in immunoprecipitation study used cathepsin B purchased from Santa Cruz Biotechnology Inc. (Dallas, TX, USA). Before use for enzymatic reactions, legumain was activated in an activation buffer, consisting of 50 mM CH_3COONa (pH 4.0, adjusted by adding acetic acid) and 100 mM NaCl. Cathepsin B was activated in an activation buffer of 5 mM DTT and 25 mM MES (pH 5.0). Substrates Z-Ala-Ala-Asn-AMC and Z-Leu-Arg-AMC for fluorescence assay were obtained from Bachem (Torrance, CA, USA). Human breast whole tissue lysate (adult normal) with the stock concentration of 4.9 $mg \cdot mL^{-1}$ was purchased from Novus (Littleton, CO, USA). All aqueous solutions were prepared using 18.2 MΩ-cm resistivity deionized (DI) water from a bench-top water purifier (Barnstead EASYpure II RF/UV, Model D7035, Thermo Scientific, Asheville, NC, USA). For the details of synthesis of ferrocene-appended tetrapeptide for legumain cleavage (i.e. $H_2N\text{-}(CH_2)_4\text{-}CO\text{-}Ala\text{-}Ala\text{-}Asn\text{-}Leu\text{-}NH\text{-}CH_2\text{-}Fc$) and for cathepsin B cleavage (i.e. $H_2N\text{-}(CH_2)_4\text{-}CO\text{-}Leu\text{-}Arg\text{-}Phe\text{-}Gly\text{-}NH\text{-}CH_2\text{-}Fc$), please refer to Allan Prior's Ph.D. dissertation 2014 and reference1.

2.3.2 Electrode functionalization toward protease detection

To reduce nonspecific adsorption, the SiO_2 surface of the VACNF NEAs was first passivated with protective moieties containing ethylene glycol. The chip was immersed in an 8 g L^{-1} solution of APTES in ethanol for 20 minutes to produce a primary amine derivatized surface. The chip was treated with 50 μL solution of 0.1 mM of 2-(2-methoxyethoxy)ethoxyacetic acid,

100 g L^{-1} of EDC and 50 g L^{-1} of sulfo-NHS, and incubated at room temperature for 2 hours in an enclosed chamber (Arrayit, CA, USA). The carboxylic acid group of 2-(2-methoxyethoxy)ethoxyacetic acid formed an amide bond with the amino function on the chip surface, leaving ethylene glycol moiety covering the surface. The molecules attached to the CNF tips were then removed by electrochemical etching at 1.2 V (vs. Ag/AgCl (3 M KCl)) for 20 seconds in 1.0 M NaOH solution. This process regenerated clean CNF tips which contain abundant carboxylic acid functional groups.

The tetrapeptide H_2N-$(CH_2)_4$-CO-Ala-Ala-Asn-Leu-$NHCH_2$-Fc for legumain study or H_2N-$(CH_2)_4$-CO-Leu-Arg-Phe-Gly-NH-CH_2-Fc for cathepsin B study was covalently linked to the VACNF NEA by forming amide bond facilitated by EDC and sulfo-NHS. Typically, a solution of 10 μL of 10 mM tetrapeptide mixed with 90 μL of 10 g L^{-1} EDC and sulfo-NHS was applied onto the electrochemically activated VACNF NEA chip and incubated in the enclosed Arrayit chamber at room temperature for 2 hours. Control experiments and HPLC-MS characterization confirmed that only the end $–NH_2$ group of the tetrapeptide formed amide bond with the carboxylic acid group on the VACNF NEA. The $–NH_2$ and NH functions in asparagine and arginine moieties in the peptide do not react with the carboxylic acid group under the reaction conditions. In order to stabilize the electronic signal, the CNF electrode surface was further dipped into a solution of 5 mL of 1 mM 6-amino-1-hexanol containing 5 g L^{-1} EDC and 2 g L^{-1} sulfo-NHS so that the unreacted –COOH sites were linked with 6-aminohexanol.

2.3.3 Electrochemical measurements

The EC measurements were performed in a TEFLON cell with a total volume of 250 μL. The cell was sealed against a VACNF NEA chip with a 3-mm i.d. O-ring in a three-electrode configuration with the VACNF NEA as the working electrode, an Ag/AgCl (3M KCl) reference

electrode and a coiled Pt wire as the counter electrode. The electrolyte solutions consisted of 50 mM MES (pH = 5.0) and 250 mM NaCl for legumain experiment and 25 mM MES (pH = 5.0) for cathepsin B experiment. The average AC current was measured by applying an AC voltage bias on the DC staircase waveform with the potential sweeping from -0.05 to +0.65 V for legumain experiment and -0.1 V to +0.75 V for cathepsin B experiment, both at 10 $mV \cdot s^{-1}$ scan rate. The parameters including AC voltage amplitude and frequency were varied in specific experiments and specified as the results are presented in later sections.

2.4 Characterization of VACNF NEAs

Characterization of non-patterned VACNF NEAs by SEM and CV

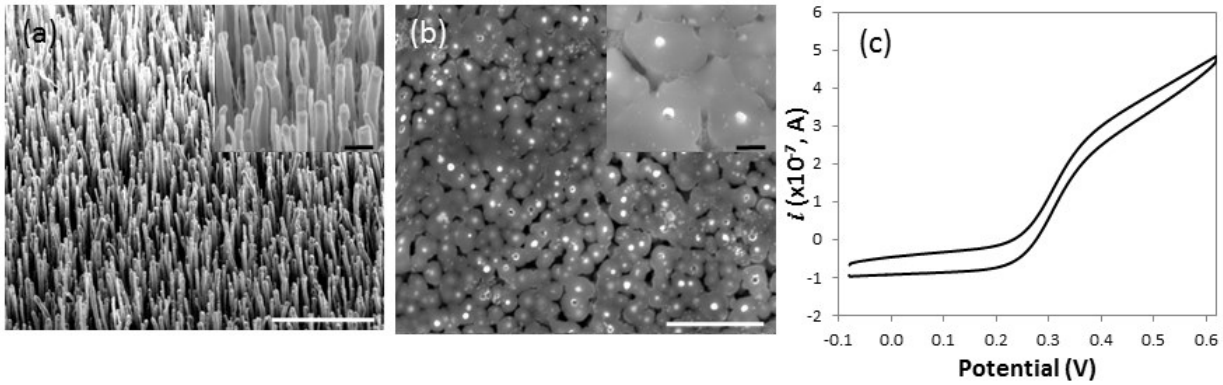

Figure 2.1 (a) SEM image of freestanding as-grown VACNFs (45° view) after PECVD. Scale bar: 4 μm (Insert: scale bar – 500 nm) (b) SEM image (top-down view) of CNFs after being encapsulated with SiO_2 using TEOS-CVD. Scale bar: 3 μm. (Insert: 45° view. Scale bar: 500 nm.). (c) CV of as-grown SiO_2 insulated vertically aligned CNF. The measurement was done in 50 mM $K_3Fe(CN)_6$ and 1.0 M KCl electrolyte at a scan rate of 50 $mV \cdot s^{-1}$.

As-grown VACNFs on the Si substrate after PECVD is shown in Figure 2.1a. Typically, it consists of randomly distributed CNF tips with an average CNF diameter of ~100–200 nm and an average spacing over ~1 μm (corresponding to a density of ~(1–10) x 10^7 CNFs-cm^{-2}). Figure

2.1b shows the CNFs are embedded in SiO_2 insulating layer with selective tips exposed by chemical mechanical polishing and RIE. The length of exposed CNF tips was controlled at ~50–300 nm by varying the RIE time to selectively remove SiO_2.

CV with 50 mM $K_3Fe(CN)_6$ and 1.0 M KCl has been used for characterization of electrodes. Due to the length of the diffusion layer is smaller than the average separation between the neighboring CNF, the CV curve is thus presented as a sigmoidal shape (Figure 2.1c), indicating the presence of a steady-state diffusion-limited current at each CNF.[117] The VACNF NEAs with low density is favorable for biosensor application. The CV signal is defined as the height of the sigmoidal curve (i.e. the steady state or limiting current i_l) which is given by Equation 2.1 for an ideal inlaid disc electrode[118]:

$$i_l = 4nFC_0^*D_0r \tag{2.1}$$

where n is the number of electrons transferred, C_0* is the bulk concentration of the species (mol/cm^3), D_0 is the diffusion coefficient (cm^2/s), r is the electrode radius (cm) and F is the Faraday constant (96485 s·A/mol). Different with macro-electrode such as macro glassy carbon electrode (GCE) where the current signal is proportional to the square root of the scan rate, the limiting current of NEAs is independent with the scan rate.

Characterization of patterned VACNF NEAs by SEM and CV

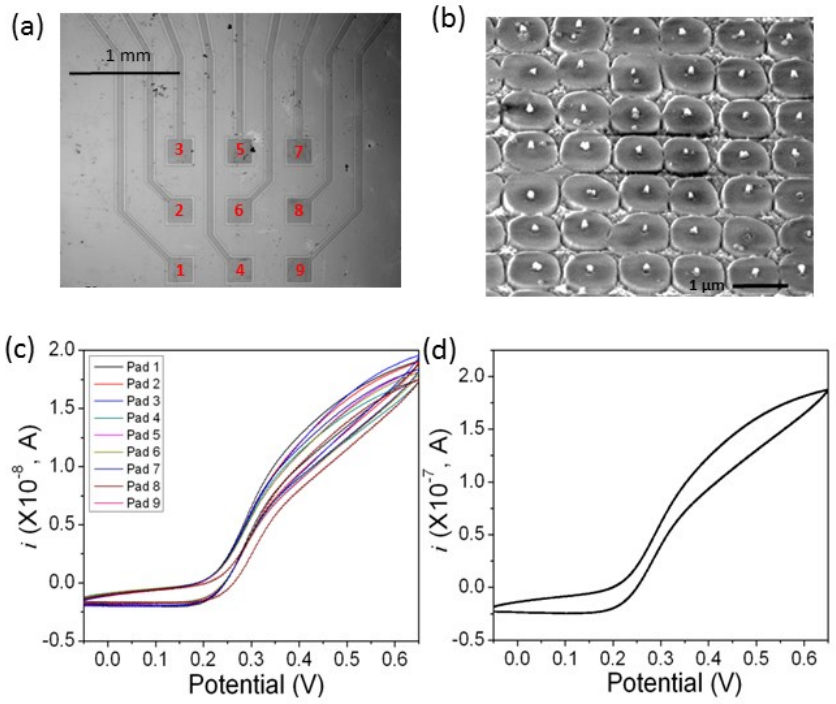

Figure 2.2 (a) Bright field microscope images of patterned VACNF NEAs using a 4x objective lens. (b) SEM image at 45° perspective view of the pattern VACNF NEAs. (c) CV of the patterned VACNF NEAs on each single microelectrode pads. (d) CV of patterned VACNF NEAs with all nine microelectrode pads connected together. The measurements were done in 50 mM $K_3Fe(CN)_6$ and 1.0 M KCl electrolyte at a scan rate of 50 $mV \cdot s^{-1}$.

Regular patterned VACNF NEAs can be mass-produced as multiplex chips on independently addressed microelectrode pads using UV- and e-beam lithography.[119] Figure 2.2a shows nine 200 μm x 200 μm microelectrode pads of ~100 nm-thick Cr film in a 3 x 3 array on a SiO_2-covered Si wafer. VACNFs were grown in regular 1 μm x 1 μm lattice on these microelectrode pads to form embedded NEAs which were independently connected with the external contact pads (1 mm x 1 mm) through the metallic line underneath the SiO_2 layer. Figure 2.2b shows the zoom-in image of exposed VACNF tips of ~100 nm in diameter protruding over the SiO_2 matrix. Figure 2.2c and 2.2d show the CVs of a 50 mM $K_3Fe(CN)_6$ solution from all

nine VACNF NEAs separately and together. Clearly, they all showed the characteristic sigmoidal shape with low background and almost identical limiting current, indicating the high uniformity of these NEAs.

2.5 Conclusions

In summary, the procedure of the fabrication of as-grown VACNF NEAs has been discussed. The electric field of PECVD could help to produce vertically aligned carbon structure. By selectively etching away the SiO_2 insulating layer and exposing the tips of the VACNFs by RIE, VACNF NEAs can be fabricated and used as a biosensor through functionalizing the tips with biological molecules, such as peptides[1-2] and DNA[104]. VACNF NEAs have sigmoidal shaped CV curve due to the length of diffusion layer is much smaller than the separation between the adjacent fibers. Finally, low background sigmoidal shaped CV curve and almost identical limiting current indicated the high uniformity of the e-beam patterned VACNF NEAs.

Chapter 3 - Cancer-related Protease Biosensor Based on Enhanced AC Voltammetry Using VACNF NEAs

Reproduced in part by permission of American Chemical Society.

Published as: Swisher, L. Z.; Syed, L. U.; Prior, A. M.; Madiyar, F. R.; Carlson, K. R.; Nguyen, T. A.; Hua, D. H.; Li, J. *J. Phys. Chem. C* **2013**, *117*, 4268-4277.

3.1 Introduction

Proteases, the proteolytic processing proteins, are ubiquitous in living organisms and regulate a multitude of cellular processes including the cell cycle, hormone activation, apoptosis and angiogenesis.[48-50] The cysteine protease legumain, also known as asparaginyl endopeptidase (AEP), has a strict specificity for hydrolysis of asparaginyl bonds.[120] It is highly expressed in macrophages, on the cell surfaces and membranous vesicles in the metastatic and invasive solid tumors where it activates other proteases such as cathepsin B, H and L, that have both elastinolytic and collagenolytic activities.[121-123] However, overexpression of those cysteine proteases was not found in the normal tissue. In breast cancer, several recent studies have shown that absence of the cysteine protease inhibitor leads to increased growth and metastasis.[124] Thus, rapid detection of the presence and activity of cancer-mediated proteases (i.e. legumain and cathepsin B), should be developed for enhancement of treatment.[125]

Traditional methods for enzyme activity study include gel electrophoresis, HPLC, ELISA and optical methods.[126-129] These methods require specific synthesis of peptides, fluorescent labels and sophisticated instrumentations, which are high-cost and time-consuming. Radioimmunoassay (RIA) had been widely used as an highly sensitive detection method but is diminished nowadays due to health safety and environment concerns.[130] Simple rapid electronic and/or electrochemical methods to detect enzyme activities are thus important in developing

portable systems for point-of-care diagnosis and treatment monitoring of diseases such as cancers. Recently, EC methods using CV measurements of redox-labeled peptides attached on macroscopic gold electrodes have been demonstrated in detecting high-activity proteases such as trypsin, thrombin and plasmin.[64, 131] Due to the localized sensing mechanism, an array of electrodes functionalized with different peptides could potentially detect multiple enzymes in a small sample volume. However, electrochemical detection of proteases that are more relevant to cancers, such as legumain and cathepsin B, has not been reported. These enzymes have much lower catalytic activity, making the measurement more difficult. Here we focus on a new electrochemical technique enabled by nanostructured electrodes that can successfully detect these enzymes.

It is well known that reducing the electrode size can dramatically enhance the detection sensitivity and temporal resolution of electrochemical measurements.[132-133] This trend extends from the scale of microns to nanometers. Well-separated NEAs, either in regular pattern or in random distributions (also referred to as nanoelectrode ensembles (NEEs)), have attracted extensive interests for highly sensitive electroanalysis, measuring fast electrochemical kinetics, and biosensing.[134-136] Fabrication methods such as nanosphere lithography and E-beam lithography have been developed for the well-ordered NEAs.[137-138] Carbon based NEAs are particularly attractive for biosensors due to the wider applicable potential window and ease in biofunctionalization through robust covalent attachment. Development in this area, however, has been limited by the lack of readily available methods to fabricate reliable NEAs. Recent research in carbon nanotechnology has provided a method to fabricate well-controlled NEAs using VACNFs embedded in insulating materials.[136, 139-140] Both precisely patterned and randomly distributed CNFs with the average diameter of 50–200 nm and uniform vertical alignment have

been fabricated on 4" Si wafers[141] and can be mass-produced into robust NEAs on individually addressed microelectrodes forming an "array-in-array" format. Various applications of VACNF NEAs with and without further encapsulation of insulating materials have been demonstrated for various biosensing or biomedical applications, including DNA hybridization analysis,[104] glucose detection,[139] electrochemical sensing of neurotransmitters,[142] neural electrical recording,[143] and gene delivery.[144] Here we employ the embedded VACNF NEAs for enzymatic studies. The SiO_2 matrix was selectively etched by plasma etching to expose ~50–200 nm long CNF tips over the surface (as shown in Figure A.1). Specific peptide substrates were functionalized at the exposed CNF tips and subjected to proteolysis by proteases. The small radius of the CNF tips (~50–100 nm) protruding over the SiO_2 matrix makes it easier for enzymes to access to the peptides, avoiding the steric hindrance that is normally encountered on macroscopic surfaces.

Generally, CV measurements of bulk redox species using embedded VACNF NEAs show characteristic sigmoidal curves,[104, 145] in which the tiny CNF tips carry much higher current densities than macro- or micro-electrodes. This feature indicates one of the predicted benefits of nanoelectrodes due to the nonlinear radial diffusion of redox species to the electrode surface.[146] The NEA also presents much smaller electrochemical cell time constant which allows the electrochemical measurement to be carried out at a much higher speed. These properties make NEAs attractive for rapid high-sensitivity biosensing applications.

Recently, we discovered that the electrochemical measurements on VACNF NEAs can be significantly improved by applying an AC voltage bias on the direct current (DC) ramps in the common CV measurement, i.e. by using ACV.[47] An anomalously high electron transfer rate was obtained with redox-active Fc molecules attached to the exposed CNF tips of the embedded NEAs.[47] This was attributed to the unique conically stacked graphitic structure of the CNFs,

which opened a new capacitive pathway for AC current. As a result, ACV on VACNF NEAs can be carried out at much higher AC frequency (at kHz) than <100 Hz on macroscopic GCEs. Since the magnitude of the signal in ACV, i.e. AC current amplitude, increases monotonically with the AC frequency at < 1 kHz, the detection sensitivity can be greatly enhanced using VACNF NEAs. The ACV is particularly advantageous over common CV for measuring small quantities of surface-attached redox molecules since the electrons can be shuffled back and forth for many times between the electrode and each adsorbed molecules. Here, we report the application of this property on detection of the enzymatic activities of legumain and cathepsin B by monitoring the kinetic decrease of the ACV signals of Fc attached to the CNF tip through a specific peptide linker during proteolysis. The data are well explained with the Michaelis-Menten heterogeneous enzymatic model.

3.2 Design and electrochemical characterization of VACNF NEAs for protease detection

Figure 3.1 shows the structure of an embedded VACNF NEA covalently attached with Fc-linked peptides at the exposed CNF tips. The Fc moiety at the distal end provides a reliable redox signal at ~0.25 V vs. Ag/AgCl (3M KCl) in ACV measurements. Upon supplied with the specific protease, the peptide is expected to be cleaved at the particular site. As a result, the Fc moiety is released from the electrode surface into the bulk solution, causing the redox signal to decrease. The kinetic of the enzymatic reaction at the electrode surface will be monitored by continuously repeated ACV measurements. The advantage of this method is that the appended Fc moiety provides a characteristic faradaic signal which can be easily separated from the unstable nonfaradaic background and other interfering redox signals. The key for this method is that the Fc signal needs to be relatively large and stable over the period of the kinetic measurements (up

to ~1 hour) and the ACV measurement at each point is fast enough to provide ~1 minute (or less) of temporal resolution. This may become challenging for enzymes requiring long peptide substrate sequences for specific recognition. The Fc signal involves electron transfer between Fc molecule and the electrode surface, which is highly sensitive to the Fc-surface distance and the molecular packing of the peptides on the electrode surface. Thus the electrochemical properties of Fc-linked peptide attached on VACNF NEAs need to be carefully characterized.

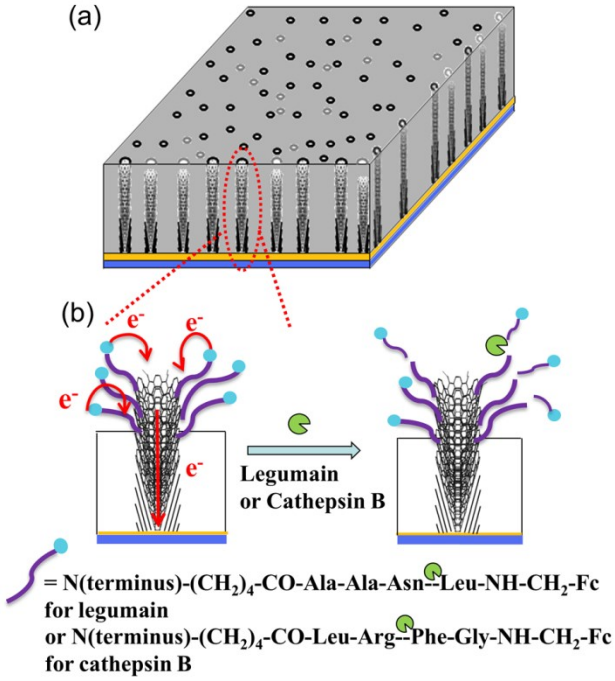

Figure 3.1 Schematic diagram of the cleavage of Fc-linked tetrapeptides at the VACNF NEA tip by specific proteases. (a) A random VACNF array embedded in the SiO_2 matrix. (b) Electron transfer from appended ferrocene at the distal end of the peptide to the underlying metal film electrode through the VACNFs and the loss of the electrochemical signal from ferrocene due to the cleavage of the peptide at specific sites.

Figure 3.2 shows the comparison of ACVs of a macro-GCE and a VACNF NEA, both functionalized with the tetrapeptide H_2N-$(CH_2)_4$-CO-Ala-Ala-Asn-Leu-$NHCH_2$-Fc to be used for

legumain study. A peak current was observed at ~0.2 V vs. Ag/AgCl (3M KCl) for both electrodes. The amplitude of the peak current density (i_p) in the ACVs with macro-GCE increased from ~1.0 x 10^{-7} A·mm^{-2} at 10 Hz to ~2.0 x 10^{-7} A·mm^{-2} at 40 Hz, but then dropped to zero at 1500 Hz. At the meantime, the background signal steadily increased from ~4.7 x 10^{-7}, to 1.8 x 10^{-6} and 2.8 x 10^{-6} A·mm^{-2}, respectively. In contrast, although the i_p of ACV with VACNF NEAs was not measurable at 10 Hz and 40 Hz, it rose clearly above the background at 1500 Hz, giving ~2.0 x 10^{-8} A·mm^{-2}. Obviously, VACNF NEAs allowed the Fc signal to be detected at much higher frequency. It is noteworthy that the current density in Figure 3.2 was calculated with the geometric electrode surface area. As shown in Figure A.1, the actual exposed CNF surface area in the VACNF NEA is more than ~100 times less than the geometric surface area. Hence the real current density at the CNF tip is at least 10 times higher than that at the GCE. Generally, the electrochemical signal is very sensitive to Fc-surface distance since the electron transfer rate decays exponentially versus the Fc-surface distance. Hence electrochemical sensors based on redox reactions normally use linker molecules less than 2 nm in length. Here, the electron transfer on both GCEs and VACNF NEAs was not significantly affected by the tetrapeptide and the linker (with a fully extended length of ~2.5 nm). Experiments with an even longer octapeptide (Figure A.15) did not show notable difference in Fc signal, suggesting that the molecule might be folded back to the CNF surface.

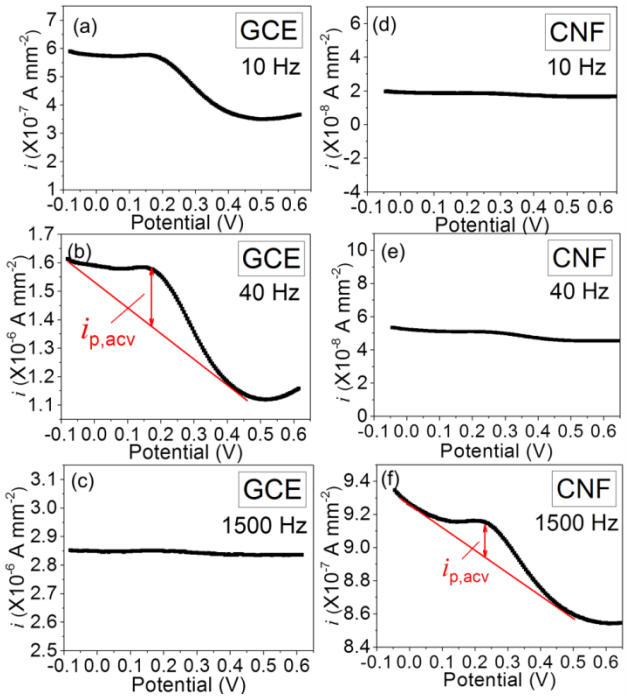

Figure 3.2 Comparison of ACVs measured at 10, 40 and 1500 Hz of H_2N-$(CH_2)_4$-CO-Ala-Ala-Asn-Leu-$NHCH_2$-Fc immobilized on a macro-GCE (a–c) and on a VACNF NEA (d–f). All the measurements were done in 500 µL of 50 mM MES (pH 5.0) and 250 mM NaCl. Sinusoidal waves with the fixed amplitude of 25 mV were superimposed on a DC staircase ramp from -0.05 to +0.65 V at a scan rate of 10 mV·s^{-1}. The measured average AC current at each point was normalized by the 7.1 mm^2 geometric surface area defined by the 3-mm i.d. O-ring. The actual CNF surface area is ~100 times less.

ACV uses a sinusoidal AC voltage superimposed on a DC potential ramp for voltammetric measurements. It has advantages over commonly used DC-based CV, particularly for biosensors, due to the ability to amplify the electrochemical signal of small quantity of redox tags by shuffling the electron between the redox tag and the electrode many times. In general, the signal increases with AC frequency at low frequencies but is saturated and then decreases at higher frequencies. In our previous study using VACNF NEAs, the optimum frequency for Fc

through a short NH_2CH_2- linker was found to be 40 times higher than that on the macro-GCE.[47] Figure 3.3 illustrates the similar phenomena with Fc attached to the electrode surface through the tetrapeptide and a longer linker group versus the AC frequency. Clearly, the optimum frequency which gave the maximum i_p was 40 Hz for the GCE, but 1750 Hz for the VACNF NEA. Despite that both frequency values are about half of those with short NH_2CH_2- linker, the drastic difference between VACNF NEA and macro-GCE remained the same, i.e. the optimum frequency on the VACNF NEA was ~40 times of that on the GCE. The higher applicable AC frequency at VACNF NEA afforded a larger ACV signal (i.e. i_p) and faster ACV measurements. Each ACV measurement in Figure 3.2 can be done in ~60–70 s. As a result, the kinetics of enzymatic cleavage can be monitored with continuously repeated ACV measurements at a temporal resolution of ~1 minute.

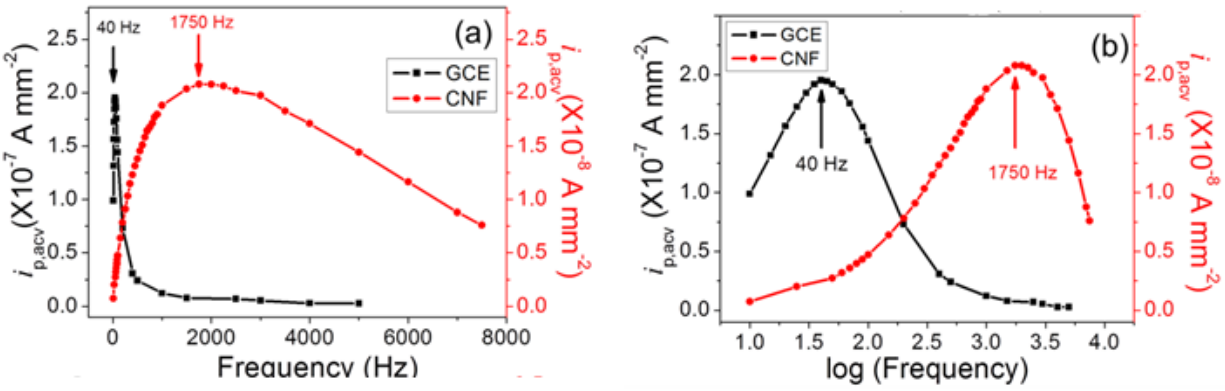

Figure 3.3 (a) Background-corrected ACV peak current density $i_{p,acv}$ (normalized to the 7.1 mm^2 geometric electrode area) of H_2N-$(CH_2)_4$-CO-Ala-Ala-Asn-Leu-$NHCH_2$-Fc immobilized on a GCE (square) and a VACNF NEA (filled circle) plotted against the AC frequency. (b) Plot of $i_{p,acv}$ versus logarithm of the AC frequency. Note: The real CNF surface area is ~100 times less than the geometric surface area defined by the O-ring.

The AC peak current density $i_{p,acv}$ can be extracted by subtracting the background (as a simple sloped straight line). These values are plot in Figure 3.3a versus the AC frequency. Clearly, the AC peak current density of the GCE shows a sharp peak with the maximum at 40 Hz and a full width at half maximum (FWHM) of ~140 Hz. The current value approximately increases linearly with the AC frequency but drops rapidly as the AC frequency exceeds 40 Hz. In contrast, the maximum AC peak current density was observed at 1750 Hz on the VACNF NEA and the FWHM asymmetrically spread over 5000 Hz, indicating a large range of frequency that can be used. The current density increases about linearly with the frequency up to ~1000 Hz. When the peak current density is plot versus the logarithm of the AC frequency as shown in Figure 3.3b, the curves obtained with the GCE and the VACNF NEA show similar shape but with shifted peak frequency. It needs to be noted that the ACV measurements are not stable with the GCE. The peak shape changed significantly in about 10 minutes as shown in Figure A.2, which limits the use of GCEs for the measurement of enzymatic kinetics. In contrast, the peak shape of the ACV curve of VACNF NEAs is much more stable.

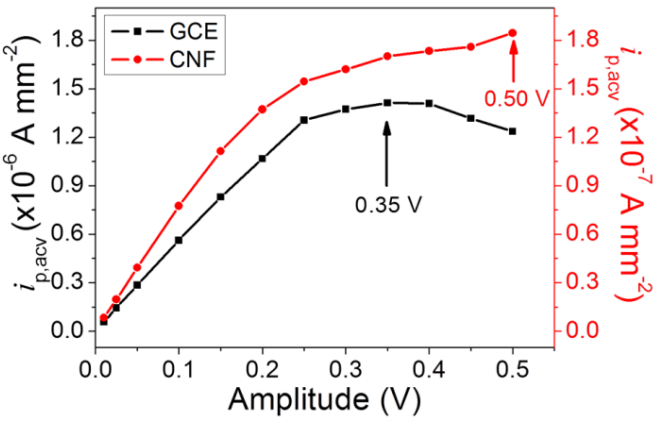

Figure 3.4 Background-corrected ACV peak current density $i_{p,acv}$ (normalized to the 7.1 mm^2 geometric electrode area) of H_2N-$(CH_2)_4$-CO-Ala-Ala-Asn-Leu-$NHCH_2$-Fc immobilized on a

GCE and a VACNF NEA plotted against the amplitude of the AC voltage (square: GCE, filled circle: VACNF NEA).

The peak current in ACVs also depended on the amplitude of the applied AC voltage. Figure 3.4 shows that there is a small difference between the GCE and the VACNF NEA. The peak current density ($i_{p,acv}$) reached to the highest value of ~1.5 x 10^{-6} A·mm^{-2} at the amplitude of 0.35 V for GCE while the peak current density kept increasing at the amplitude up to 0.50 V for VACNF NEA. However, for the VACNF NEA at amplitude larger than 0.15 V, the value of the peak current density deviated from the linear relationship and the raw ACV peak became broad and unstable (Figure A.3). For this reason, we choose amplitude at 0.15 V as the optimum working amplitude in all the following ACV measurements for legumain activity study. For cathepsin B study, the tetrapeptide H_2N-$(CH_2)_4$-CO-Leu-Arg-Phe-Gly-NH-CH_2-Fc was immobilized on the VACNF NEA, giving very similar ACV properties with slightly different optimum AC frequency (800 Hz) and amplitude (0.15 V), respectively (see Figure A.4). These optimum parameters were used in the following kinetic study on cathepsin B activities.

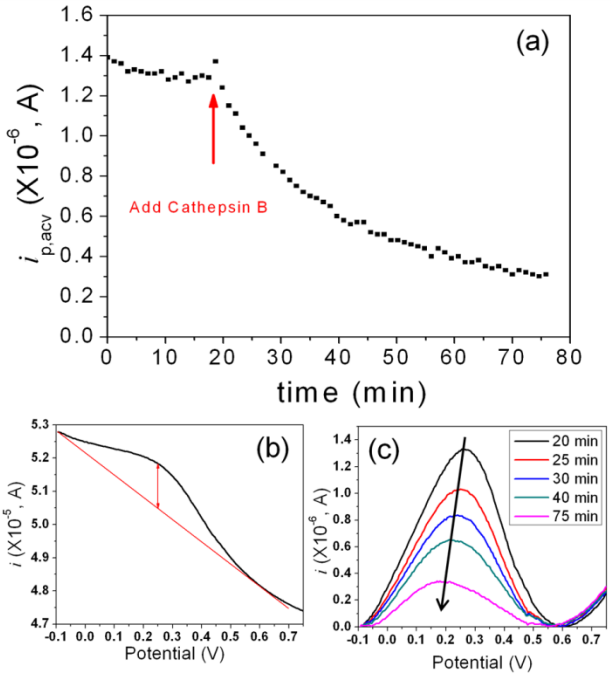

Figure 3.5 (a) The change of the peak current ($i_{p,acv}$) of H_2N-$(CH_2)_4$-CO-Leu-Arg-Phe-Gly-NH-CH_2-Fc immobilized on a VACNF NEA in continuously repeated ACV measurements while 25 µL of 9.8 ng·µL^{-1} (338 nM) cathepsin B in the activation buffer consisting of 5 mM DTT and 25 mM MES (pH 5.0) was added into the electrochemical cell containing 250 µL of 25 mM MES (pH 5.0). All ACV measurements were carried out at f = 800 Hz and AC voltage amplitude V_0 = 150 mV. (b) ACV curve measured at the time of 20 minute immediately after the cathepsin B solution was added into the electrochemical cell. (c) Five representative background-subtracted ACV curves measured at 20 (black), 25 (red), 30 (blue), 40 (green) and 75 minute (pink), respectively, showing the decrease of $i_{p,\,acv}$ due to enzymatic cleavage.

Figure 3.5 shows the change of peak current ($i_{p,acv}$) over time during continuously repeated ACV measurements with Fc-linked tetrapeptide (H_2N-$(CH_2)_4$-CO-Leu-Arg-Phe-Gly-NH-CH_2-Fc) immobilized on a VACNF NEA. The initial signal was quite stable, with only slow drifting. At ~20 minute, a solution of 25 µL of 9.8 ng·µL^{-1} (338 nM) cathepsin B in the

activation buffer was added into the electrochemical cell, giving a final enzyme concentration of 30.7 nM. Due to the disturbance to in electrolyte, the ACV peak current jumped up and then followed by an exponential decay. Figure 3.5b shows the ACV curve measured at 20 minute, immediately after the cathepsin B solution was added. A clear peak at around 0.25 V confirms the immobilization of Fc-linked tetrapeptide on the electrode surface. Figure 3.5c further illustrates the representative background-subtracted ACV curves corresponding to 0, 5, 10, 20 and 55 minutes, respectively, after adding the cathepsin B solution. The peak current clearly decreased over time and the peak position slowly shifted from 0.27 V to 0.18 V. Two control experiments (Figure A.5) were carried out and confirmed that the exponential decay in $i_{p,acv}$ was truly attributed to the kinetics of enzymatic cleavage of the peptide. First, 25 μL of blank activation buffer, i.e. 5 mM DTT and 25 mM MES (pH 5.0), was added into the electrochemical cell prefilled with 250 μL of electrolyte (25 mM MES (pH 5.0)). The disturbance to the ACV signal was negligible in this process. Second, a solution of 25 μL of activation buffer containing deactivated cathepsin B (which was confirmed with the fluorescence assay) was added into the electrochemical cell in the similar way as in the first case. Neither case showed the characteristic exponential decay observed when the activated enzyme was introduced. It is clear that the exponential decay was due to enzymatic cleavage to the tetrapeptide substrate by cathepsin B.

3.3 Modified Michaelis-Menten model for heterogeneous enzymatic reaction

The observed proteolysis kinetics may be explained with a modified Michaelis-Menten model for heterogeneous enzymatic reactions:[147]

$$\mathrm{E} + \mathrm{S_s} \underset{k_{-1}}{\overset{k_1}{\longleftrightarrow}} \mathrm{ES_s} \xrightarrow{k_{cat}} \mathrm{E} + \mathrm{P_s} + \mathrm{P}, \tag{3.1}$$

where E, S_s, ES_s, P_s and P represent the enzyme, the surface-bound peptide substrate, the enzyme-substrate complex on the electrode surface, the surface-attached product, and the product released to solution, respectively. The reaction rate can be defined as

$$\upsilon = -\frac{d\Gamma_{Ss}}{dt} = \frac{d\Gamma_{Ps}}{dt} = \frac{k_{cat}[\mathrm{E_0}] \times \Gamma_{Ss}}{\mathrm{K_m} + [\mathrm{E_0}]}, \tag{3.2}$$

where k_{cat} is the dissociation rate constant, $\mathrm{K_m} = (k_{cat}+k_{-1})/k_1$ is the Michaelis-Menten constant, and Γ_{Ss} and Γ_{Ps} represent the surface densities of original and reacted peptide substrates, respectively. At low enzyme concentrations with $[\mathrm{E_0}] << \mathrm{K_m}$, an approximate relationship can be obtained as

$$\upsilon = -\frac{d\Gamma_{Ss}}{dt} = \frac{d\Gamma_{Ps}}{dt} = \frac{k_{cat}}{\mathrm{K_m}}[\mathrm{E_0}] \times \Gamma_{Ss}. \tag{3.3}$$

The reaction rate υ (or $-d\Gamma_{Ss}/dt$) is a time-dependent quantity proportional to the change in electrochemical signals (dE/dt), where E is the kinetic electrochemical signal corresponding to the peak current i_p in ACV measurements. As a result the slope of (dE/dt) versus the time-dependent Γ_{Ss} will be equal to $(k_{cat}/\mathrm{K_m})[\mathrm{E_0}]$, namely

$$-\frac{d\Gamma_{Ss}/dt}{\Gamma_{Ss}} = -\frac{dE/dt}{S} = \frac{k_{cat}}{\mathrm{K_m}}[\mathrm{E_0}]. \tag{3.4}$$

Thus, by rearranging the kinetic electrochemical data, we can derive the value of "specificity constant" $k_{cat}/\mathrm{K_m}$ which is commonly used to represent the catalytic efficiency of enzymes.

3.4 Analyses of legumain and cathepsin B activity

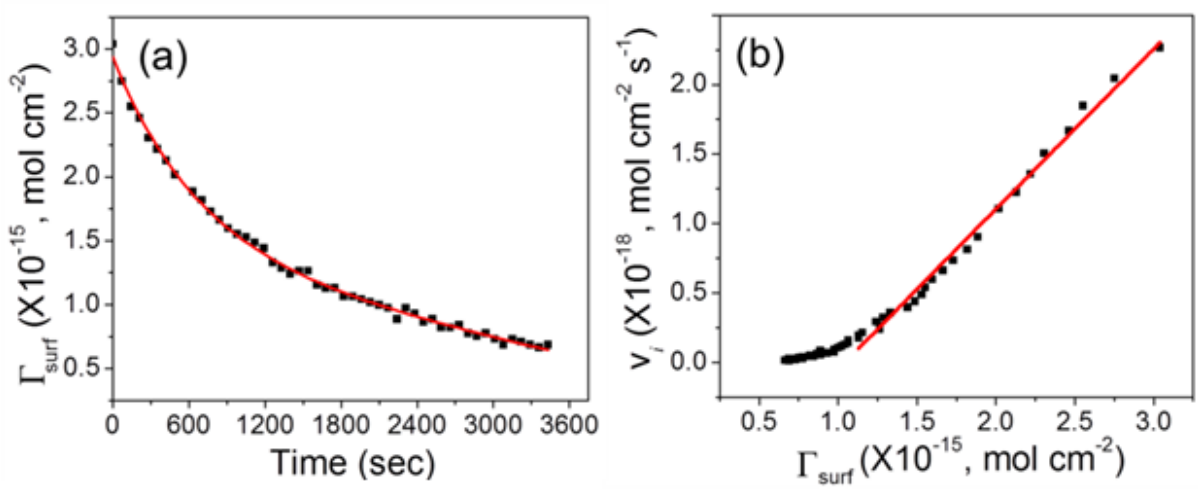

Figure 3.6 Replot of the data presented in Figure 3.5. (a) Decrease of the quantity of surface adsorbed Fc (i.e. Γ_{surf}) during enzymatic cleavage of the tetrapeptide after adding the cathepsin B solution. (b) Plot of the reaction rate (v_i) versus the quantity of surface adsorbed Fc (Γ_{surf}) during the enzymatic reaction.

To further analyze the kinetic enzymatic process, the peak current in ACV was converted into the quantity of surface adsorbed Fc (i.e. Γ_{surf}) based on[148]

$$i_{p,acv} = \left(\frac{2}{\pi}\right)\left(\frac{F^2}{4RT}\right)\Gamma_{surf}(2\pi f)V_0, \tag{3.5}$$

where the AC frequency f was 800 Hz and the amplitude of the AC voltage V_0 was 150 mV. Although the Γ_{surf} value derived with Equation 3.5 is known to be smaller than that obtained with other methods, particularly at high frequencies, the linear relationship between $i_{p,acv}$ and Γ_{surf} remains true. The deviation of the proportional coefficient from the true value is cancelled in later steps and does not affect the final results. As shown in Figure 3.6a, the kinetic data can be

fitted with an exponential decay superimposed on a linear curve corresponding to the slow baseline drift. The fitting equation is

$$\Gamma_{surf} = 1.55\times10^{-15}\times e^{\left(-\frac{t}{683.6}\right)} - 2.19\times10^{-19}t + 1.38\times10^{-15}. \quad (3.6)$$

From equation 3.6, the reaction rate v_i at different Γ_{surf} can be calculated. The results were presented in Figure 3.6b, which appeared to be a linear curve in the high Γ_{surf} region. This linear curve is fitted by equation

$$v_i = 1.15\times10^{-3}\Gamma_{surf} - 1.20\times10^{-18} \ . \quad (3.7)$$

As mentioned earlier, both v_i and Γ_{surf} are proportional to $i_{p,acv}$. The slope of v_i versus Γ_{surf}, however, is independent of the exact proportional coefficient since it presented in both v_i and Γ_{surf} and is thus cancelled. Therefore, we can derive the exact slope without being affected by the ACV experimental conditions. Equation 3.7 gives a slope of 1.15 x 10^{-3} s^{-1}, which equals to (k_{cat}/K_m)[E_0] as described in Equation 3.3. With [E_0] = 30.7 nM, the value of the "specificity constant" k_{cat}/K_m can be calculated as 3.8 x 10^4 $M^{-1}s^{-1}$. This value is close to the value of 2.3 x 10^4 $M^{-1}s^{-1}$ derived from the comprehensive analysis with the fluorescence assay in a series of peptide substrate concentrations (Figures A.6 & A.7). It is also within the range reported in literature which varies from ~2 x 10^3 $M^{-1}s^{-1}$ to ~7 x 10^6 $M^{-1}s^{-1}$. [147, 149-150]

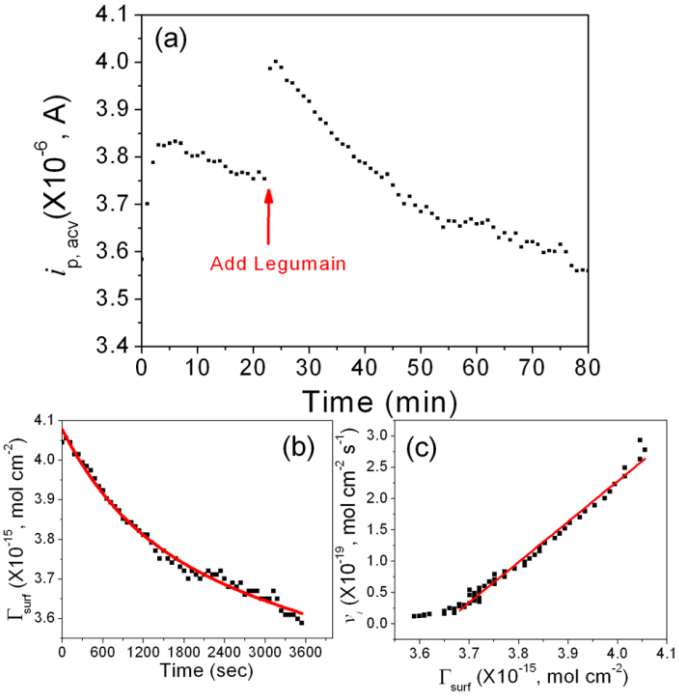

Figure 3.7 (a) The change of the peak current ($i_{p,acv}$) of H_2N-$(CH_2)_4$-CO-Ala-Ala-Asn-Leu-NH-CH_2-Fc immobilized on a VACNF NEA in continuously repeated ACV measurements while 11 µL of 90.9 ng·µL^{-1} (1.90 µM) legumain in the activation buffer consisting of 50 mM CH_3COONa (pH = 4.0, adjusted by adding acetic acid) and 100 mM NaCl was added into the electrochemical cell containing 250 µL of 50 mM MES (pH 5.0) and 250 mM NaCl. All ACV measurements were carried out at f = 1750 Hz and AC voltage amplitude V_0 = 150 mV. (b) Replot of the data presented in figure (a) showing the reduction of the quantity of surface adsorbed Fc (i.e. Γ_{surf}) during enzymatic cleavage of the tetrapeptide after adding the legumain. (c) Plot of the reaction rate (v_i) versus the quantity of surface adsorbed Fc (Γ_{surf}) during the enzymatic reaction.

Figure 3.7 shows the ACV measurements with H_2N-$(CH_2)_4$-CO-Ala-Ala-Asn-Leu-NH-CH_2-Fc immobilized on a VACNF NEA. Comparing to cathepsin B, the change of peak current corresponding to the cleavage by legumain was smaller, likely due to the difference in the

enzyme activity. None of the two control experiments in Figure A.8 by adding the blank activation buffer and the buffer containing deactivated legumain (confirmed with fluorescence assay), respectively, showed the characteristic exponential decay in $i_{p,acv}$. The former caused negligible disturbance to the electrochemical signal. The latter caused the $i_{p,acv}$ to slowly rise by ~5% after 5 minutes and then became stabilized, which might be attributed to the disturbance to the tetrapeptide conformation on the electrode surface.

The data in Figure 3.7b can be fitted with the following equation:

$$\Gamma_{surf} = 3.23\times10^{-16}\times e^{\left(-\frac{t}{1101}\right)} - 4.36\times10^{-20}t + 3.75\times10^{-15} \quad (3.8)$$

where the time constant is 1101 s (~18 min.), indicating that the reaction is quite slow. It normally took ~1 hour to complete the kinetic measurement. This was found to be limited by the low enzymatic activity of legumain. However, it was still possible to extract the faradaic signal of Fc from the varying background with the ACV measurements. Figure 3.7c gives a linear curve fitted by equation $v_i = 6.30\times10^{-4}\Gamma_{surf} - 2.30\times10^{-18}$ with the slope of 6.30 x 10^{-4} s^{-1} at $[E_0]$ = 80.1 nM. From this analysis, the value of the k_{cat}/K_m can be calculated as 7.9 x 10^3 $M^{-1}s^{-1}$. This value is higher than the value of 4.3 x 10^3 $M^{-1}s^{-1}$ derived from the comprehensive analysis using the fluorescence assay (Figures A.9 & A.10) and the specifications provided by the vendor (R&D Systems).

The kinetic measurements with ACV for both cathepsin B and legumain were repeated at least three times under similar conditions as those in Figure 3.5 and Figure 3.7. The results were consistent and reproducible. More comprehensive measurements at varied enzyme concentrations and peptide lengths will be reported in future studies. Table 3.1 summarizes the statistical values of the specificity constant k_{cat}/K_m derived from both electrochemical method

using ACVs on VACNF NEAs in comparison with the fluorescence assay based on a series of substrate concentrations in solution, for both legumain and cathepsin B. Interestingly, the electrochemical method gave higher k_{cat}/K_m values for both of legumain and cathepsin B than the fluorescence assay. In contrast, other studies using macroscopic electrodes found that the electrochemically measured k_{cat}/K_m was normally lower than solution based assays, primarily due to the steric effects which lower the access of enzyme to the peptides attached to the flat surface.[64, 131] The results confirmed that the small radius in VACNF NEAs helped to eliminate the steric hindrance. The peptide substrates for the fluorescence assay consisted of only 3 and 2 amino acids, respectively, which were also expected to have lower binding affinity than the tetrapeptides used for our electrochemical measurements.

Table 3.1 Comparison of the specificity constant k_{cat}/K_m for legumain and cathepsin B, derived from the electrochemical method (i.e. ACV on VACNF NEAs) and the fluorescence assay in solutions.

Enzyme	**Peptide Sequence**	k_{cat}/K_m **($M^{-1}s^{-1}$)**
Legumain	(FL[a]) Ala-Ala-Asn↓-AMC	$(4.3 \pm 0.6) \times 10^3$
	(EC[b]) Ala-Ala-Asn↓-Leu-NH-CH_2-Fc	$(11.3 \pm 3.8) \times 10^3$
Cathepsin B	(FL) Leu-Arg↓-AMC	$(2.3 \pm 1.7) \times 10^4$
	(EC) Leu-Arg↓-Phe-Gly-NH-CH_2-Fc	$(4.3 \pm 0.8) \times 10^4$

[a]FL: fluorescence; ↓: cleavage site. The fluorescence data were derived from the analysis in Figures A.6, A.7, A.10 and A.11.

[b]EC: electrochemistry. The electrochemical data were statistical value over at least duplicated experiments.

The values of the specificity constant k_{cat}/K_m for cathepsin B by both electrochemical and fluorescence assays are about 5 times of that of legumain. For ACV measurements, this helps to reduce the time constant for the exponential decay and makes the experiment easier and more reliable. As a result, lower enzyme concentration can be measured. From these results, it can be

concluded that the ACV would work even better for measuring proteases with the k_{cat}/K_m values higher than ~4 x 10^4 $M^{-1}s^{-1}$. But even proteases with relatively low specificity constant (such as legumain and cathepsin B) can still be reliably measured. Even though the required enzyme concentration was ~5 to 10 times higher than that by the fluorescence assay, the electrochemical method has a potential advantage that simultaneous detection of multiple proteases in a small volume is possible, attributed to its localized sensing mechanism using surface-attached peptides. Further investigation is in progress to assess the cross-reactions between different enzyme-substrate pairs.

The vendor suggests that legumain cleaves peptide bonds with asparagine (Asn) at the P1 position while it has been reported that cathepsin B cleaves peptide or AMC bonds with arginine (Arg) at P1 site.[151] To confirm the cleavage site, we have incubated each tetrapeptide with legumain and cathepsin B and measured the products with HPLC. As shown in Figure A.11 and Figure A.12, the HPLC graphs of the cleaved products were directly compared with those of the pure tetrapeptides and synthesized fragments (mono amino acid or dipeptide). The cleaved products were further validated with mass spectrometry. These experiments clearly demonstrated the cleavage site as listed in Table 3.1. Interestingly, even after incubating for 2 hours, the cleaved tetrapepetide concentration was only ~1/5 of the total concentration for legumain and ~3/4 for cathepsin B. The fluorescence assay reported earlier is sensitive to the absolute amount of cleaved products while the electrochemical assay is sensitive to the percentage of the cleavage to the surface-attached peptide. The large amount of starting peptides used in the fluorescence assay partially contributed to its capability to measure lower enzyme concentrations. The electrochemical method, however, has advantage for miniaturization and multiplexing which may be critical for rapidly screening multiple proteases in disease diagnosis. It is noteworthy that

the k_{cat}/K_m values of legumain and cathepsin B are relatively low, but they have high biological significance respect to cancer diagnosis and treatment. The speed and required enzyme concentration in the electrochemical measurements can be significantly improved when this technique is used to detect other proteases with higher k_{cat}/K_m values, such as trypsin at (1.44 ± 0.1) x 10^6 $M^{-1}s^{-1}$,[64] α-thrombin at (1.0 ± 0.2) x 10^6 $M^{-1}s^{-1}$,[64] and plasmin at 6.7 x 10^5 $M^{-1}s^{-1}$.[131]

In previous electrochemical detection of proteases including trypsin,[64] a-thrombin,[64] and plasmin,[131] normal CV measurements on gold electrodes were used. This method was found not applicable on carbon electrode. As shown in Figure A.13, the Fc redox waves of the labeled tetrapeptide can be observed on the GCE, but the baseline currents were quite high, making it difficult to reliably extract redox signals. The previous studies on gold electrodes were able to block the nonfaradaic background current using close-packed self-assembled monolayer of small passivating alkane thiol molecules. The covalent bond of small passivating molecules does not allow them to move around to form a close-packed monolayer. Thus there were many leaking pinholes in the passivation layer on GCE. This is even more severe on VACNF NEA due to the curvature and inhomogeneity at the CNF surface. As a result, it was not possible to use CV to measure the Fc signal on VACNF NEAs. ACV provides a necessary solution for the reported enzymatic study.

While we have demonstrated that it is feasible to detect the enzymatic kinetics of both legumain and cathepsin B. It remains critical to evaluate the specificity for any practical applications. This will be carefully investigated in the future. Our preliminary data indicated that the specificity of protease detection using this reported method strongly depended on the value of the "specificity constant" k_{cat}/K_M. Cathepsin B has higher k_{cat}/K_M which resulted in ~75% of drop in the electrochemical signal due to cleavage to the designated tetrapeptide (see Figure

A.5). As a result, the exponential decay can be reliably measured, giving high specificity. In contrast, as shown in Figure A.14, the change of electrochemical signal is negligible using a tetrapeptide without Arg. For legumain, the low value of k_{cat}/K_M caused that the electrochemical signal only dropped by ~10% (see Figure 3.7a). The disturbance to the electrode during adding the enzyme solution caused uncontrollable fluctuation in the electrochemical signal. This limited precisely deriving the k_{cat}/K_M value. Therefore, the specificity for legumain is inconclusive at this stage and needs careful further study. But we can conclude that k_{cat}/K_M of $(1.13 \pm 0.38) \times 10^4$ $M^{-1}s^{-1}$ (as for legumain) is about the low limit for reliable protease measurements using the current setup.

3.5 Conclusions

In summary, we have demonstrated that high-frequency ACV can be applied on embedded VACNF NEAs to measure the redox reaction of Fc attached to the exposed CNF tip through a tetrapeptide and linker molecule. Due to the additional capacitive current pathway enabled by the unique interior graphitic microstructure of the VACNFs, the optimum frequency giving the highest peak AC current for Fc on VACNF NEA was found to be 40 times of that on GCEs. The higher frequency afforded a larger ACV signal and shorter time for the ACV measurements. Thus the kinetics of proteolysis of the surface-attached peptides can be measured upon addition of two types of cancer related proteases, i.e. legumain and cathepsin B. The kinetic process can be analyzed with a heterogeneous Michaelis-Menten model to derive the "specificity constant" k_{cat}/K_m, which is $(4.3 \pm 0.8) \times 10^4$ $M^{-1}s^{-1}$ for cathepsin B and $(1.13 \pm 0.38) \times 10^4$ $M^{-1}s^{-1}$ for legumain. These values are about 2 times of that measured with a fluorescence assay as well as the specifications provided by the vendor. The nanostructured electrode size clearly eliminated the steric effects for enzymatic reactions with surface-attached peptides. This is the

first example of the use of VACNF NEA on protease activity study. These VACNF NEA based electrochemical enzymatic biosensors can be potentially developed into portable multiplex electronic devices for rapid cancer diagnosis and treatment monitoring. Further study on the specificity and sensitivity of this VACNF NEA biosensor applied with biological samples is in progress toward this goal.

Chapter 4 - Quantitative electrochemical detection of cathepsin B activity in complex tissue lysates

Reproduced in part by permission of Elsevier.

Published as: Swisher, L. Z.; Prior, A. M.; Nguyen, T. A.; Hua, D. H.; Li, J. *Biosens. Bioelectron.* **2014**, *56*, 129-136.

4.1 Introduction

Cathepsin B is a lysosomal cysteine protease which is highly expressed during cancer invasion and progression.[152-154] Increased level of cathepsin B in tumors or in extracellular fluids can serve as prognostic factors for cancer patients.[155-156] It has been reported that cathepsin B is overexpressed in many cancer types, such as laryngeal cancer, oral cancer, breast cancer and colorectal cancer, compared to that in normal tissue.[157-161] Therefore simple and rapid detection of the expression level of cathepsin B, particularly quantitatively determine its enzymatic activity, is highly demanded for early diagnosis and treatment of cancers.[125]

Recently, we demonstrated a new approach by applying ACV on NEAs fabricated with embedded VACNFs to measure the activities of two cancer related proteases, legumain and cathepsin B.[1] The proteolytic kinetics of both proteases can be approximately analyzed with a heterogeneous Michaelis-Menten model.[1, 162] Cathepsin B is particularly interesting since its k_{cat}/K_M value was derived as $(4.3 \pm 0.8) \times 10^4$ $M^{-1}s^{-1}$, about four times of that of legumain, and hence can be reliably measured in a wider concentration range.

The ACV technique involved superimposing a sinusoidal AC voltage on the DC potential ramp, which can enhance the redox current from Fc moieties immobilized at the electrode surface by shuffling the electrons back and forth many times between the Fc moieties and the electrode.[47, 148] Particularly, applying ACV on the VACNF NEAs enabled the use of much

higher AC frequencies than on conventional macroscopic GCEs.[47] For Fc-appended tetrapeptide on VACNF NEAs, the maximum ACV peak current was at ~1,000 Hz, about 40 times of that on macro-GCEs.[1] The enhanced electrochemical signal and higher temporal resolution (< 1 min) are critical for measuring the fast enzymatic kinetics in this study.

However, the previous method[1] was found unable to consistently compare data collected from different electrodes due to the variation in electrochemical signals. Here we report a refined method for analyzing the kinetic ACV data of proteolysis of Fc-peptide attached on VACNF NEAs. Consistent quantitative analyses of cathepsin B activity at varied concentrations have been established. In addition, two critical steps toward rapid multiplex cancer diagnoses have been achieved. First, we demonstrate that this detection method is applicable on the whole tissue lysate of normal human breast samples, the tissue lysate spiked with varied concentrations of purified cathepsin B and the tissue lysate after immunoprecipitation. The relative cathepsin B concentrations in these complex samples are clearly correlated with the exponential rate. Second, a 3 x 3 microarray containing nine independently addressed regular VACNF NEAs by e-beam lithography showed substantially enhanced performance than the previously used non-patterned random VACNF NEAs. The measured activity of cathepsin B appeared to be much higher due to the smaller and well-defined CNF tips. These results demonstrated the great potential for this nanoelectronic method as a portable multiplex technique for simultaneously detecting a large number of distinct proteases in a minute drop of serum or lysate sample. This may enable quick analyses of a patient's protease profile, which is critical for rapid cancer diagnosis and treatment monitoring.

4.2 Quantitative analyses of purified cathepsin B activity

The insert of Figure 4.1a illustrates the principles of electrochemical assay for measuring the enzymatic activity of cathepsin B using VACNF NEAs. The tetrapeptides Leu-Arg-Phe-Gly labeled with electroactive Fc at the distal end are immobilized on the VACNF NEAs. Fc provides a reliable oxidation peak at ~0.25 V versus Ag/AgCl (3 M KCl) in ACV measurements. In our previous report[1], we have confirmed with HPLC and MS analyses that cathepsin B specifically cleaved the tetrapeptide at the site between arginine and phenylalanine. This releases the fragment containing Fc into the bulk solution and caused the peak current to decrease. The kinetics of the proteolytic reaction is monitored with continuously repeated ACV measurements. As reported in our previous studies[1, 47], a noteworthy advantage of ACV technique on Fc-attached VACNF NEAs is that the optimum AC frequency (800 to 1,800 Hz) was much higher than that on macro-GCEs (~40 Hz), leading to higher sensitivity and higher temporal resolution.

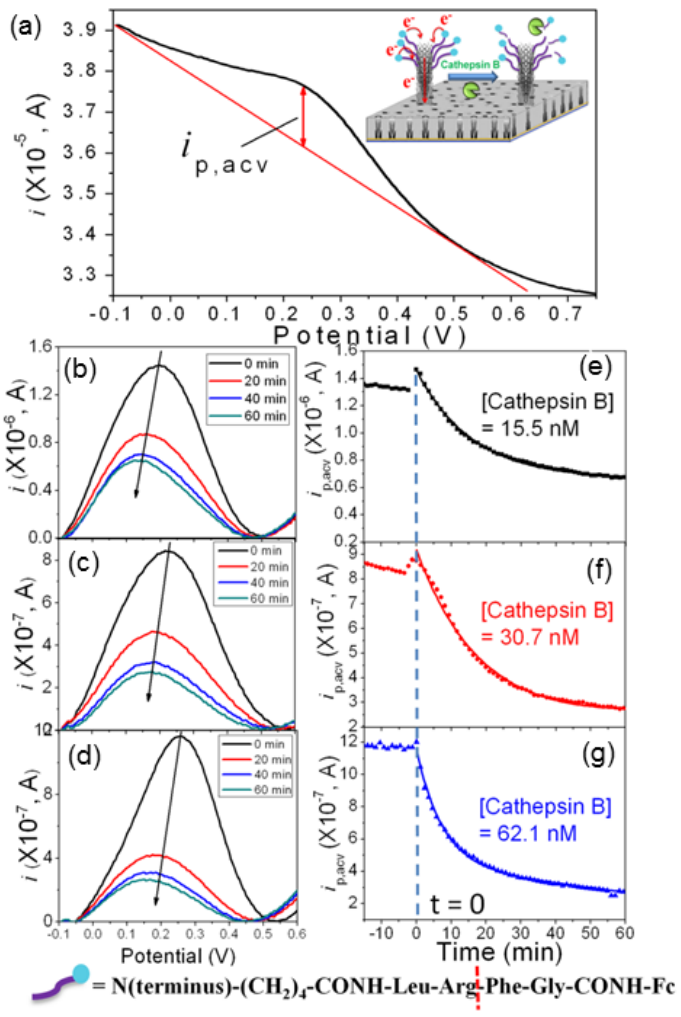

Figure 4.1 (a) A representative ACV of a random VACNF NEA immobilized with H_2N-$(CH_2)_4$-CO-Leu-Arg-Phe-Gly-NH-CH_2-Fc measured at AC frequency f = 800 Hz and AC voltage amplitude V_0 = 150 mV. Insert: Schematic of cathepsin B induced proteolytic cleavage of the tetrapeptide substrate. (b–d) Four representative background-subtracted ACVs from the continuously repeated ACV measurements after 25 µL of cathepsin B was added into the electrochemical cell. The final concentrations of cathepsin B were (b): 15.5 nM (0.5 ng·µL^{-1}); (c): 30.7 nM (0.9 ng·µL^{-1}); and (d): 62.1 nM (1.8 ng·µL^{-1}), respectively. (E–G) The change of ACV peak current $i_{p,acv}$ versus the reaction time while the cathepsin B solution at the

concentration corresponding to (b–d) was added to the electrochemical cell. The continuous lines are fitting curves to the proteolysis using Equation 4.1.

Figure 4.1a shows a representative ACV curve of H_2N-$(CH_2)_4$-CO-Leu-Arg-Phe-Gly-NH-CH_2-Fc immobilized on a random VACNF NEA. The AC peak current $i_{p,acv}$ can be derived by subtracting a linear background. Figures 4.1b-d show four representative background-subtracted ACV curves corresponding to 0, 20, 40 and 60 min, respectively, after adding the purified cathepsin B solution at three different final concentrations. The background-subtracted peak current $i_{p,acv}$ clearly decreased with the reaction time while the peak position slowly shifted from ~0.25 to ~0.15 V. Figures 4.1e-g illustrate the value of $i_{p,acv}$ from all ACVs versus the reaction time t. The value of $i_{p,acv}$ was relatively stable at the beginning. Adding the cathepsin B solution at $t = 0$ caused some disturbance to the $i_{p,acv}$ signal. Following that, all curves showed an exponential decay versus the reaction time which can be fit with:

$$i_t = i_0 \exp(-t/\tau) + (bt + c). \tag{4.1}$$

The values of the fitting parameters to Figure 4.1e–d are listed in Table B.1. Apparently, the value of i_0 correlated with the total amount of surface-functionalized peptide-Fc[47, 148], which varied with the density and exposed length of VACNFs in the NEAs. The term (bt + c), whose nature was not fully understood in our previous study[1], was found due to the Fc residues that were not cleavable by the protease. A large portion of them was attributed to physically trapped peptide-Fc at the Cr or embedded CNF surface due to the defects and pores in the SiO_2 insulating layer. Figure B.2 shows the ACV feature of physically trapped peptide-Fc on a random VACNF NEA by simply soaking the chip in 1.0 mM peptide-Fc solution for 2 hrs. There was also a possibility that some covalently attached peptide-Fc molecules might lie tightly on the VACNF

surface and cannot be cleaved by the protease due to the steric hindrance. Both factors may lead to the negative shift of ACV peak potential in Figure 4.1b–d.

Two "negative control" experiments were carried out to ascertain that the exponential decay of the $i_{p,acv}$ signal was attributed to specific proteolysis of cathepsin B by using a non-relevant peptide-Fc substrate H_2N-$(CH_2)_4$-CO-Ala-Ala-Asn-Leu-NH-CH_2-Fc and a peptide-Fc substrate with the specific cleavage site (i.e P1) –Arg- replaced by –Asn-, i.e. H_2N-$(CH_2)_4$-CO-Leu-**Asn-**Phe-Gly-NH-CH_2-Fc. As shown in Figure B.3a&b, the peak current $i_{p,acv}$ of these two tetrapeptides did not show the characteristic exponential decay while the activated cathepsin B was added into the electrochemical cell.

Apparently, the exponential decay of the $i_{p,acv}$ value after adding the protease represents the proteolysis kinetics. However, though each curve in Figure 4.1e-g can be analyzed separately, the raw $i_{p,acv}(t)$ values cannot be directly compared due to the variations in Fc-peptide quantity and background level from sample to sample. In order to normalize these varying factors, we define a new function S, referred as "extracted proteolytic signal", with

$$S = [i_t - (bt + c)]/i_0 = \exp(-t/\tau). \quad (4.2)$$

The extracted function S is essentially the exponential component of the kinetic data, whose decay time constant τ is directly related to the protease activity, as will be discussed later. As shown in Figure 4.2, the proteolytic measurements of different random VACNF NEAs at three cathepsin B concentrations are normalized to the same fractional scale using S, with all curves passing through (t = 0, S = 1.0). This allows clear view of the decay rate from different samples. The increase in cathepsin B concentration caused the function S to decay faster, giving smaller decay time constant τ and higher protease activity. This new method is critical for later studies requiring quantitative comparison of data from a large set of electrodes.

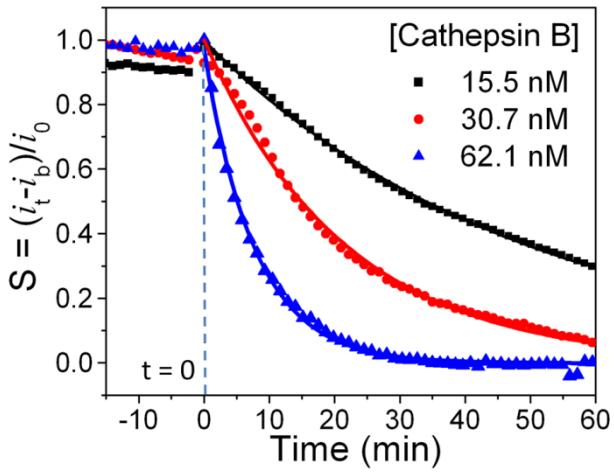

Figure 4.2 The proteolysis kinetics represented by the extracted proteolysis signal $S = (i_t - i_b)/i_0$ vs. the reaction time after adding purified cathepsin B into the electrochemical cell. The final concentrations of cathepsin B are 15.5, 30.7, and 62.1 nM, respectively. Each set of data was fitted with a simple exponential decay.

From our previous report[1], the proteolysis kinetics can be analyzed with a modified Michaelis-Menten model for heterogeneous enzymatic reactions [147]:

$$\mathrm{E} + \mathrm{S_s} \underset{k_{-1}}{\overset{k_1}{\longleftrightarrow}} \mathrm{ES_s} \xrightarrow{k_{\mathrm{cat}}} \mathrm{E} + \mathrm{P_s} + \mathrm{P}, \tag{4.3}$$

where E, S_s, ES_s, P_s and P represent the enzyme, surface-bound peptide substrate, enzyme-substrate complex on the electrode surface, surface-attached product, and product released to solution, respectively. The reaction rate υ can be defined as

$$\upsilon = -\frac{\mathrm{d}\Gamma_{S_S}}{\mathrm{dt}} = \frac{\mathrm{k_{cat}}[\mathrm{E_0}] \times \Gamma_{S_S}}{\mathrm{K_M} + [\mathrm{E_0}]}, \tag{4.4}$$

where Γ_{Ss} represents the surface density of active peptide substrate, k_{cat} is the dissociation rate constant and $K_M = (k_{cat}+k_{-1})/k_1$ is the Michaelis-Menten constant, respectively. Since "extracted

proteolytic signal" S is proportional to the surface densities of Fc-peptide substrates (i.e. $\Gamma_{Ss} \propto S$), Equation 4.4 can be rewritten as Equation 4.5 and, at low enzyme concentrations ($[E_0] << K_M$), an approximate relationship can be obtained as

$$\upsilon \propto -\frac{dS}{dt} = \frac{k_{cat}[E_0] \times S}{K_M + [E_0]} \approx \frac{k_{cat}[E_0] \times S}{K_M}, \tag{4.5}$$

The value of (-dS/dt) can be derived from Figure 4.2 and plot versus S in Figure 4.3a. Combining Equations 4.2 and 4.5, it gives

$$-\frac{dS/dt}{S} = \frac{k_{cat}}{K_M}[E_0] = \frac{1}{\tau}. \tag{4.6}$$

Therefore, the measured quantity $(k_{cat}/K_M)\cdot[E_0]$ can be represented by $1/\tau$ or the slope of Figure 4.3, with smaller τ giving larger $(k_{cat}/K_M)\cdot[E_0]$. The statistical value of $(k_{cat}/K_M)\cdot[E_0]$ derived from the slope of each lines in Figure 4.3a (i.e. -dS/dt versus S) was $(7.45 \pm 3.53) \times 10^{-4}$, $(1.25 \pm 0.30) \times 10^{-3}$ and $(2.15 \pm 0.37) \times 10^{-3}$ s^{-1} from nine experiments with enzyme concentration at 15.5, 30.7 and 62.1 nM, respectively. As shown in Figure 4.3b, the derived quantity $(k_{cat}/K_M)\cdot[E_0]$ is linearly proportional to the enzyme concentration $[E_0]$, consistent with the theoretical model. Since $[E_0]$ was known in the measurements shown in Figure 4.1&4.2, one can easily derive the concentration-independent "specificity constant" k_{cat}/K_M which is commonly used to represent the fundamental catalytic efficiency of different enzymes.

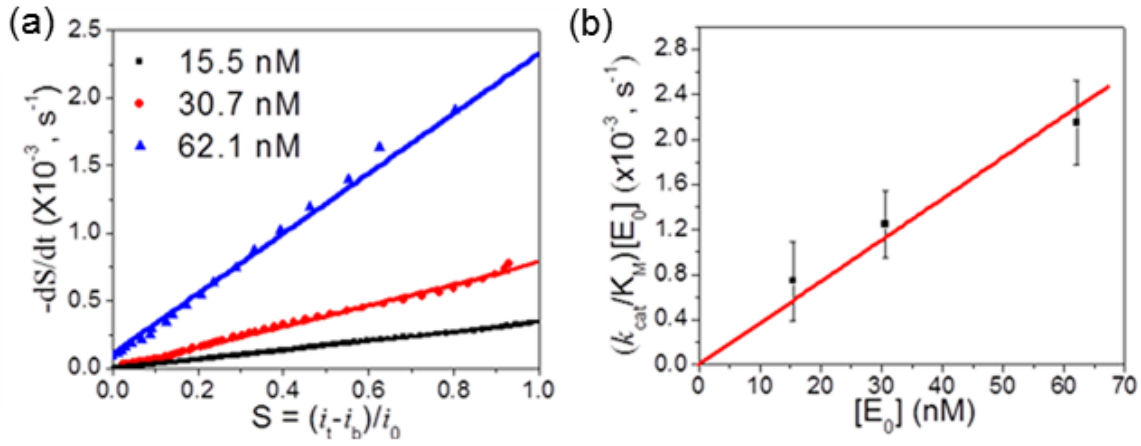

Figure 4.3 (a) Plot of the reaction rate -d*S*/dt versus extracted proteolysis signal S = $(i_t\text{-}i_b)/i_0$ at different cathepsin B concentrations. (b) Plot of $(k_{cat}/K_M)\cdot[E_0]$ with respect to cathepsin B concentration $[E_0]$ in the proteolytic reactions. The error bars are the standard deviation of the results from at least triplicated experiments.

The calculated k_{cat}/K_M values at three cathepsin B concentrations were very close to each other, giving an average value of 4.11 x 10^4 $M^{-1}s^{-1}$ and a standard deviation of 6.66 x 10^3 $M^{-1}s^{-1}$. Alternatively, fitting the data points in Figure 4.3b with a straight line passing through the origin gave a more accurate k_{cat}/K_M value of (3.68 ± 0.50) x 10^4 $M^{-1}s^{-1}$ that incorporated the results from all nine experiments at three discrete cathepsin B concentrations. These k_{cat}/K_M values are more accurate than our previous analyses[1] based on ACV measurements at a single enzyme concentration. The k_{cat}/K_M of the same batch of cathepsin B derived from nine fluorescence experiments right before the electrochemical measurements was (9.6 ± 4.1) x 10^4 $M^{-1}s^{-1}$, showing much larger standard deviation. However, all values are within the range of ~2 x 10^3 $M^{-1}s^{-1}$ to ~7 x 10^6 $M^{-1}s^{-1}$ in literature[147, 149-150] with a more extensive list showing in Table B.2. Importantly, the results confirmed that the k_{cat}/K_M value by ACV measurements remained constant as the cathepsin B concentration varied, establishing a method to determine the cathepsin B activity in

an unknown sample by dividing the measured $(k_{cat}/K_M)\cdot[E_0]$ with the above k_{cat}/K_M value.

4.3 Detecting cathepsin B activity in complex tissue lysates

Normal human tissues may contain many proteases including cathepsin B and their expression at higher level is expected in cancerous tissues. To demonstrate that ACV coupled with VACNF NEAs is viable for detecting protease activities in complex human samples, we have carried out three sets of measurements using lysates from human breast tissue. The cathepsin-B-specific tetrapeptide H_2N-$(CH_2)_4$-CO-Leu-Arg-Phe-Gly-NH-CH_2-Fc was immobilized on random VACNF NEAs. The human breast whole tissue lysate (adult normal) was first treated with the activation buffer similar to the purified cathepsin B experiments. 25 µL of the activated lysate solution was then added into the electrochemical cell containing 250 µL of 25 mM MES (pH 5.0) while the ACV measurement was continuously repeated. In Figure 4.4a, the final concentrations of the lysate were 20.0 $\mu g\cdot mL^{-1}$ and 29.1 $\mu g\cdot mL^{-1}$, diluted by 245 and 168 fold, respectively from the purchased tissue lysate stock solution. Both lysate samples caused exponential decay after being added into the electrochemical cell, as shown in the "extracted proteolytic signal" $S = (i_t - i_b)/i_0$ with $i_b = bt + c$. The fitted time constants are $\tau_0 = 725$ s and $\tau_0' = 1647$ s at the lysate concentration of 29.1 and 20.0 $\mu g\cdot mL^{-1}$, respectively. The derived $(k_{cat}/K_M)\cdot[E_0]$ values are $6.04 \times 10^{-4}\ s^{-1}$ for 20.0 $\mu g\cdot mL^{-1}$ tissue lysate and much higher at $1.38 \times 10^{-3}\ s^{-1}$ for 29.1 $\mu g\cdot mL^{-1}$ tissue lysate. Using $k_{cat}/K_M = (3.68 \pm 0.50) \times 10^4\ M^{-1}s^{-1}$ derived from the purified cathepsin B solutions in Figure 4.3, the equivalent cathepsin B concentrations were calculated as ~(16.4 ± 2.2) nM in the 20.0 $\mu g\cdot mL^{-1}$ tissue lysate, and ~(37.5 ± 5.1) nM in the 29.1 $\mu g\cdot mL^{-1}$ tissue lysate. Due to the existence of the experimental deviation and activity variation of biology sample, they did not present a perfect linear relationship but were close.

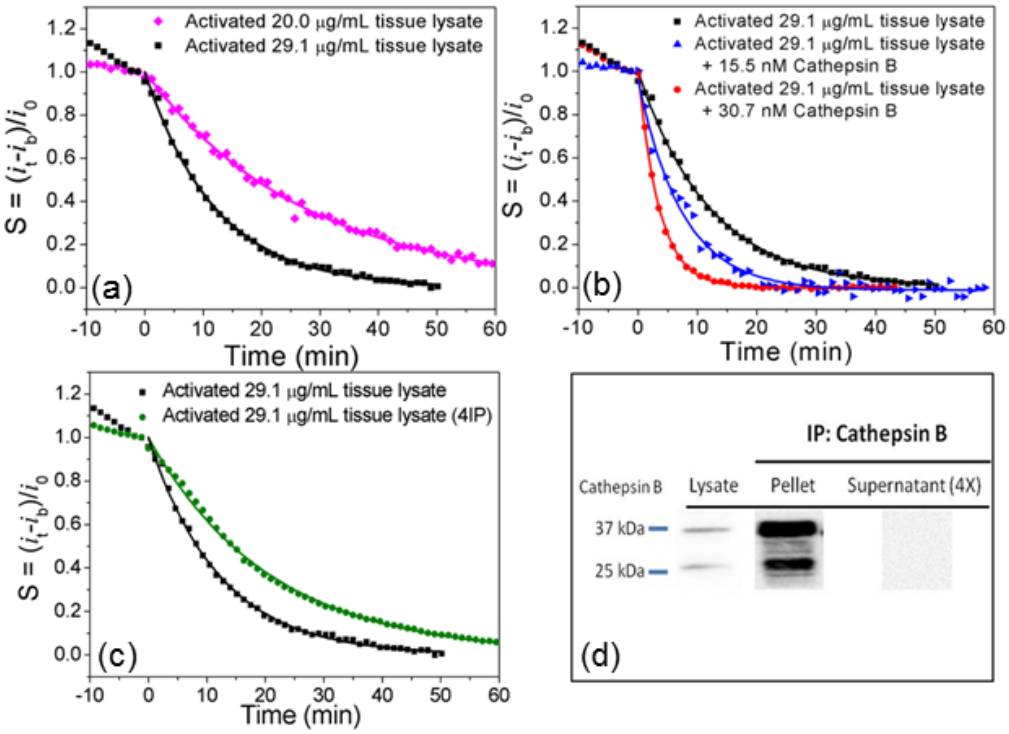

Figure 4.4 The proteolysis curves of (a) 20.0 μg·mL^{-1} (pink diamond) and 29.1 μg·mL^{-1} (black square) of the whole breast tissue lysate (normal adult human); (b) 29.1 μg·mL^{-1} whole tissue lysate (black square) and this tissue lysate spiked with 0.9 μg·mL^{-1} (30.7 nM) (red dot) and 0.5 μg·mL^{-1} (15.5 nM) (blue triangle) cathepsin B, respectively; and (c) 29.1 μg·mL^{-1} tissue lysate before (black square) and after four rounds of immunoprecipitation (4IP) in order to deplete the cathepsin B (green dot). All ACV measurements were carried out at f = 800 Hz and AC voltage amplitude V_0 = 150 mV. (d) Western blot analysis using cathepsin B antibody: Lysate lane – 25.0 μg of the original whole tissue lysate; Pellet lane – the immunoprecipitated fraction of 0.5 mg of tissue lysate using cathepsin B antibody; Supernatant lane – the supernatant fraction after four rounds of immunoprecipitation. The proenzyme cathepsin B is ~37 kDa and the active cathepsin B is ~25 kDa.

As 15.5 and 30.7 nM purified cathepsin B were spiked into the 29.1 $\mu g \cdot mL^{-1}$ tissue lysate, the decay became faster, giving τ_1 = 433 s and τ_2 = 213 s, respectively (Figure 4.4b). Clearly, substantial proteolysis was catalyzed by cathepsin B. To further confirm that the measured decay was from the specific proteolysis of peptide-Fc by cathepsin B, an immunoprecipitation (IP) assay was employed to partially remove cathepsin B from the tissue lysate. The exponential decay was indeed much slower, giving τ_4 = 1246 s (Figure 4.4c), but some substantial decay feature was retained. It is likely that some cathepsin B still retained in the tissue lysate after four rounds of IP but the level was below the sensitivity of Western blot analysis shown in Figure 4.4d. It is also possible that other proteases (particular other cathepsins, such as cathepsin L and V) may cleave the tetrapeptide although the catalytic activity may be lower.

Quantitative estimation of cathepsin B activity in the tissue lysate can be made based on the results shown in Figure 4.4b. First, according to Equation 4.6, we can derive the difference between the 15.5 nM spiked and unspiked samples as:

$$(k_{cat}/K_M)\cdot([E_0] + 15.5\ nM) - (k_{cat}/K_M)\cdot[E_0] = 1/\tau_1 - 1/\tau_0 = 9.30 \times 10^{-4}\ s^{-1}, \quad (4.7)$$

which gives $k_{cat}/K_M = 6.0 \times 10^4\ M^{-1}s^{-1}$. This value is slightly higher than the value $(4.11 \pm 0.67) \times 10^4\ M^{-1}s^{-1}$ obtained with purified cathepsin B in buffer solutions as discussed above. For the tissue lysates with and without IP procedure, we have

$$(k_{cat}/K_M)\cdot\Delta[E_0] = 1/\tau_0 - 1/\tau_4 = 5.77 \times 10^{-4}\ s^{-1}. \quad (4.8)$$

Thus the difference in cathepsin B concentration $\Delta[E_0]$ is equivalent to ~14 ± 2.3 nM cathepsin B in buffer solution if we use the value $k_{cat}/K_M = (4.11 \pm 0.67) \times 10^4\ M^{-1}s^{-1}$ discussed above. Though refinements are needed to reduce the error bar, it is clear that this method is applicable in complex tissue lysate samples. This study established a critical step toward developing meaningful diagnosis tools. *To our knowledge, this is the first time that the activity of*

a protease has been quantitatively determined by electrochemical methods with complex whole tissue lysates.

The cathepsin B activity in the normal human breast whole tissue lysate was also validated by the fluorescence method using a short peptide substrate Z-Leu-Arg-AMC. The very small exponential curvature in Figure B.4 gave a much lower value of $(k_{cat}/K_M)\cdot[E_0]$ (~4.98 x 10^{-5} s^{-1}) than that obtained from the electrochemical measurement (~1.38 x 10^{-3} s^{-1}), although the lysate concentration was much higher (0.24 $mg\cdot mL^{-1}$ vs. 29.1 $\mu g\cdot mL^{-1}$). But the lysates spiked with 11.9 and 23.9 nM purified cathepsin B showed clear exponential increases in fluorescence signal (Figure B.5) due to proteolysis, which validated that the electrochemical signal was indeed due to cathepsin B.

4.4 Toward multiplex detection with regular VACNF NEAs

In long term, regular VACNF NEAs can be mass-produced as multiplex chips on independently addressed microelectrode pads using UV- and e-beam lithography[119]. Such chips can be integrated into portable electronic systems for profiling a set of proteases. Figure 4.5a and B.1 show nine 200 μm x 200 μm microelectrode pads of ~100 nm-thick Cr film in a 3 x 3 array on a SiO_2-covered Si wafer. VACNFs were grown in regular 1 μm x 1 μm lattice on these microelectrode pads to form embedded NEAs which were independently connected with the measuring circuits through larger (1 mm x 1 mm) contact pads at the top of Figure B.1a (not shown). Figure 4.5b shows the zoom-in image of exposed VACNF tips of ~100 nm in diameter and ~150 nm length protruding over the SiO_2 matrix. Figure B.6a shows the CVs of a 50 mM $K_3Fe(CN)_6$ solution from all nine VACNF NEAs. Clearly, they all showed the characteristic sigmoidal shape with low background and almost identical limiting current, indicating the high uniformity of these NEAs.

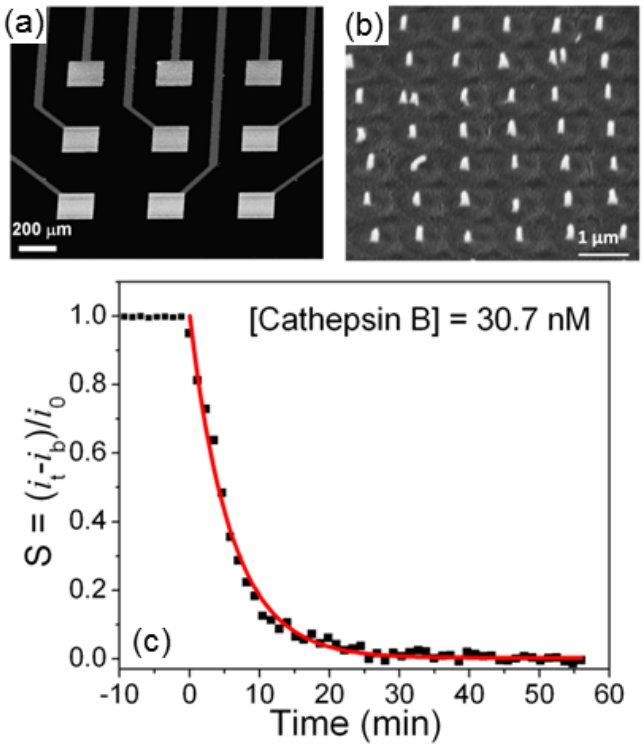

Figure 4.5 SEM images at 45° perspective view of (a) a 3 x 3 VACNF NEA chip, and (b) the e-beam patterned regular VACNF NEA partially embedded in SiO_2 matrix at each microelectrode pad. (c) The extracted proteolysis signal $S = (i_t\text{-}i_b)/i_0$ was derived from continuously repeated ACV measurements while 25 μL of purified cathepsin B was added into the electrochemical cell to a final concentration of 30.7 nM (0.9 ng·μL^{-1}). All ACV measurements were carried out at f = 800 Hz and AC voltage amplitude V_0 = 150 mV.

The covalently attached tetrapeptide $H_2N\text{-}(CH_2)_4\text{-}CO\text{-}Leu\text{-}Arg\text{-}Phe\text{-}Gly\text{-}NH\text{-}CH_2\text{-}Fc$ on the e-beam patterned regular VACNF NEA present a similar ACV peak at ~0.25 V as shown in Figure B.6c. The peak shape was much better defined than the random VACNF NEAs. Similar as before, the ACV peak can be extracted by subtracting a linear background. Figure B.6d shows that the ACV peak current monotonically decreased after a purified cathepsin B solution was added into the electrochemical cell to give a final concentration of 30.7 nM. The peak potential

also continuously downshifted to ~0.10 V. The completed kinetic curve of raw $i_{p,acv}$ during proteolysis is presented in Figure B.7a. The $i_{p,acv}$ amplitude decayed much faster in the initial reaction period but then leveled off after ~35 min. Similar to the random VACNF NEAs, the leveled $i_{p,acv}$ was attributed to physically trapped peptide-Fc in the SiO_2 matrix as confirmed by the control experiment shown in Figure B.7b. While such background can be reduced in the future by improving SiO_2 deposition and passivation, it can be easily excluded using the "extracted proteolysis signal" $S = (i_t - i_b)/i_0$ discussed earlier.

The kinetic curves of S vs. the reaction time after adding 30.7 nM purified cathepsin B is shown in Figure 4.5c. The fitted exponential decay time constant τ was 353 s, clearly smaller than 800 ± 192 s obtained with random VACNF NEAs at the same cathepsin B concentration. From either the fitted slope of $-dS/dt$ versus S or τ value, $(k_{cat}/K_M)\cdot[E_0]$ was calculated as 2.81 x 10^{-3} s^{-1}, about twice of the statistical value (1.25 ± 0.30) x 10^{-3} s^{-1} on the random VACNF NEA at 30.7 nM cathepsin B concentration. Accordingly, the specificity constant k_{cat}/K_M was 9.2 x 10^4, about twice of (4.11 ± 0.67) x 10^4 $M^{-1}s^{-1}$ measured with random VACNF NEAs. Clearly, the regular VACNF NEAs worked much better than the random VACNF NEAs. The smaller diameter (~100 nm vs. 150 nm) may help to reduce the steric hindrance for enzymes to interact with the immobilized peptide. The uniform size and exposed length as well as the regular spacing of the CNFs made the regular VACNF NEAs more reproducible and perform better than the random VACNF NEAs.

4.5 Conclusions

We have demonstrated electrochemical detection and kinetic analysis of cathepsin B activity in proteolysis of Fc-appended tetrapeptides that are immobilized on VACNF NEAs using enhanced AC voltammetry. A normalization algorithm was used to extract the proteolysis

signal from the largely varied raw data, which enabled consistent comparison and quantitative analyses of cathepsin B activity. This algorithm was first validated with purified cathepsin B solutions and then demonstrated in complex lysates of human breast tissue, the lysates spiked with purified cathepsin B, and the immunoprecipitated lysate. The cathepsin B concentration in normal tissue lysate can be quantitatively assessed by comparing these results. The regular VACNF NEAs fabricated with precise e-beam lithography showed faster kinetics of cathepsin B proteolysis, illustrating the potential for further improving detection sensitivity. This electrochemical method has great potential as a portable multiplex system for simple and rapid protease profiling of lysate, serum, or blood samples, which may be used in cancer diagnosis and treatment monitoring.

Chapter 5 - Quantitative electrochemical detection of cathepsin B activity in breast cancer cell lysates toward identification of cancer formation

Reproduced in part from manuscript submitted by Swisher, L. Z.; Prior, A. M.; Gunaratna, M. J.; Shishido, S.; Madiyar, F.; Nguyen, T. A.; Hua, D. H.; Li, J. (under review)

5.1 Introduction

Breast cancer is the most common type of cancers, with about 235,000 new cases expected in the United States in 2014, followed by prostate and lung cancer.[25] The most useful prognostic parameters for cancer recurrence and progression are the tumor grade, the depth of tumor penetration (stage) and the presence of carcinoma in situ.[163] Quantitative detection of molecular biomarkers that are involved in breast tumor progression is another important avenue for cancer diagnosis and treatment. It is known that cancer metastasis involves proteases, a group of enzymes that cause proteolysis to degrade the extracellular matrix (ECM) components and intercellular cohesive structures of neighboring cells leading to the activation of growth and angiogenic factors,[164-165] which could serve as biomarkers for diagnosis.[49] Among them, cathepsin B is a representative prognostic marker for human lung cancer[57] and breast cancer.[166]

Cathepsin B is a papain-family cysteine protease synthesized as glycosylated proenzyme of ~37 kDa and subsequently converted to the active form of ~25 kDa [by sodium dodecyl sulfate polyacrylamide gel electrophoresis (SDS-PAGE)] after the proteolysis of the signal sequence.[167-168] Of the cysteine proteases, cathepsin B has been most often implicated in invasive and malignant phenotype of tumors including brain, breast, lung, pancreas, bladder, prostate and stomach.[169] ELISA has been commonly used to measure the cathepsin B concentrations in urine,

serum, and tissue lysates. Kotaska et al. found that cathepsin B concentrations have been significantly elevated in the serum and urine samples from bladder cancer patients and correlated well with grading and invasivity of tumors.[163] Chen's group claimed that the serum level of cathepsin B was significantly higher in the lung cancer patients compared to the healthy controls.[170] Using immunochemical staining of tissue section and immunoblotting of cell lysates, Nouh et al. found that there was a positive correlation between the expression of cathepsin B and the number of positive metastatic lymph nodes in inflammatory breast cancer.[166] By studying the microdissected frozen tissue sections of human tumors from colon and breast carcinoma, a group of researchers found a significant increase in the level of cathepsin B in regions of invasive tumor as compared to normal epithelium from the same patients.[171]

Although ELISA and immunohistochemical methods can sensitively detect the concentration of specific proteases, they are typically time-consuming and can only measure one protease each time. In contrast, electrochemical technology has superior advantages such as its simple electronic readout and potential for simultaneous detection of multiple proteases using an electrode array, making it more suitable for rapid point-of-care diagnosis, treatment monitoring, and drug (protease inhibitor) screening. In addition, it detects the activity instead of concentration of proteases, which is more relevant to biological processes. However, there is very limited study of the activities of cancer-related proteases in complex human tissues or cancer cell lysates using electrochemical methods. In previous studies, we have demonstrated an electrochemical technique in detecting the proteolytic kinetics of two cancer-related proteases legumain and cathepsin B in purified solutions and complex whole tissue lysates, respectively, using NEAs fabricated with VACNFs a special type of carbon nanotubes.[1-2] Specific tetrapeptides with a Fc group at the distal end were attached to the exposed VACNF tip and

selectively cleaved by the proteases. The unique structure of VACNFs allowed using a high-frequency (~1 kHz) ACV to monitor the small electrochemical signal from Fc.[1-2, 47, 57] In this report, we further apply this technique on detection of cathepsin B activities in four types of cell lysates including normal and breast cancer cells. The cathepsin B activities were found increased from normal to cancer cells and reached highest value in metastatic cancer cell lysate. A specific inhibitor clearly suppressed the activity of cathepsin B in the cell lysate. Our results showed that this NEA-based electrochemical method has great potential as a portable multiplex system for simple and rapid protease profiling of lysate, serum or urine samples toward early cancer diagnosis, treatment monitoring, and drug screening.

5.2 Cell characterization: Western blot analysis and IP assay

The expression of cathepsin B in normal breast cells HMEC, non-tumorigenic breast cells MCF-10A, breast cancer cells T47D and metastatic cancer cells MDA-MB-231 was first subjected to Western blot analysis. It is known that cathepsin B presents in two forms, i.e. proenzyme and active form, with the molecular weight of ~37 kDa and ~25 kDa, respectively, by SDS-PAGE.[167] Incubated in activation buffer consisting of 5 mM DTT and 25 mM MES converts a portion of pro cathepsin B into the active enzyme.[167] The Western blot results in Figure C.6a clearly show the presence of both pro and active forms of cathepsin B in WCE of all breast cells, with the content of the active form generally higher than that of the pro form. It needs to be noted that the band intensity among the four cell lysates in Figure C.6a varied due to different sample loading and immunoblotting conditions, as indicated by the control Western blot results of actin in these samples (see Figure C.1). In order to prove the electrochemical signal decay is indeed due to proteolysis from cathepsin B, cathepsin B-depleted lysate samples were used. Cathepsin B was precipitated out from the same amount of WCEs using cathepsin B

antibody. The pellets (the immunoprecipitated fraction) containing the concentrated and purified cathepsin B were then subjected to Western blot analyses all in one run. Figure C.6b and Table C.1 illustrate that, with the same initial loading of 500 µg WCE, the total integrated pixel intensity of cathepsin B in the Western blot bands increased in cancer cell lysates. The linear relationship of the Western blot band intensity with the amount of enzyme was verified with experiments using purified cathepsin B (Figure C.2). After one round of IP, small but detectable amount of cathepsin B still present in the supernatant of the lysate (shown in 1X column of Figure C.6a). However, no obvious amount of cathepsin B was found in the supernatant after 2 to 3 times of IP (shown in the 3X column of Figure C.6a), indicating a complete removal of cathespin B in the sample.

5.3 Electrochemical study of proteolysis of breast cancer cell lysates (MDA-MB-231)

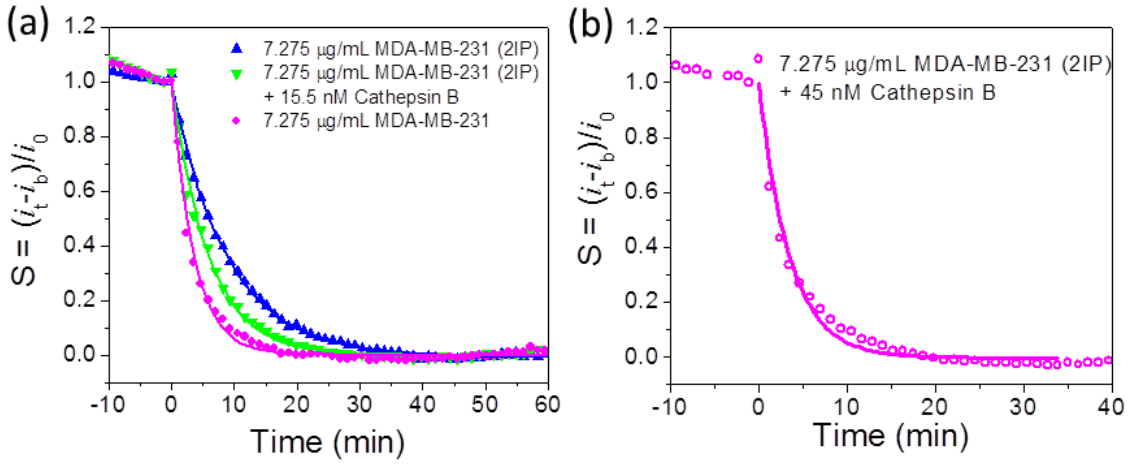

Figure 5.1 The normalized proteolysis curves of (a) 7.28 µg·mL^{-1} MDA-MB-231 cell extract with cathepsin B partially removed by two times immunoprecipitation (2IP) (blue triangle), this sample spiked with ~13.3 nM (0.45 µg·mL^{-1}) purified cathepsin B (green inverted triangle), and

7.28 μg·mL^{-1} MDA-MB-231 whole cell extract (pink dots); (b) 7.28 μg·mL^{-1} 2IP MDA-MB-231 cell extract spiked with ~38.0 nM (1.30 μg·mL^{-1}) purified cathepsin B. All ACV measurements were carried out at f = 800 Hz and AC voltage amplitude V_0 = 150 mV.

The electrochemical detection of cathepsin B activity in the breast cancer cell followed the method in our previous study.[2] The direct lysate of breast cancer cell MDA-MB-231 and that with cathepsin B removed by two rounds of IP (denoted as 2IP) have been studied. The cathepsin B specific tetrapeptide H_2N-$(CH_2)_4$-CO-Leu-Arg-Phe-Gly-NH-CH_2-Fc was immobilized on VACNF NEAs as the substrate for the enzymatic reaction. Twenty five μL of the activated lysate sample was added into the electrochemical cell containing 250 μL of 25 mM MES (pH 5.0) while ACV signal from the Fc-appended tetrapeptide was repeatedly recorded. In Figure 5.1a, the final total protein concentration of the lysate is 7.28 μg·mL^{-1}. Adding both lysate samples caused kinetic exponential decay in the extracted electrochemical signal S. The fitted time constants are τ_1 = 215 s for MDA-MB-231 cell lysate (pink dots) and τ_2 = 533 s for the cathepsin B-removed lysate (blue triangle). Cathepsin B-removed lysate (by 2IP) showed 2.5 times slower kinetic decay rate compared to the direct lysate. In order to confirm that the difference of decay rate is indeed due to the removal of cathepsin B, 13.3 nM cathepsin B was spiked into the 7.28 μg·mL^{-1} cathepsin B-removed MDA-MB-231 lysate (green inverted triangle). The decay time was shortened from τ_2 = 533 s to τ_3 = 352 s.

According to Equation 4.6, the value of k_{cat}/K_M can be derived by:

$$(k_{cat}/K_M)\cdot([E_0] + 13.3\ \text{nM}) - (k_{cat}/K_M)\cdot[E_0] = 1/\tau_3 - 1/\tau_2 = 0.96 \times 10^{-3}\ s^{-1}, \quad (5.1)$$

which gives k_{cat}/K_M = 7.22 x 10^4 M^{-1}s^{-1}. This value is slightly larger than our previous result, 4.90 x 10^4 M^{-1}s^{-1} which derived from the purified cathepsin B.[2] We can also obtain the difference of cathepsin B in direct and cathepsin B-removed MDA-MB-231 lysates as following:

$$(k_{cat}/K_M)\,\Delta E_0 = 1/\tau_1 - 1/\tau_2 = 2.77 \times 10^{-3}\ s^{-1}. \quad (5.2)$$

Since k_{cat}/K_M equals to $7.22 \times 10^4\ M^{-1}s^{-1}$ according to above calculation, the difference of cathepsin B in 7.28 μg·mL^{-1} MDA-MB-231 lysate and cathepsin B-removed lysate, i.e. ΔE_0, can be calculated as ~38 nM. To investigate whether our calculation is legitimate, we spiked 38 nM (1.30 μg·mL^{-1}) cathepsin B into 7.28 μg·mL^{-1} cathepsin B-removed MDA-MB-231 lysate. A similar decay time $\tau_4 = 207$ s (versus $\tau_1 = 215$ s in 7.28 μg·mL^{-1} of original MDA-MB-231 cell lysate) was obtained as shown in Figure 5.3b, validating that the higher proteolytic rate was indeed due to high cathepsin B concentration.

In principle, the 2IP cell lysate should not cause any exponential decay in contrast to the significant decay in Figure 5.1a. In previous studies,[1-2] we have demonstrated that the tetrapeptide H_2N-$(CH_2)_4$-CO-Leu-Arg-Phe-Gly-NH-CH_2-Fc can be selectively cleaved by cathepsin B but not legumain. However, the cell lysate contain many unknown proteases which could cleave the tetrapeptide at any possible sites. To identify a highly selective peptide remains a big challenge of today's research. Our future studies will focus on screening the peptides with the optimum selectivity from a large library of peptide substrates.

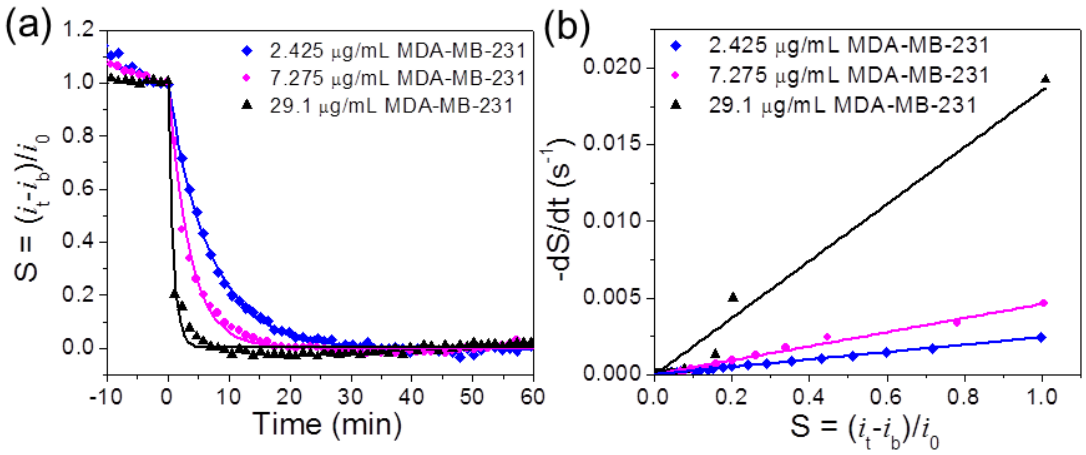

Figure 5.2 The normalized proteolysis curves of (a) 2.43 μg·mL^{-1} (blue diamond), 7.28 μg·mL^{-1} (pink dots) and 29.1 μg·mL^{-1} (black triangle) MDA-MB-231 whole cell extract. (b) Plot of – dS/dt vs S during the proteolytic reaction by the cell extracts demonstrated in panel A. The slope is equal to the inverse of the exponential decay, i.e. 1/τ. All ACV measurements were carried out at f = 800 Hz and AC voltage amplitude V_0 = 150 mV.

The proteolysis of tetrapeptide H_2N-$(CH_2)_4$-CO-Leu-Arg-Phe-Gly-NH-CH_2-Fc by different concentrations of MDA-MB-231 cell lysates was also studied. As shown in Figure 5.2a, the decay rate increases with the increasing concentrations of MDA-MB-231 lysates. The decay time constants are 53 s, 215 s and 410 s for 29.1, 7.28 and 2.43 μg·mL^{-1} MDA-MB-231 cell lysates, respectively. According to Equation 4.6, $(k_{cat}/K_M)\cdot[E_0]$ can be represented by 1/τ or the slope of Figure 5.2b (i.e., -dS/dt versus S). The values of $(k_{cat}/K_M)\cdot[E_0]$ derived from the slope were 1.86 x 10^{-2}, 4.60 x 10^{-3} and 2.42 x 10^{-3} s^{-1} with lysate concentration at 29.1, 7.28 and 2.43 μg·mL^{-1}, respectively. The quantity of $(k_{cat}/K_M)\cdot[E_0]$ deviated from linear relationship at the low lysate concentration $[E_0]$ = 2.43 μg·mL^{-1}, posing the low limit of lysate concentration for quantitative analysis. However, the results showed that this technique can reliably measure the protease above ~2.43 μg·mL^{-1}.

5.4 Specificity study by using cathepsin B inhibitor GC-373

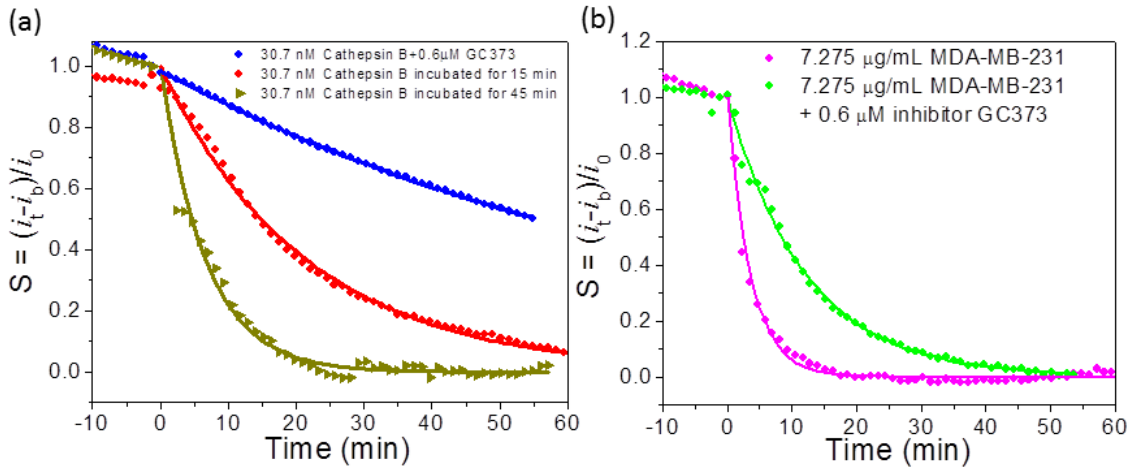

Figure 5.3 (a) The normalized proteolysis curves of 30.7 nM (0.89 μg·mL^{-1}) purified recombinant cathepsin B after (1) normal activation procedure by incubation for 15 min in the activation buffer (5 mM DTT and 25 mM MES buffer, pH 4.0) (red dot), (2) with additional 30 min incubation after the normal activation (dark yellow triangle), and (3) adding 0.6 μM inhibitor GC-373 during the 30 min additional incubation (blue diamond). (b) The normalized proteolysis curves of 7.28 μg·mL^{-1} MDA-MB-231 incubated for 30 min with (green dot) and without (pink dot) adding 0.6 μM inhibitor GC-373 after the normal 15 min activation procedure.

To assess the specificity of the electrochemical detection of cathepsin B activity, an inhibitor GC-373 which inhibits the activity of cathepsin B was applied. The IC_{50} value of 9.67 nM was first measured with the fluorescence assay (Figure C.4). The proteolysis of tetrapeptide H_2N-$(CH_2)_4$-CO-Leu-Arg-Phe-Gly-NH-CH_2-Fc by purified recombinant cathepsin B with and without inhibitor was then measured as shown in Figure 5.3a. Three sets of measurement were

done with 30.7 nM cathepsin B: (1) with normal 15 min activation in the activation buffer (5 mM DTT and 25 mM MES buffer, pH = 5.0); (2) with extra 30 min incubation following the normal activation; and (3) with 30 min incubation with added 0.6 μM GC-373 inhibitor following the normal activation. Since the inhibitor requires 30 min incubation with the activated cathepsin B for it to take effects, experiment 2 is needed as the control. The decay time for the cathepsin B being activated for 15 min is 1287 s, giving $(k_{cat}/K_M)\cdot[E_0]$ (= $1/\tau$) equals to 7.77 x 10^{-4} s^{-1}. With further incubation for 30 min, the enzyme is more active, giving a smaller decay time of 397 s. After adding the GC-373 inhibitor, the decay time dramatically increases to 4,812 s. Accordingly, the cathepsin B activity $(k_{cat}/K_M)\cdot[E_0]$ dropped by ~12 fold from 2.52 x 10^{-3} s^{-1} to 2.08 x 10^{-4} s^{-1}. The same trend was also found by using fluorescence method shown in Figure S5. The above results implied that inhibitor GC-373 is an efficient inhibitor for cathepsin B. Furthermore, Figure 5.3b showed that inhibitor GC-373 treated cancer cell lysate MDA-MB-231 also exhibited 3.4 fold lower proteolysis activity compared to the untreated lysate, with $(k_{cat}/K_M)\cdot[E_0]$ of 1.37 x 10^{-3} s^{-1} vs. 4.65 x 10^{-3} s^{-1} and the decay time constant of 729 s vs. 215 s. This result illustrated that cathepsin B was the major protease responsible to the cleavage of the tetrapeptide H_2N-$(CH_2)_4$-CO-Leu-Arg-Phe-Gly-NH-CH_2-Fc in the electrochemical measurements, but other proteases in cancer cell lysate MDA-MB-231 also made some contributions.

5.5 Comparison of proteolysis kinetics of different breast cell lysates

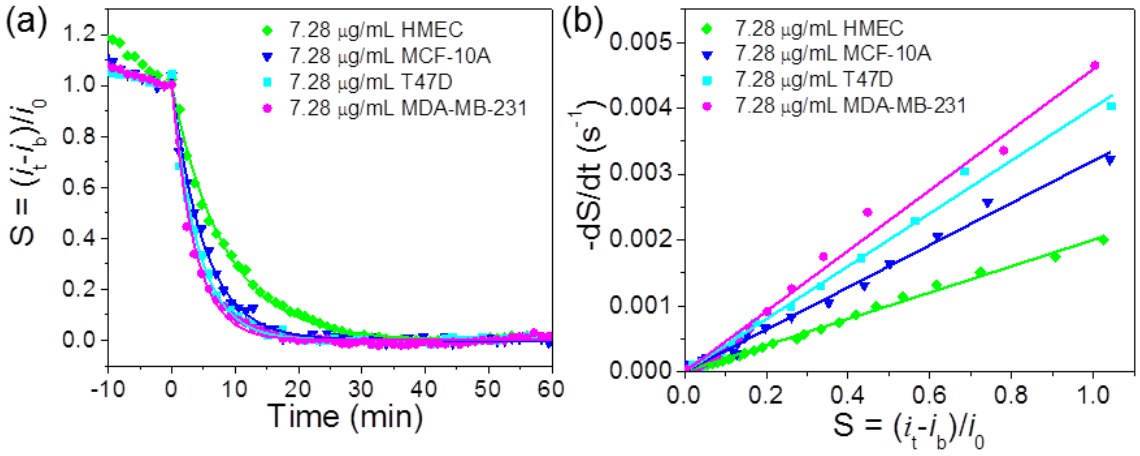

Figure 5.4 (a) The normalized proteolysis curves of 7.28 μg·mL^{-1} of HMEC cell extract (green diamond), MCF-10A cell extract (blue inverted triangle), T47D cell extract (cyan square) and MDA-MB-231 cell extract (pink diamond), respectively. (b) The plot of –dS/dt vs. S during the enzymatic reaction of the cell extracts in panel a.

A major goal of today's research is to develop methods that can quantitatively detect protease in complex samples and correlate the results with cancer formation. Toward this goal, one type of primary culture cells and three different breast cell lines were used to investigate whether the electrochemical detection of cathepsin B activity using VACNF NEAs could have biological significance. A solution of 25 μL of normal mammary cell HMEC lysate, non-tumorigenic breast cell MCF-10A lysate, breast cancer cell T47D, or metastatic breast cell MDA-MB-231 lysates at total protein concentration of 7.28 μg·mL^{-1} was added into the electrochemical cell filled with 250 μL of 25 mM MES buffer (pH = 5.0). The decay time clearly varied among these different cell lysates (Figure 5.4a) giving τ = 497, 311, 248 and 215 s for 7.28 μg·mL^{-1} of HMEC, MCF-10A, T47D, and MDA-MB-231, respectively. The values of

(k_{cat}/K_M)·[E_0] derived from 1/τ or the slope of –dS/dt versus S are 2.00 x 10^{-3}, 3.20 x 10^{-3}, 4.02 x 10^{-3} and 4.60 x 10^{-3} s^{-1} accordingly (Figure 5.4b).

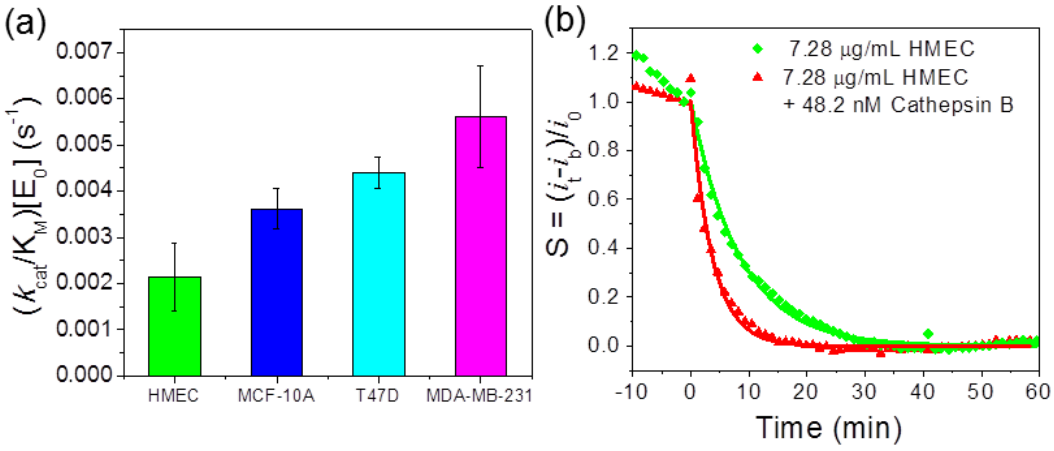

Figure 5.5 (a) Comparison of the (k_{cat}/K_M)·[E_0] values derived from 7.28 µg·mL^{-1} HMEC, MCF-10A, T47D and MDA-MB-231 cell extracts reacting with tetrapeptide H_2N-$(CH_2)_4$-CO-Leu-Arg-Phe-Gly-NH-CH_2-Fc on VACNF NEAs. The error bars represent standard deviation from the mean from three measurements. (b) The normalized proteolysis curves of 7.28 µg·mL^{-1} HMEC cell extract spiked with 48.2 nM (1.63 µg·mL^{-1}) purified cathepsin B. The AC measurements were carried out at f = 800 Hz and AC voltage amplitude V_0 = 150 mV.

Most of the early stage mammary tumors are ER-positive and many patients could respond to anti-estrogen or endocrine therapy[172-175] and later stage breast cancers become resistant to endocrine therapy and are more malignant, aggressive, invasive and metastatic[176-180]. HMEC is derived from normal mammary tissue, and MCF-10A is a non-tumorigenic cell line, while T47D and MDA-MB-231 cell lines are derived from breast cancer patients. MDA-MB-231 has been shown to be estrogen receptor (ER)-negative, indicating a more aggressive form of breast cancer. Excitingly, our electrochemical results showed that the values of (k_{cat}/K_M)·[E_0] (= 1/τ) significantly increased in the cancer cell lysates. Comparison of the values of (k_{cat}/K_M)·[E_0]

of different breast cell lysates at concentration of 7.28 $\mu g \cdot mL^{-1}$ in bar graph is shown in Figure 5.5a. Triplicated experiments were carried out for each cell lysates. The statistical values of $(k_{cat}/K_M)\cdot[E_0]$ are (2.13 ± 0.73) x 10^{-3}, (3.62 ± 0.44) x 10^{-3}, (4.39 ± 0.34) x 10^{-3} and (5.61 ± 1.09) x 10^{-3} s^{-1} for HMEC, MCF-10A, T47D and MDA-MB-231 cell lysates, respectively. This trend is correlated well with our Western blot results (Figure 5.1b).

In order to estimate the overexpressed amount of cathepsin B in cancer cell lysates compared to the normal cells, an experiment was done by spiking certain amount of cathepsin B into HMEC lysate solution. According to Equation 4.6, the difference of cathepsin B in HMEC and MDA-MB-231 cell lysates at concentration of 7.28 $\mu g \cdot mL^{-1}$ can be derived as:

$$(k_{cat}/K_M)\cdot\Delta E_0 = 5.61 \text{ x } 10^{-3} - 2.13 \text{ x } 10^{-3} = 3.48 \text{ x } 10^{-3} \text{ s}^{-1}. \quad (5.3)$$

Assuming that k_{cat}/K_M equals to 7.22 x 10^4 $M^{-1}s^{-1}$ as obtained earlier, ΔE_0 equals to 48.2 nM. This implied that 7.28 $\mu g \cdot mL^{-1}$ HMEC spiked with 48.2 nM purified cathepsin B should be equivalent to 7.28 $\mu g \cdot mL^{-1}$ MDA-MB-231. The kinetic curves after spiking 48.2 nM purified cathepsin B into 7.28 $\mu g \cdot mL^{-1}$ HMEC solution indeed showed a decay time constant comparable to the same concentration of MDA-MB-231 cell lysate, as shown in Figure 5.5b. The statistic value of the decay time from three repeating measurements was (255 ± 30) s, giving a $(k_{cat}/K_M)\cdot[E_0]$ value of (3.97 ± 0.50) x 10^{-3} s^{-1} falling between (3.62 ± 0.44) x 10^{-3} s^{-1} for MCF-10A and (4.39 ± 0.34) x 10^{-3} s^{-1} for MDA-MB-231. The higher proteolysis rate of cancer cell lysate is indeed due to elevated cathepsin B activity.

Proteolysis by breast cell lysates has also been studied with a commercial fluorescence assay using 0.05 $mg \cdot mL^{-1}$ lysate of HMEC, MCF-10A, T47D and MDA-MB-231. Even though this method works well in measuring proteolysis of purified recombinant cathepsin B and was used as a validation technique in our previous studies,[1-2] the results were quite diverging and

unreliable in measuring cell lysates. Despite that the lysate concentration was about 10 times of that in electrochemical experiments, none of the kinetic curves except T47D lysate showed clear exponential increase in fluorescence intensity due to proteolytic cleavage of the AMC group from the peptide substrate. The fluorescence intensity was in general 10 to 100 times lower than the measurements using purified cathepsin B solutions at comparable or even lower concentrations. The measurements in MCF-10A and MDA-MB-231 cell lysates only showed noisy uncharacteristic fluctuations. None of these measurements were able to be used for quantitative analysis. It is noted that the fluorescence assay can only use a rather simple substrate Z-Leu-Arg-AMC where the signal moiety AMC has to be attached to the cleavage site Arg at the end of the peptide due to its fluorescence mechanism. The lack of specificity and strong interference likely limited this commercial fluorescence assay from measuring the proteolytic kinetics of the complex cell lysates. Further study for a better understanding of this phenomenon is still in progress.

5.6 Discussion

In this study, we have shown that cathepsin B exits as both pro and active forms in the whole cell extract of normal breast cells (HMEC), non-tumorigenic breast cells (MCF-10A) and breast cancer cells (T47D and MDA-MB-231). Our results also demonstrated that the total integrated pixel intensity from the Western blot bands, thus the amount of cathepsin B, increased for the cancer cell lysates. However, the commercial fluorescence assay is not suitable to study the proteolytic kinetics of the cathepsin B in the cell lysates. In contrast, electrochemical method applied on VACNF NEAs has shown great potential and advantage in quantitative study the complex cell lysates. We have shown that ACV measurements is a reliable tool to derive the value of $(k_{cat}/K_M)\cdot[E_0]$ from the cancer cell lysate solutions. The spiking experiments results

confirmed that the elevated proteolytic rate is due to the cathepsin B. Well-separated protruding VACNF tips immobilized with the peptide substrate likely facilitate the protease to reach and cleave the specific site of the peptides. The results from inhibitor experiment illustrated that proteases other than cathepsin B in the cancer cell lysate also contributed to the cleavage of the tetrapeptide substrate. We also found that the protease activity (i.e., the value of $(k_{cat}/K_M)\cdot[E_0]$) increased for the cancer cells, consistent with Western blot results. The value of $(k_{cat}/K_M)\cdot[E_0]$ is the highest for metastatic cancer cell MDA-MB-231, then followed by cancer cell T47D and non-tumorigenic cell MCF-10A. Normal cell lysate HMEC showed the smallest value of $(k_{cat}/K_M)\cdot[E_0]$, thus lowest protease activity. To our knowledge, this is the first report to use simple electrochemical method to quantify the protease activities in complex cell lysates and identify the cancer formation. Integrated in the multiplex system, this electrochemical biosensor can be potentially used for improving cancer diagnosis, treatment monitoring, and drug (inhibitor) screening.

Although this electrochemical technique is viable for detecting cathepsin B activity in tissue or cell lysates, it would have broader impact if it can profile protease in serum or urine samples. According to Karel Kotaska et al.'s bladder cancer study, the concentration of cathepsin B in serum is in the range of 27-126 $\mu g\cdot L^{-1}$ and that in urine is in the range of 0-2.54 $\mu g\cdot L^{-1}$.[163] The lowest concentration of purified cathepsin B by using ACV on VACNF NEA in our previous study is ~450 $\mu g\cdot L^{-1}$ (13.3 nM), about 4-20 times of the concentration of cathepsin B in serum and >200 times more in urine.[2] In order to effectively detect the cathepsin B in serum or urine samples, the detection limit of our electrochemical method needs to be further improved. One of the approaches is to use e-beam patterned VACNF NEAs which has exhibited enhanced performance in our previous study due to more uniform SiO_2 encapsulation and smaller

background from nonspecifically adsorbed Fc-peptide.[2] At the same time, the serum or urine samples can also be concentrated in order to effectively measure cathepsin B activity by using electrochemical method. It is noteworthy that cell culture (as used in this study) is the key to new drug discovery and screening analysis. Not only the 2D cell culture allows rapid and cost-effective approach, it also provides a simple and control environment to design a new technology. However, the 2D cell culture has its limitation due to the flat environment and lack of the complexity of cell network in biological system. In the previous study[2], we have demonstrated that this electrochemical technique also works nicely in the complex tissue lysates. The next logical step is to detect the level of cathepsin B activity in clinical tumor samples.

The absolute concentration [E_0] of cathepsin B also needs further study. From the difference in the proteolytic rates between the original WCE and 2IP MDA-MB-231 lysates, the concentration of removed cathepsin B was calculated to be ~38 nM according to Equation 5.2. The mass percentage of cathepsin B in MDA-MB-231 cell extract can be calculated as ~18% (1.3 $\mu g \cdot mL^{-1}$ cathepsin B in 7.28 $\mu g \cdot mL^{-1}$ total cell protein). However, according to the Western blot data (Table C.1) and the calibration curve (Figure C.2), the approximate percentage of cathepsin B in MDA-MB-231 is only ~0.13 %. Besides loss of the some cathepsin B during Western blot procedures, there are two other possibilities at this stage to explain such a large discrepancy. First, the k_{cat}/K_M value of the cathepsin B in the cell lysate may be much larger than that of the purified recombinant cathepsin B. Thus more recombinant cathepsin B was needed in the spiking experiments, leading to overestimation of cathepsin B quantities. The large variation in k_{cat}/K_M value of cathepsin B is quite common in literature. For example, it varies from ~2 x 10^3 $M^{-1}s^{-1}$ [150] to 7 x 10^6 $M^{-1}s^{-1}$ [181] depending on the source of cathepsin B and the nature of the peptide substrates. Second, the complex matrix of the cell lysate may have strong interference to

suppress the activity of the spiked recombinant cathepsin B, making its real k_{cat}/K_M value much lower than what we measured in simple buffer solutions in previous studies, thus more cathepsin B was needed to reach the same effects. This is consistent with the known network interaction with other enzymes in complex samples.

5.7 Conclusions

In summary, this work demonstrated two critical features toward rapid protease profiling using an electrochemical method based on nanoelectrode arrays fabricated with vertically aligned carbon nanofibers. First, continuously repeated ACV measurement of Fc-tetrapeptide attached to VACNF NEAs has been proved to be a reliable tool to measure the proteolytic kinetics and quantify the protease activity in complex breast cell lysates. Second, the activity of cathepsin B measured by this electrochemical method was found to increase from normal to cancer cell lysates. The clear inhibitor effects indicated that this method may be used as an effective technique for inhibitor screening in the complex biological samples. This study demonstrates the feasibility for future protease profiling using a library of peptide substrates specific to interested proteases on independently addressed NEAs. It could be potentially developed into a portable multiplex electronic system for cancer diagnosis, assessment of treatment efficacy, and drug screening.

Chapter 6 - Ultrasensitive blood-borne pathogen biosensor based on chemiluminescence (CL) method

Reproduced in part by permission of Royal Society of Chemistry.

Published as Syed, L. U.; Swisher, L. Z.; Huff, H.; Rochford, C.; Wang, C.; Liu, J.; Wu, J.; Richter, M.; Balivada, S.; Troyer, D.; Li, J. *Analyst* **2013**, *138*, 5600-5609.

6.1 Introduction

CL is a process in which visible light is emitted as a result of chemical reactions. CL is a much more sensitive and convenient analytical technique than commonly used FL methods due to high quantum yield, no need for exciting light sources, and low background.[182] It has been widely utilized for forensic investigations by spraying luminol (5-amino-2,3-dihydro-1,4-phthalazine-dione) and hydrogen peroxide at crime scene to identify dried blood stains.[183] Here, we report a study to improve luminol based CL by covalently attaching luminol molecules onto GNPs through a monolayer of carboxylic acid terminated alkane thiols. GNPs can serve as high-surface-area nanocarriers, making manipulation and binding of a large amount of luminol moieties easier. Detection of the CL signal generated by luminol on GNPs is expected to be much more sensitive than colorimetric measurements based on GNP aggregation that are used in many analytical applications.

GNPs have gained a considerable attention in the past few decades due to their unparalleled optical, electronic, physical, and chemical properties.[184-186] Ease of surface modification of GNPs with alkane thiol molecules and further covalent linking with other chemical and biological moieties make GNPs an attractive choice for sensor applications.[187-190] In addition, GNPs present strong size-dependent SPR, which significantly enhances the sensitivity of colorimetric or optical absorption detection of GNP based sensors.[88, 191-196] Here,

we demonstrate that GNPs can be used as convenient nanocarriers for luminol molecules, generating strong CL.

Luminol belongs to the family of heterocyclic hydrazide compounds, and is by far one of the most popular agents for CL applications.[196-199] Under the proper reaction conditions, luminol can generate strong blue-colored luminescence peaking at ~425 nm wavelength. The concept of light production by luminol catalyzed with Fe^{3+} ions released from red blood cells is the basis of forensic and hospital analysis of blood contamination.[183, 200-201] In many experiments to study luminol CL, ferricyanide ions $[Fe(CN)_6]^{3-}$ were used as the catalyst due to the higher chemical stability. When GNPs are involved, however, it is not conclusive how the GNPs affect the CL signal,[202-203] particularly since the SPR of GNPs strongly depends on their size and shape. Some studies using bare GNPs directly mixed with CL reagents reported that the CL signal was inhibited due to quenching by GNPs when their diameters were less than 5 nm, but was enhanced, possibly due to catalytic effects, when the GNP diameters were ~25 to 38 nm.[202-203] However, in another study using luminol molecules covalently attached to 30 nm-diameter GNPs, CL was found to be reduced by about five fold comparing to in bulk solutions.[204]

In general, electron transfer might facilitate catalytic effects to enhance CL while energy transfer to GNPs is sure to cause nonradiative deactivation (quenching) of chemically excited luminol products. The effect of GNPs to luminol CL was found to be minimal when the diameter was in the range of 5 to 10 nm.[202-203] To avoid the complication, we chose to use 10 nm-diameter GNPs in this study, where GNPs mainly serve as nano-carriers for manipulating and placing of large amount of luminol molecules in highly reduced volumes (or areas) by taking the advantage of the large surface-to-volume ratio of GNPs. In this study, the surface of GNPs is protected with a close-packed self-assembled monolayer of a long-chain thiol linker, mercaptoundecanoic acid

(MUA), to minimize both electron transfer and energy transfer between luminol and the GNP. This allowed us to assess the controversial results in previous studies[196, 202-204] on whether the surface-functionalized luminol can generate enhanced CL than in bulk solutions. Using this design, we have observed largely enhanced CL from luminol-labeled GNPs and have found that the CL intensity can be detected while the number of GNPs was varied by 8 orders of magnitude.

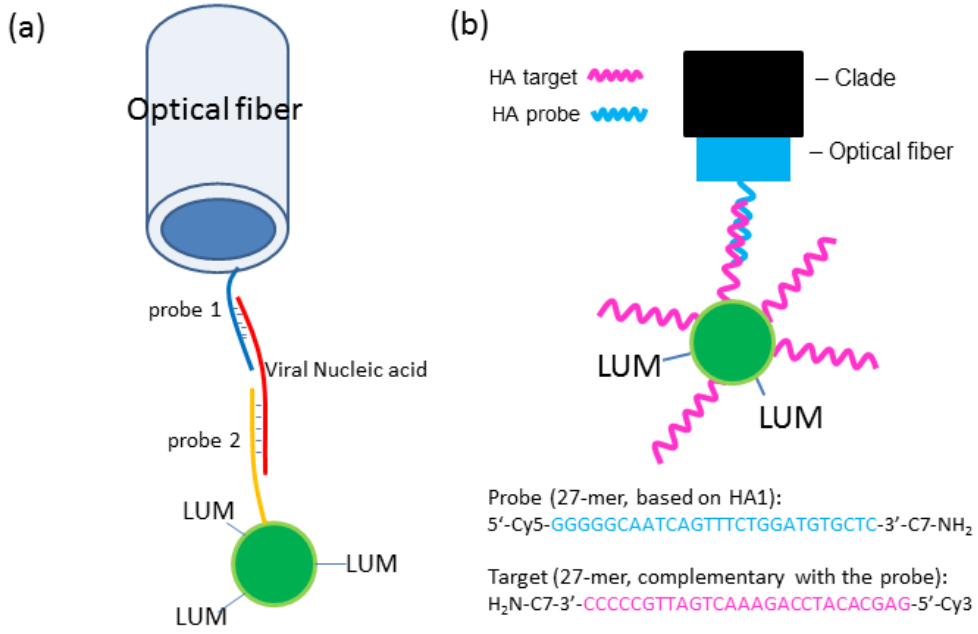

Figure 6.1 (a) Schematic illustration of viral nucleic acid biosensor based on CL detection by optical fibers. (b) Hybridization of HA target on the nanoparticles and HA probe on the optical fiber.

The study described here is aiming to design a new generation of chemiluminescent nanoparticle-based bio-detectors for blood-borne pathogens, such as H1N1. We expect to functionalize probe 1 on the optical fibers and after inserting the optical fibers into the fluids containing H1N1 viral nucleic acid (target), the probe 1 will hybridize with the target. Then, the hybridization of probe 2 with target will be performed. Probe 2 and luminol molecules are co-

immobilized on the surface of the carrier nanoparticles (Figure 6.1a). The concentration of the viral nucleic acid will be determined from the intensity of the chemiluminescence due to luminol molecules. The developed assay will be incorporated into a portable device for routine assays in hospitals or for large-scale screening of human populations to curb the rapid spread of the H1N1 virus and other viral or bacterial pathogens. In order to reach this goal, we start from preparing nanoparticles which are co-functionalized with both H1N1 nucleic acid fragment, such as influenza hemagglutinin sequence (HA target), and luminol and also functionalizing optical fibers with HA complimentary nucleic acid (HA probe) (Figure 6.1b). The hybridization of HA target and HA probe is investigated by fluorescence microscope and SEM. The CL performance using luminol-labeled latex beads (30 nm diameter) and luminol-labeled GNPs (10 nm diameter) are assessed and compared.

6.2 Experimental details

6.2.1 Materials and reagents

Citrate protected GNPs (8.0-12.0 nm in diameter) were purchased from Sigma Aldrich (Saint Louis, MO, USA) and BB International (UK). Carboxylate-modified latex beads in 30 nm diameter, mercaptoundecanoic acid (MUA), APTES and succinic anhydride were purchased from Sigma Aldrich (Saint Louis, MO, USA). Luminol (LUM), EDC, sulfo-NHS, Tween 20, potassium ferricyanide ($K_3Fe(CN)_6$), phosphate buffer saline (PBS), sodium hydroxide (NaOH), hydrogen peroxide (H_2O_2), dimethylformamide (DMF), ammonia hydroxide (NH_4OH) and microscope slides were obtained from Fisher Scientific (Pittsburgh, PA, USA). All chemicals used in this study were analytical grade. DI water with a resistivity of 18.2 MΩ-cm from a portable filtration system (Barnstead EASYpure II RF/UV, Model D7035, Thermo Scientific, Asheville, NC, USA) was used in all the experiments. 5'Cy5-

GGGGGCAATCAGTTTCTGGATGTGCTC-3'-C7-NH_2 (HA probe) and H_2N-C7-3'-CCCCCGTTAGTCAAAGACCTACACGAG-5'-Cy3 (HA target) were ordered from Eurofins Genomics (Huntsville, AL, USA). Polyethylene jacketed polymethyl-methacrylate (PMMA) optical fibers were purchased from Industrial Fiber Optics, Inc. (Tempe, AZ, USA).

6.2.2 Characterization of instruments

UV-visible absorption spectra were recorded using Beckman DU640 spectrophotometer in a 360 μL microcuvette with an optical path length of 10.0 mm. Infrared spectroscopy (IR) was performed on a Nicolet 380 FT-IR spectrophotometer with neat solid samples using an attenuated total reflectance (ATR) accessory. Fluorescence images of latex beads immobilized glass slide were taken by using an upright fluorescence optical microscope (Axioskop 2 FS plus; Carl Zeiss). The immobilization of latex beads on the optical fibers were investigated by using field-emission scanning electron microscopy (FESEM) (Leo 1550, Zeiss).

6.2.3 Modification of nanoparticles with luminol and/or viral nucleic acid

6.2.3.1 Modification of gold nanoparticles (GNPs) with luminol

The scheme to functionalize the GNPs with luminol is illustrated in Figure 6.2. The initial step was to exchange the citrate groups on the surface of GNPs with the MUA ligands under the protection of the nonionic surfactant Tween-20. Typically, 2 mL of citrate-protected GNP stock solution (5.99 x 10^{11} particles/mL) was transferred to a clean, dry test tube with a screw-cap followed by addition of 2 mL of 1X PBS with 0.2 mg/mL Tween-20 buffer (the same buffer composition was used for all following functionalization steps in this work). The mixed solution was incubated at room temperature for 30 min before 2 mL of 3.0 mM MUA solution (in 1:3 v/v ratio of ethanol/DI water mixture) was added. The solution was further incubated overnight at room temperature with gentle shaking. The mixture was centrifuged at 14,500 rpm (~14,100 G)

for 20 min to pellet the MUA-modified GNPs (GNP-MUA). The supernatant was discarded and the pellet was re-suspended in the buffer. The pellet was washed three times before being suspended in the buffer. MUA-modified GNPs (200 µL) then reacted with 100 µL of freshly prepared aqueous solution containing 50 mM EDC and 50 mM sulfo-NHS for 15 min. This mixture was then combined with 100 µL of 50 mM LUM solution (a few drops of 0.4 M NaOH were added to increase the solubility of LUM in DI water) and incubated at room temperature for 2 h. Finally, the LUM-modified GNPs (GNP-MUA-LUM) were washed 3 times with buffer and finally suspended in the buffer solution to obtain a final concentration of ~$1x10^{12}$ GNP/ml. The GNP concentrations before and after functionalization were calculated using the peak absorbance at 516 nm, in good agreement with the value for stock GNPs provided by the vendor. As shown in figure 6.2, by varying the concentration of luminol-labeled GNPs and fixing the concentration other CL reagents, the system can be developed into DNA biosensors through co-functionalization of target DNA and luminol on GNPs (scheme I). If varying the concentration of Fe^{3+}, the system can be developed into a biosensor to detect Fe^{3+}-carrying analytes such as red blood cells (scheme II). The study described here focuses on the application based on scheme I.

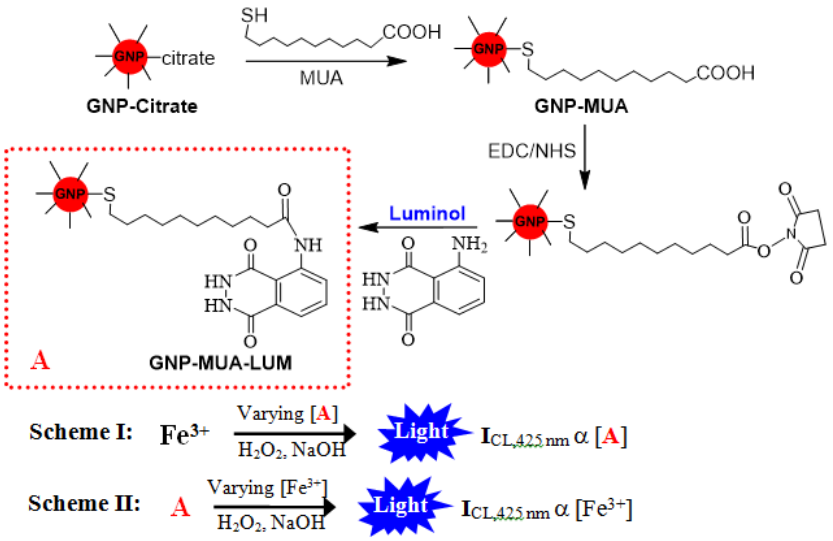

Figure 6.2 Schematic of the two-step covalent modification of GNPs with LUM by ligand exchange to replace citrate with MUA and amide linkage of the –COOH group in MUA with –NH_2 group in LUM. Two schemes to implement luminol-labeled GNPs (compound A) for chemical analyses are illustrated: Scheme I - to detect the amount of A by supplying sufficient Fe^{3+} catalyst and other reagents (H_2O_2 and NaOH); Scheme II - to detect Fe^{3+}-carrying analytes (such as red blood cells) which can catalyze the CL reaction in presence of sufficient amount of A and other reagents (H_2O_2 and NaOH).

6.2.3.2 Modification of latex beads with luminol and viral nucleic acid (Latex beads-HA probe/LUM)

Incubate 100 µL latex beads solution (4.75 x 10^{10}/mL) with 200 µL 4 mM EDC, sulfo-NHS and 100 µL 1 µM NH_2-(HA target)-Cy3 in 1 x PBS buffer at 37 °C for 2 hr; then add 100 µL 10 mM luminol and 100 µL 2 mM EDC, sulfo-NHS solution into above HA target functionalized latex beads solution (latex beads-HA target) and incubate at 37 °C for another 2 hr. Wash the HA target and luminol co-functionalized latex beads solution (latex beads-HA target/LUM) four times in 50 mM tris-HCl buffer by centrifuging at 14.1 x 1000 rcf speed for 1 hr each time. Re-suspend the latex beads-HA target/LUM pellet into 3 x SSC buffer after the last centrifuging.

6.2.4 Immobilization of latex beads on glass slide and PMMA optical fibers

The scheme to immobilize DNA probe on the glass surface was shown in figure 6.3. The glass slide was first treated by Piranha solution (concentrated H_2SO_4: 30% H_2O_2 = 3:1) for 20 min to generate hydroxyl groups on the surface, and then followed by DI H_2O and ethanol washing.[205] Dip the fiber in 1% NH_4OH solution at 80 °C for 1 hr to make the surface hydrophilic. Then, the fiber was emerged in 2% APTES ethanol solution for 2 hr in order to form

amine groups on the surface. The fiber was then kept in 1M succinic anhydride dissolved in dry DMF for overnight. The fiber was now terminated by –COOH and ready for DNA immobilization. Immerse –COOH terminated optical fiber tip in the solution of 5 – 20 μM HA probe with 10 mM EDC and sulfo-NHS in 1 x PBS buffer. Then, incubate the fiber with DNA solution in a humidity chamber at 37 °C for 2 hr. HA probe immobilized optical probe was then ready to hybridize with HA target-functionalized latex beads (latex beads-HA target/LUM). For immobilization of latex beads on the PMMA optical fiber, 3M H_2SO_4 solution or oxygen plasma etching can be used to generate –COOH groups on the surface.

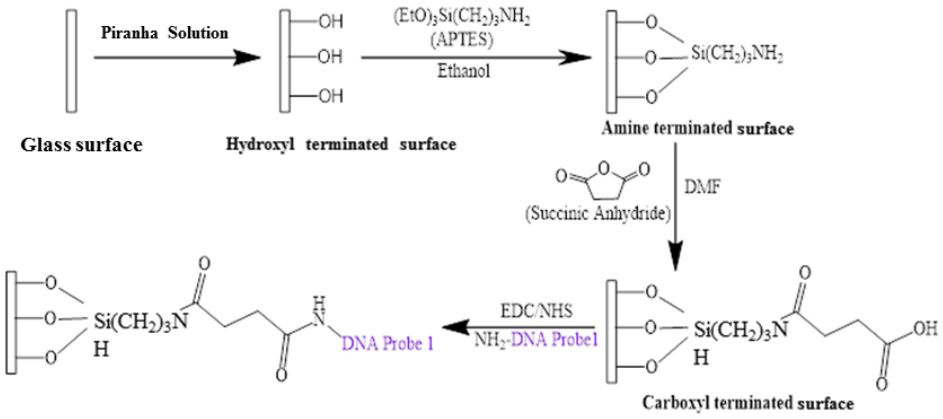

Figure 6.3 Schematic of the immobilization of DNA probe on the glass surface. (Provided by Lateef U. Syed)

Before immobilization of latex beads on the HA probe functionalized optical fiber or glass slide, blocking steps were followed in order to minimize the non-specific binding. Rinse the HA probe-functionalized optical fiber tip or glass slide by 1 x PBS buffer for three times, and then incubate the fiber in 5 mM ethanol amine solution with 10 mM EDC, sulfo-NHS at room temperature for 1 hr. Finally, incubate the optical fiber or glass slide with latex beads-HA target/LUM solution in 3 x SSC buffer in the humidity chamber at 37 °C for 2 hr. By this means,

the latex beads were immobilized on the glass slide or optical fiber tip surface through double strand DNA chain.

6.2.5 CL measurements using commercial luminometer in 96 well plate

CL experiments were carried out with a GloMax Multi+ system (Promega Corporation, CA, USA). The GloMax Multi+ system uses a photomultiplier tube (PMT) detector covering 350 to 650 nm for single-channel measurements of the kinetic CL emission from individual wells in a standard round bottom white polystyrene 96-well plate with a volume of ~300 μL per well (~6.5 mm in dia and ~11 mm in depth). A ~9.0 mm diameter optical mask was placed in front of the PMT detector assembly to cut off the background from other wells while allowing only the light from the selected well to be measured. In the experiments, 25 μL of 0.10 M NaOH, 25 μL of 1.41 M H_2O_2 and 25 μL of 1.0 mM $K_3Fe(CN)_6$ solution were preloaded in a well. Then 25 μL of luminol solution with varied concentration (~10^{-14} to 10^{-5} M) was added by a capillary injector at a rate of 200 μL/sec into the well to initialize the CL reaction. The CL signal was recorded continuously for ~8 min immediately following the injection.

6.3 Results and discussion

6.3.1 GNPs characterization

In regard of GNP characterization using TEM, UV-visible and FT-IR spectrum, please refer to Lateef U. Syed's dissertation 2012 and reference 3 for details. In short, strong absorption peaks were observed for all GNP samples at ~520 nm in the UV-visible absorption spectra. For the GNP-MUA-LUM, an additional small peak at 350 nm was observed, corresponding to the absorption peak of luminol. Clearly, the size of GNPs remained the same as they went through the ligand exchange and luminol functionalization processes.

For the GNP-MUA, the characteristic IR absorption peaks can be clearly seen at 2919 and 2849 cm^{-1}, which can be ascribed to the vibrational stretches of $–CH_2–$ functional groups in the MUA chain.[206] The peak corresponding to the C=O stretch in the terminal carboxylic acid group in GNP-MUA was shifted from ~1700 cm^{-1} to ~1550 to 1650 cm^{-1} indicating that the carboxylic acid group was in the ionized form as carboxylate salts.[207] This is consistent with the fact that the pH value of the suspension solution was ~7, above the pKa of the –COOH group. For the GNP-MUA-LUM, these IR bands split into three bands between ~1541 to 1730 cm^{-1}, consistent with the formation of amide bonds between the –COOH group in MUA and the $–NH_2$ group in luminol.[208] Also, a peak at 1396 cm^{-1} corresponding to the bending of C-H bond in the long alkane chain $–(CH_2)_n–$ can be seen in GNP-MUA and GNP-MUA-LUM. The peaks corresponding to the C-H stretch of the alkane chain were observed at 2919 and 2849 cm^{-1} for GNP-MUA and at 2913 and 2864 cm^{-1} for GNP-MUA-LUM, confirming that the MUA monolayer was intact after LUM functionalization. The N-H stretch mode of luminol, which is expected to be at 3,300 to 3,500 cm^{-1}, however, was buried under the strong and broad background absorption peak. The FTIR spectra clearly confirmed that the ligand exchange to replace citrate with MUA and functionalization of LUM to MUA were successful following the schemes shown in Figure 6.2.

6.3.2 Latex beads immobilization on glass slide and PMMA optical fibers

6.3.2.1 Investigation of immobilization using fluorescence microscope

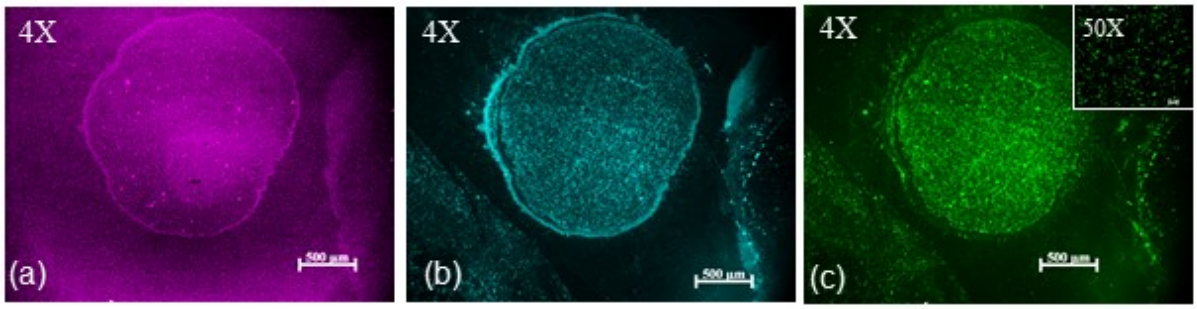

Figure 6.4 Fluorescence microscopy images of latex beads immobilized glass slide using (a) Cy5 filter with λ_{ex} = 625-655 nm, λ_{em} = 665-715 nm; (b) Cy3 filter with λ_{ex} = 540-552 nm, λ_{em} = 575-640 nm and (c) filter with λ_{ex} = 475-495 nm, λ_{em} = 515-565 nm in 4x magnification (Insert image: 50x magnification).

Fluorescence microscopy images of latex beads-immobilized glass slide through HA probe and HA target hybridization using different filters was shown in figure 6.4. Filter was chosen according to the excitation and emission wavelengths of Cy5 dye on HA probe, Cy3 dye on HA target and the dye molecules on latex beads. The excitation and emission wavelengths of all the dyes were summarized in table 6.1 (the values were provided by the vendor). Around 100 µL solution of 10 µM NH_2-(HA probe)-Cy3, EDC and sulfo-NHS mixture was spread on the surface of –COOH terminated glass slide and incubated in the humidity chamber at 37 °C for 2 hr. Thus, HA probe-Cy3 was immobilized on the glass slide through amide bond. Then, around 2 µL of latex beads-HA target/LUM solution (4.75 x 10^{10}/mL) was pinned on the surface of the HA probe-immobilized glass slide and kept in the humidity chamber at 37 °C overnight. After rinsing glass slide by 1 x PBS buffer and DI H_2O thoroughly, the area where the solution of latex beads-HA target/LUM was pinned on clearly showed fluorescence using different filters (figure 6.4). This result implied that latex beads were successfully immobilized on the glass slide surface through DNA hybridization.

Table 6.1 The excitation (λ_{ex}) and emission wavelength (λ_{em}) of different dye molecules.

Dye	λ_{ex} (nm)	λ_{em} (nm)
Cy5	650	670
Cy3	550	510
Dye on Latex beads	470	505

6.3.2.2 Investigation of immobilization using SEM

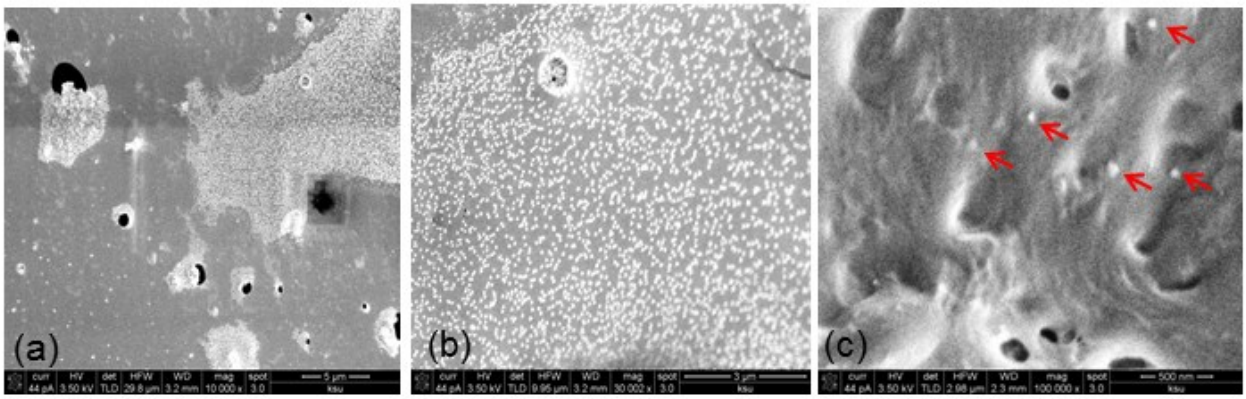

Figure 6.5 SEM images of latex beads immobilized on (a) & (b) side wall (clad) and (c) tip of the optical fiber core.

The optical fiber consisted of polyethylene black jacket, the clad which is made of fluorinated polymer and PMMA optical fiber core. The core diameter is 1.84 – 2.08 mm. The refractive index of core is 1.49. The immobilization of latex beads on the surface of PMMA optical fiber core was investigated by using SEM. Figure 6.5 (a) and (b) showed the clad of optical fiber core with latex beads attached. The pits on the clad surface might be due to the treatment using 3M H_2SO_4. In addition, the density of latex beads on the clad surface was varied greatly, which may be caused by non-uniformity of the hydroxyl functional groups generated by

the acid treatment (figure 6.5a). However, 30-nm-diameter latex beads are distributed on the clad surface without aggregation. Figure 6.5c shows the tip of optical fiber core functionalized with latex beads. The density of the latex beads on the core surface was extremely low compared to the clad area. Due to the photons traveling through the tip of the fiber core and blocked by the clad, the density of latex beads on the surface of optical fiber tip needs to be greatly improved.

6.3.3 CL assessment

The mechanism of light production by luminol has been extensively explored.[201, 209-211] The CL reaction of luminol generally utilizes Fe^{3+} as the catalyst and requires two equivalents of base to deprotonate the -NH-NH- group, leaving a negative charge that then undergoes resonance to form an enolate ion.[201] Then a cyclic addition reaction of the oxygen (provided by H_2O_2) at the two carbonyl carbons takes place (with Fe^{3+} catalyzing the breakdown of peroxide into oxygen and water), leading to the expulsion of N_2 in the gaseous form. This step leads to the formation of 3-aminophthalate (an excited form of luminol) and light emission peaking at a wavelength of 425 nm while electrons return to the ground state.[201, 211] In general, CL of luminol follows a flash mechanism in which CL occurs immediately and then decays at a time constant of tens of seconds.[211]

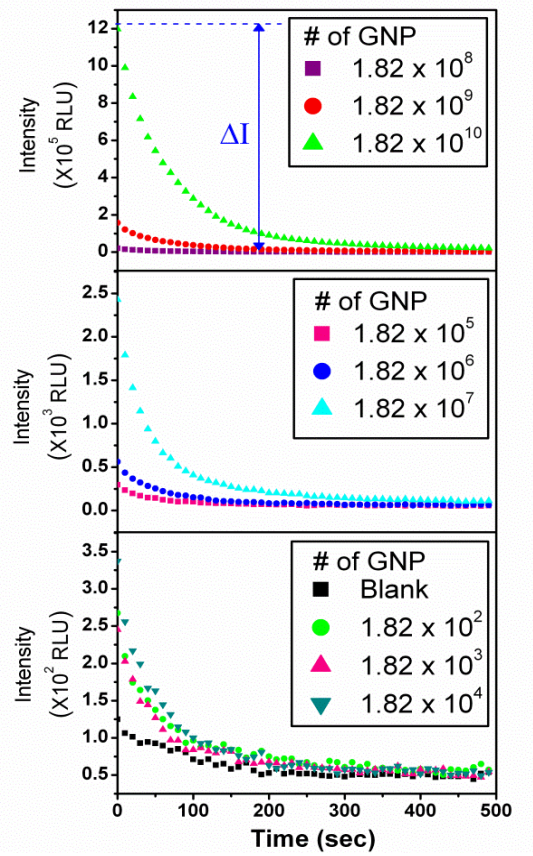

Figure 6.6 Chemiluminescence measurement of GNP-MUA-LUM solutions at a series of concentrations as it was diluted across 8 orders of magnitude. In these experiments, 25 µL of 0.10 M NaOH, 25 µL of 1.41 M H_2O_2 and 25 µL of GNP-MUA-LUM solution (containing varying number of GNPs from 1.82 x 10^{10} to 1.82 x 10^2) were added in a 96-well plate and loaded in the Promega GloMax-Multi+ microplate reader. Then 25 µL of 1.0 mM $K_3Fe(CN)_6$ solution was added into the mixture with a micro-injector to start the reaction and the chemiluminescence signal was recorded immediately.

Figure 6.6 shows the kinetic CL curves of GNP-MUA-LUM in a 96-well plate with the number of GNPs in the wells varied by 8 orders of magnitude from 1.82 x 10^{10} to 1.82 x 10^2 per well. The number of GNPs instead of GNP concentration was used for ease of comparison with

the data in later sections of this study, but can be easily converted to concentration since the total volume in these experiments was fixed at 100 μL in each well. The light intensity (in relative light units, RLU) clearly followed an exponential decay.

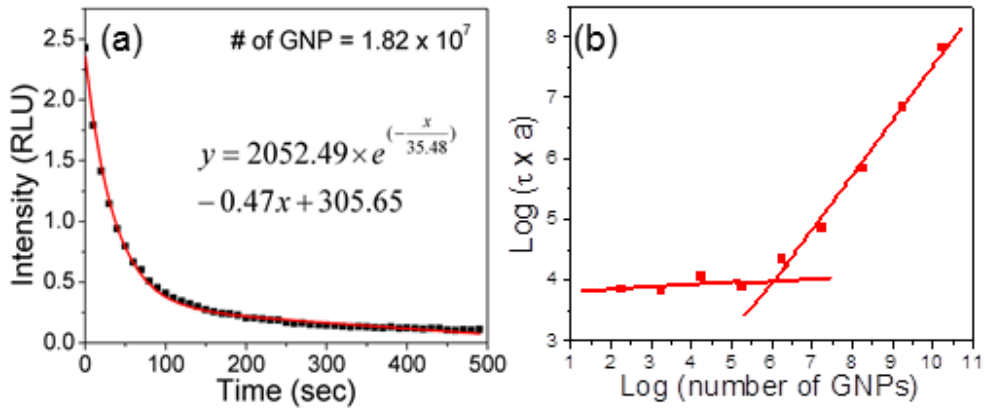

Figure 6.7 (a) The fitting of a representative kinetic chemiluminescence curve of GNP-MUA-LUM solutions recorded with GloMax Multi+ system. In this set of data, 1.82 x 10^7 GNP-MUA-LUM nanoparticles was used. The curve fits nicely with an exponential decay over a linear background. The decay time constant is 35 s. (b) The calibration curve using integrated CL signal (the initial intensity a multiplied by the decay time constant τ) instead of ΔI in the vertical axis. The slopes of the two linear curves are 0.90 (at high N) and 0.038 (at low N), nearly the same as those using ΔI.

Figure 6.7 shows a representative kinetic CL curve measured with 1.82 x 10^7 GNP-MUA-LUM nanoparticles, giving a decay time constant of about 35 s. At other concentrations, it varied between ~35 and ~61 s. For ease of comparison, the difference of CL signal (ΔI) between the first point and the last point on a CL kinetic curve (see Figure 6.6a) was used as the background-corrected CL signal.

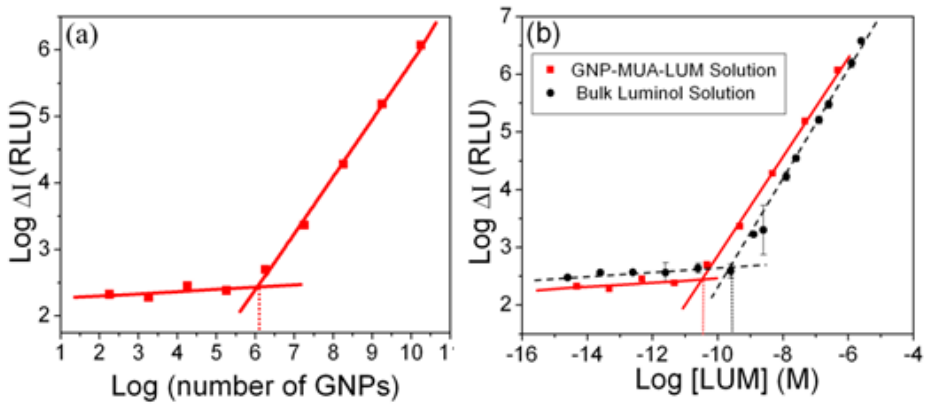

Figure 6.8 Calibration curves of the background-subtracted chemiluminescence signal ΔI (as shown in Figure 6.6). (a) Plot vs. the number of GNP-MUA-LUM nanoparticles in the 96-well plate, and (b) Plot vs. the equivalent luminol concentration from the GNP-MUA-LUM nanoparticles in the mixed solutions (red filled squares) in comparison with the bulk luminol concentration in the mixed solutions (black filled circles). The error bars of the data with bulk luminol are standard deviations calculated from three measurements at each condition.

Figure 6.8 summarizes the results from Figure 6.6 into calibration curves to illustrate CL for analytical applications under Scheme I. The CL signal can be observed clearly above that of the blank control sample as the quantity of the GNP-MUA-LUM was varied by 8 orders of magnitude, down to 1.82 x 10^2 nanoparticles. Interestingly, the value of ΔI vs. number of GNPs (N) showed two distinct linear curves on the log-log scale. They can be fitted with the following functions:

$$\log(\Delta I) = 0.86 \log N - 2.76, \quad \text{for N} \geq 1.82\text{x}10^{6}, \tag{6.1}$$

and $$\log(\Delta I) = 0.035 \log N + 2.23, \quad \text{for N} = 1.82\text{x}10^{2} \text{ to} 1.82\text{x}10^{5}. \tag{6.2}$$

At the low concentration limit, the slope is substantially less than 1 that is expected for a direct linear relationship. It is likely that the CL reaction was limited by slow diffusion or other

factors rather than by thermodynamic equilibrium. Nevertheless, the ΔI clearly increased with N. In the control experiments using deionized water to replace GNP solutions, the mean value of $\log(\Delta I_{blank})$ is 1.87 and the standard deviation $\sigma_{\log(\Delta I)}$ is 0.015. Accordingly, the signal detection limit is $\log(\Delta I)_{DL} = \log(\Delta I_{blank}) + 3\sigma_{\log(\Delta I)} = 1.92$. This means that even the lowest GNP-MUA-LUM concentration in Figure 6.6 (with $N = 1.82 \times 10^2$) is detectable in principle. However, the small slope makes the precise quantification at very low GNP-MUA-LUM concentrations difficult. Since our goal in this work is to develop a robust analytical technique, the cross point of the two linear curves in Figure 6.8a is defined as the detection limit instead, which gives 1.1×10^6 GNP-MUA-LUM nanoparticles per well (corresponding to 1.8×10^{-14} M GNP). The calibration curve using integrated CL intensities extracted by the curve fitting to the kinetic data (as shown in Figure 6.7b) showed nearly the same results.

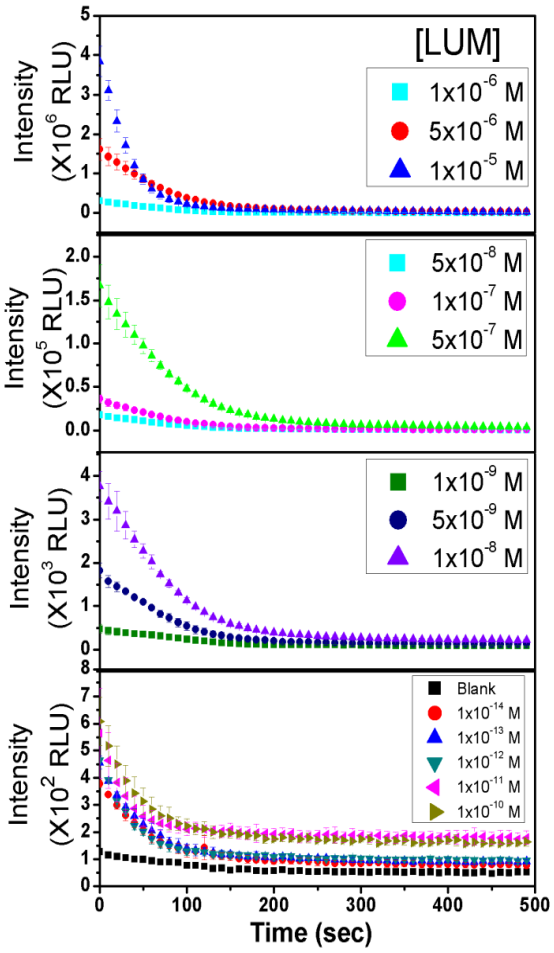

Figure 6.9 The kinetic CL measurements with bulk aqueous luminol solution at varied concentrations. The experimental conditions were identical with those in Figure 6.6 except the GNP-MUA-LUM solutions being replaced with bulk luminol solutions. About 25 µL of 0.10 M NaOH, 25 µL of 1.41 M H_2O_2 and 25 µL of 1.0 mM $K_3Fe(CN)_6$ solution were preloaded in a 96-well plate. Then 25 µL of aqueous luminol solution with varied concentration (1.0×10^{-14} to 1.0×10^{-5} M) was added by the micro-injector to initialize the CL reaction.

The bulk aqueous solution of free luminol (Figure 6.9) presented a similar CL behavior. The background-subtracted signal ΔI vs. the luminol concentration showed two straight lines very similar to that of GNP-MUA-LUM in Figure 6.8a. Assuming that luminol formed a close-

packed monolayer at a density of 5.0 x 10^{14} luminol/cm^2 on the outer surface (πd^2) of a GNP, it can be estimated that there is a maximum of 1,600 luminol molecules on each GNP. Thus the equivalent luminol concentration of various GNP-MUA-LUM solutions can be calculated and directly compared with free bulk luminol solutions, as shown in Figure 6.8b. The conversion into equivalent luminol concentration did not affect the slopes of GNP-MUA-LUM in the log-log scale. For the bulk luminol solutions, the slope at low concentration was 0.040, almost the same as 0.035 for GNP-MUA-LUM. But the slope at high concentrations became 1.00, indicating that the CL signal was ideally proportional to the bulk luminol concentration. At high concentrations, the value of ΔI for the GNP-MUA-LUM is notably higher than that of the bulk luminol solution at the same equivalent concentration. The higher CL signal, smaller slope, and lower background made the cross point for GNP-MUA-LUM appear at a lower concentration (~3.0 x 10^{-11} M equivalent luminol) than that of the bulk luminol solutions (3.9 x 10^{-10} M). Thus luminol-labeled GNPs provided a detection limit that was about one order of magnitude lower than in bulk solutions. Since it is unlikely that luminol can form a perfect close-packed monolayer on GNPs, the real detection limit could be even lower.

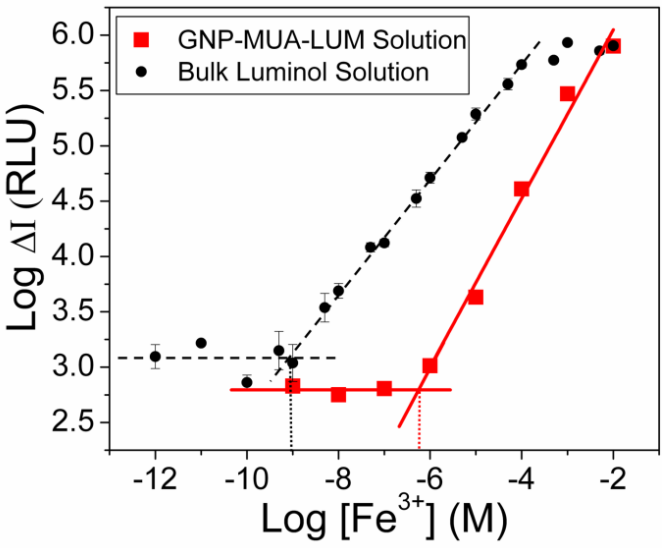

Figure 6.10 Calibration curves of the background-subtracted chemiluminescence signal vs. the concentration of $[Fe(CN)_6]^{3-}$ catalyst using luminol-attached GNPs (GNP-MUA-LUM) and bulk luminol solution, respectively. In the experiments with bulk luminol solutions, 25 μL of 0.10 M NaOH, 25 μL of 1.41 M H_2O_2, and 25 μL of $K_3Fe(CN)_6$ solution at varied concentrations were preloaded in a 96-well plate. Then 25 μL of luminol solution at 1.0 x 10^{-6} M concentration was added by a micro-injector into the above mixed solution to initialize the CL reaction. In the experiments with suspended GNP-MUA-LUM solutions, 25 μL of 0.10 M NaOH, 25 μL of 1.41 M H_2O_2 and 25 μL of GNP-MUA-LUM solution at 1.0 x 10^{11} GNP/mL concentrations (equivalent to 2.7 x 10^{-7} M luminol concentration) were preloaded in the wells of a 96 well plate. Then 25 μL of $K_3Fe(CN)_6$ solution at varied concentrations was added by the micro-injector into the well to start the CL reaction. The error bars of the data with bulk luminol solutions are standard deviations calculated from three measurements at each condition.

Some analytical applications may use Scheme II (see Figure 6.2) in which the catalyst concentration such as $[Fe^{3+}]$ is measured by supplying sufficient luminol and other reagents. The representative calibration curves in using 1.0 x 10^{-6} M bulk luminol and 1.0 x 10^{11} GNP-MUA-LUM nanoparticles/mL (equivalent to 2.7 x 10^{-7} M luminol) as the CL reagent are presented in Figure 6.10. In the CL measurements with bulk luminol solutions, a linear curve on the log-log scale was observed with a slope of 0.52 in the range of 1.0 x 10^{-9} M to 1.0 x 10^{-4} M $K_3Fe(CN)_6$. The detector was saturated at the $K_3Fe(CN)_6$ concentration above 1.0 x 10^{-4} M. Below 1.0 x 10^{-9} M $K_3Fe(CN)_6$, the ΔI signal was buried in the high and noisy background signal (about 3 – 5 times higher than in Figure 6.8). This was mostly due to trace $K_3Fe(CN)_6$ contaminations in the tubing and injector from previous experiments. Premixing $K_3Fe(CN)_6$ with NaOH and H_2O_2 solutions in the wells and adding the luminol solution through the micro-injector instead slightly

lowered the background, but it was still not possible to reach the extremely low background as in the case of luminol as the analyte.

A similar calibration curve of ΔI vs. the $K_3Fe(CN)_6$ concentration was obtained using the GNP-MUA-LUM solution (1.0 x 10^{11} nanoparticles/mL) and the result is summarized in Figure 6.10. The equivalent luminol concentration (2.7 x 10^{-7} M) was lower than the bulk luminol solution (1.0 x 10^{-6} M) and thus the detection saturation at high $K_3Fe(CN)_6$ concentrations was avoided. The background at low $K_3Fe(CN)_6$ concentrations was reduced by ~2 times. The slope of the linear curve at high $K_3Fe(CN)_6$ concentrations was increased from 0.52 (for the bulk luminol solution) to 0.76 (for the GNP-MUA-LUM solution). However, the linear range with the GNP-MUA-LUM solution was shifted to ~100 to 1,000 fold higher $K_3Fe(CN)_6$ concentrations comparing to the bulk luminol solution. The detection limit of $K_3Fe(CN)_6$ concentration (represented by the cross points) was 8.2 x 10^{-10} M for bulk luminol and 5.6 x 10^{-7} M for GNP-MUA-LUM, respectively. The reason for lower CL signal with GNP-MUA-LUM in Figure 6.10 may be due to two factors: (1) lower equivalent luminol concentration used in these experiments, and (2) the lower diffusion coefficient of GNPs than free luminol molecules causing lower CL reaction rate when the $K_3Fe(CN)_6$ concentration was low. However, since the slope with GNP-MUA-LUM is larger, it is expected that the CL signal in GNP-MUA-LUM could be higher, at least at the high $K_3Fe(CN)_6$ concentration limit, if a higher GNP-MUA-LUM concentration could be used. However, we found that increasing GNP-MUA-LUM concentration often induced GNP aggregation and precipitation to the bottom of the wells. These GNPs were out of the focal zone of the detector and thus caused the CL signal to decrease and unreliable.

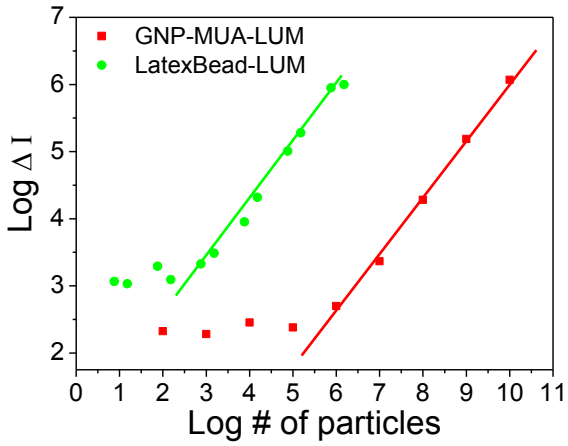

Figure 6.11 Log-log graph of ΔI vs. the number of particles. Red square: GNP-MUA-LUM. Green dot: luminol functionalized latex beads (Latex bead-LUM).

Comparison of the CL measurement using GNP-MUA-LUM and luminol functionalized latex beads (latex bead-LUM) was shown in Figure 6.11. It showed that chemiluminescence can detect down to ~1000 latex beads. Using the same amount of GNPs and latex beads, the chemiluminescence intensity by using latex beads is about 3 orders of magnitude larger than that by using GNPs. However, the surface area of 30-nm-diameter latex bead is only ~9 times larger than that of 10-nm-diameter GNP. The much larger signal might be due to latex bead's porous surface trapped large amount of luminol molecules.

6.4 Conclusions

In conclusion, we have demonstrated that the largely enhanced CL signal can be generated with luminol molecules covalently attached to 10-nm-diameter GNPs through an alkane thiol linker. This approach may be adopted for ultrasensitive analyses under two different schemes depending on whether luminol-labeled GNPs serve as a part of the analyte or as a reagent to generate CL for iron-containing catalysts as the analyte. The CL properties of luminol-

labeled GNPs have been systematically studied in suspended solutions in 96-well plates. The CL signal can be observed over 8 orders of magnitude variations in GNP concentration. The log-log calibration curves of suspended GNP-MUA-LUM showed two linear responses with distinct slopes. The portion with high slope can be used for reliable quantitative analysis and the portion with small slope may be used for ultrasensitive screening. It has been also found that using the same number of particles, luminol functionalized latex beads (30 nm diameter) showed about 3 orders of magnitude higher CL intensity compared to 10-nm-diameter luminol-labeled GNPs. Hybridization of HA target on the latex beads and HA probe on the glass slide or optical fiber surface has been successfully achieved. However, the density of latex beads on the optical fiber surface needs to be greatly improved in order to achieve ultrasensitive detection of viral nucleic acid. Finally, this assay will be incorporated into a simple hand-held device for routine assays in hospitals and clinics or for large-scale screening of human populations as diagnostic tools to identify specific viral strains.

Chapter 7 - Conclusions and Future Plan

In this dissertation, nanoelectrodes and nanoparticles have been used to develop biosensors for cancer-related proteases and viral nucleic acid detection, respectively. Our goal is to develop simple and portable devices for point-of-care detection of cancer and blood-borne pathogens. We hope that our results from these projects could pave the way of utilizing nanotechnology to achieve device miniaturization and multiplex detection.

7.1 Electrochemical protease biosensor based on enhanced AC voltammetry using CNF NEAs

In this study, continuously repeated ACV measurement of Fc-tetrapeptide attached to VACNF NEAs has been proved to be a reliable tool to measure the proteolytic kinetics and quantify the protease activity in both purified enzyme form and complex lysates environment. Significantly, the activity of cathepsin B measured by this electrochemical method was found to increase from normal to cancer cell lysates. In addition, the clear inhibitor effects indicated that this method may be used as an effective technique for inhibitor screening in the complex biological samples. This study demonstrates the feasibility for future protease profiling using a library of peptide substrates specific to interested proteases on independently addressed NEAs. It could be potentially developed into a portable multiplex electronic system for cancer diagnosis, assessment of treatment efficacy, and drug screening.

In the future, detection of cathepsin B activity can also be studied by using QCM and EIS. The results from above methods should be compared with those from ACV method in order to prove the validity of ACV method in the application of cathepsin B activity detection. In addition, quantifying the concentration of active cathepsin B in the cancer cell lysates by using ELISA method is also needed in the future to validate the results from ACV method. Moreover,

in the study of inhibitor GC-373 effect on cathepsin B activity, a complete IC_{50} curve can be generated by using EC method, which can help to demonstrate that this ACV method on VACNF NEAs is a suitable technique to develop inhibitor screening. Finally, by using e-beam patterned NEAs, a library of peptides can be immobilized on each independently address NEA to realize protease profiling.

7.2 Ultrasensitive blood-borne pathogen biosensor based on CL method

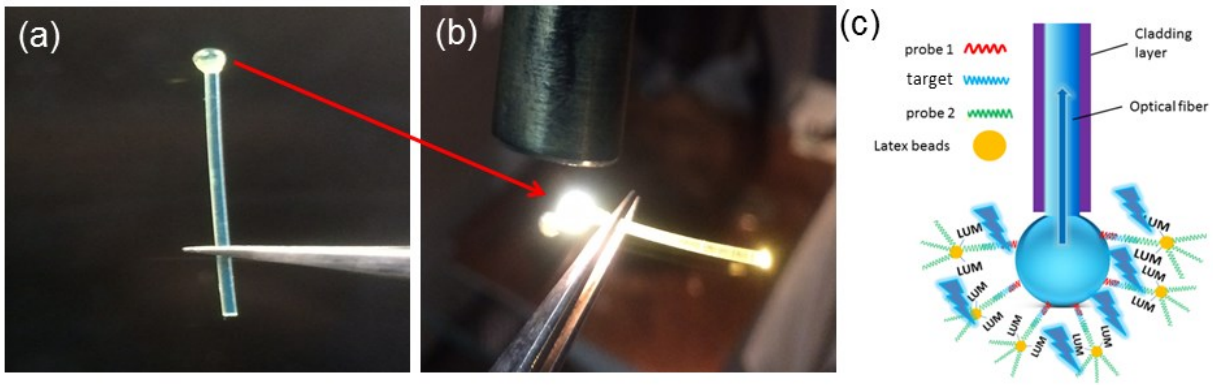

Figure 7.1 (a) Melted PMMA optical fiber tip formed a bulb. (b) The light enters the bulb and travels through the optical fiber. (c) Scheme of the portable chemiluminescence readout for detection of virus through nucleic acid hybridization on optical fibers.

We have demonstrated that the largely enhanced CL signal can be generated with luminol molecules covalently attached to 10-nm-diameter GNPs through an alkane thiol linker or luminol-labeled 30-nm-diameter latex beads. We found that using the same number of particles, luminol-labeled 30-nm-diameter latex beads showed even higher CL intensity compared to 10-nm-diameter luminol-labeled GNPs. Hybridization of HA target on the latex beads and HA probe on the glass slide or optical fiber surface has also been successfully achieved from the results of fluorescence optical microscope and SEM images.

However, the density of latex beads on the optical fiber surface through DNA hybridization needs to be greatly improved. This might be achieved by finding an appropriate etching method to generate uniform and abundant –OH groups on the surface of the optical fibers. By annealing the PMMA optical fiber tip into a sphere, the optical fiber can capture the photons from every direction (Figure 7.1a&b). Thus, the sensitivity can be further improved. In the future, we will be able to functionalize H1N1 viral nucleic acid probe 1 on the spherical tip of the optical fiber and after inserting the optical fibers into the fluids containing target viral nucleic acid, the probe 1 will hybridize with this target. Then, the hybridization of nucleic acid probe 2 with target will be performed. Probe 2 and luminol molecules are co-immobilized on the surface of the carrier nanoparticles (Figure 7.1c). The concentration of the viral nucleic acid will be determined from the intensity of the chemiluminescence due to luminol molecules. Assays will be incorporated into a simple hand-held device for routine assays in hospitals and clinics or for large-scale screening of human populations as diagnostic tools to identify specific viral strains.

References

1. Swisher, L. Z.; Syed, L. U.; Prior, A. M.; Madiyar, F. R.; Carlson, K. R.; Nguyen, T. A.; Hua, D. H.; Li, J., Electrochemical Protease Biosensor Based on Enhanced AC Voltammetry Using Carbon Nanofiber Nanoelectrode Arrays. *J. Phys. Chem. C* **2013,** *117* (8), 4268-4277.

2. Swisher, L. Z.; Prior, A. M.; Shishido, S.; Nguyen, T. A.; Hua, D. H.; Li, J., Quantitative Electrochemical Detection of Cathepsin B Activity in Complex Tissue Lysates Using Enhanced AC Voltammetry at Carbon Nanofiber Nanoelectrode Arrays. *Biosens. Bioelectron.* **2014,** *56*, 129-136.

3. Syed, L. U.; Swisher, L. Z.; Huff, H.; Rochford, C.; Wang, F.; Liu, J.; Wu, J.; Richter, M.; Balivada, S.; Troyer, D.; Li, J., Luminol-Labeled Gold Nanoparticles for Ultrasensitive Chemiluminescence-Based Chemical Analyses. *Analyst* **2013,** *138* (19), 5600-5609.

4. Vargas-Bernal, R.; Herrera-Pérez, G.; Rodríguez-Miranda, E., *Evolution and Expectations of Enzymatic Biosensors for Pesticides*. 2012.

5. Belkin, S., Microbial Whole-Cell Sensing Systems of Environmental Pollutants. *Curr. Opin. Microbiol.* **2003,** *6* (3), 206-212.

6. Su, L.; Jia, W.; Hou, C.; Lei, Y., Microbial Biosensors: A Review. *Biosens. Bioelectron.* **2011,** *26* (5), 1788-1799.

7. Wilson, G. S.; Gifford, R., Biosensors for Real-Time in vivo Measurements. *Biosens. Bioelectron.* **2005,** *20* (12), 2388-2403.

8. Zhao, Z.; Jiang, H., *Enzyme-Based Electrochemical Biosensors*. INTECH: Croatia, 2010.

9. Eggins, B. R., *Biosensors: an Introduction*. Wiley: 1996.

10. Hlavay, J.; Guilbault, G. G., Applications of the Piezoelectric Crystal Detector in Analytical Chemistry. *Anal. Chem.* **1977,** *49* (13), 1890-1898.

11. Fan, X.; White, I. M.; Shopova, S. I.; Zhu, H.; Suter, J. D.; Sun, Y., Sensitive Optical Biosensors for Unlabeled Targets: A Review. *Anal. Chim. Acta* **2008,** *620* (1–2), 8-26.

12. Yogeswaran, U.; Chen, S., A Review on the Electrochemical Sensors and Biosensors Composed of Nanowires as Sensing Material. *Sensors* **2008,** *8*, 290-313.

13. Yogeswaran, U.; Thiagarajan, S.; Chen, S., Nanocomposite of Functionalized Multiwall Carbon Nanotubes with Nafion, Nano Platinum, and Nano Gold Biosensing Film for Simultaneous Determination of Ascorbic Acid, Epinephrine, and Uric Acid. *Anal. Biochem.* **2007,** *365*, 122-131.

14. Koehne, J.; Chen, H.; Li, J.; Cassell, A. M.; Ye, Q.; Ng, H. T.; Han, J.; Meyyappan, M., Ultrasensitive Label-free DNA Analysis Using an Electronic Chip Based on Carbon Nanotube Nanoelectrode Arrays. *Nanotechnology* **2003,** *14*, 1239.

15. Koehne, J. E.; Chen, H.; Cassell, A. M.; Ye, Q.; Han, J.; Meyyappan, M.; Li, J., Miniaturized Multiplex Label-Free Electronic Chip for Rapid Nucleic Acid Analysis Based on Carbon Nanotube Nanoelectrode Arrays. *Clin. Chem.* **2004,** *50*, 1886-1893.

16. Cui, D.; Tian, F.; Coyer, S. R.; Wang, J.; Pan, B.; Gao, F.; .He, R.; Zhang, Y., Effects of Antisensemyc-Conjugated Single-Walled Carbon Nanotubes on HL-60 Cells. *Nanosci. Nanotechnol.* **2007,** *7*, 1639-1646.

17. Besteman, K.; Lee, J.-O.; Wiertz, F. G. M.; Heering, H. A.; Dekker, C., Enzyme-Coated Carbon Nanotubes as Single-Molecules Biosensors. *Nano Lett.* **2003,** *3*, 727-730.

18. Chen, R. J.; Bangsaruntip, S.; Drouvalakis, K. A.; Kam, N. W. S.; Shim, M.; Li, Y.; Kim, W.; Utz, P. J.; Dai, H., Noncovalent Funtionalization of Carbon Nanotubes for Highly Specific Electronic Biosensors. *PNAS* **2003,** *100*, 4984-4989.

19. Pan, B.; Cui, D.; Xu, P.; Li, Q.; Huang, T.; He, R.; Gao, F., Study on Interaction between Gold Nanorod and Bovine Serum Albumin. *Colloids Surf., A* **2007,** *295*, 217-222.

20. Liu, J.; Lu, Y., A Colorimetric Lead Biosensor Using DNAzyme-Directed Assembly of Gold Nanoparticles. *J. Am. Chem. Soc.* **2003,** *125*, 6642-6643.

21. Pan, B.; Cui, D.; Sheng, Y.; Ozkan, C.; Gao, F.; He, R.; Li, Q.; Xu, P.; Huang, T., Dendrimer-Modified Magnetic Nanoparticles Enhance Efficiency of Gene Delivery System. *Cancer Res.* **2007,** *67*, 8156-8163.

22. Hansen, J. A.; Wang, J.; Kawde, A.-N.; Xiang, Y.; Gothelf, K. V.; Collins, G., Quantum-Dot/Aptamer-Based Ultrasensitive Multi-Analyte Electrochemical Biosensor. *J. Am. Chem. Soc.* **2006,** *128*, 2228-2229.

23. Li, Z.; Wang, Y.; Wang, J.; Tang, Z.; Pounds, J. G.; Lin, Y., Rapid and Sensitive Detection of Protein Biomarker Using a Portable Fluorescence Biosensor Based on Quantum Dots and a Lateral Flow Test Strip. *Anal .Chem.* **2010,** *82*, 7008-7014.

24. Ferlay, J.; Ervik, M.; Dikshit, R.; Eser, S.; Mathers, C.; Rebelo, M. GLOBOCAN 2012 v1.0, Cancer Incidence and Mortality Worldwide: IARC Cancer Base No. 11. http://globocan.irac.fr.

25. Cancer facts and figures 2014. American Cancer Society: Atlanta, 2014.

26. Yuan, J.; Duan, R.; Yang, H.; Luo, X.; Xi, M., Detection of Serum Human Epididymis Secretory Protein 4 in Patients with Ovarian Cancer Using a Label-Free Biosensor Based on Localized Surface Plasmon Resonance. *Int. J. Nanomedicine* **2012,** *7*, 2921-2928.

27. Jin, B.; Wang, P.; Mao, H.; Hu, B.; Zhang, H.; Cheng, Z.; Wu, Z.; Bian, X.; Jia, C.; Jing, F.; Jin, Q.; Zhao, J., Multi-Nanomaterial Electrochemical Biosensor Based on Label-Free Graphene for Detecting Cancer Biomarkers. *Biosens. Bioelectron.* **2014,** *55* (0), 464-469.

28. Understanding HIV/AIDS- the Basics. http://www.webmd.com/hiv-aids/guide/understanding-aids-hiv-basics#1.

29. Hepatitis C. http://www.who.int/mediacentre/factsheets/fs164/en/.

30. Louie, B.; Lei, J.; Liska, S.; Dowling, T.; Pandori, M. W., Assessment of Sensitivity and Specificity of First, Second, and Third Generation EIA for the Detection of Antibodies to HIV-1 in Oral Fluid. *J. Virol. Method* **2009,** *159* (1), 119-121.

31. Mattke, P.; Kramer, S.; GershyDamet, G. M.; Rehle, T. M.; Liomba, G. N.; Krämer, S.; Gershy Damet, G. M.; Konan, K.; Sangare, A.; Zekeng, L.; Tsague, J. M.; Kaptue, L.; Eberle, J.; Gürtler, L., Evaluation of a Quantitative Double ELISA Strategy for Confirmation and Differentiation of HIV Infection. *J. Virol. Methods* **1997,** *66* (2), 203-209.

32. Eriksson, L. E.; Leitner, T.; Wahren, B.; BostrÖM, A.-C.; Falk, K. I., A Multiplex Real-time PCR for Quantification of HIV-1 DNA and the Human Albumin Gene in CD4+ Cells. *APMIS* **2003,** *111* (6), 625-633.

33. Cao, Y.; Jin, R.; Mirkin, C. A., Nanoparticles with Raman Spectroscopic Fingerprints for DNA and RNA Detection. *Science* **2002,** *297*, 1536-1540.

34. Li, Y.; Xiang, J.; Zhou, F., Sensitive and Label-Free Detection of DNA by Surface Plasmon Resonance. *Plasmonics* **2007,** *2*, 79-87.

35. Guo, Y.; Chen, J.; Chen, G., A Label-Free Electrochemical Biosensor for Detection of HIV Related Gene Based on Interaction between DNA and Protein. *Sensor. Actuat. B-Chem.* **2013,** *184* (0), 113-117.

36. Zhang, X.; Guo, Q.; Cui, D., Recent Advances in Nanotechnology Applied to Biosensors. *Sensors* **2009,** *9*, 1033-1053.

37. Huang, X.; El-Sayed, M. A., Gold Nanoparticles: Optical Properties and Implementations in Cancer Diagnosis and Photothermal Therapy. *J. Adv. Res.* **2010,** *1* (1), 13-28.

38. Homola, J., Surface Plasmon Resonance Sensors for Detection of Chemical and Biological Species. *Chem. Rev.* **2008,** *108* (2), 462-493.

39. Springer, T.; Ermini, M. L.; Spackova, B.; Jablonku, J.; Homola, J., Enhancing Sensitivity of Surface Plasmon Resonance Biosensors by Functionalized Gold Nanoparticles: Size Matters. *Anal. Chem.* **2014,** *86*, 10350-10356.

40. Liang, K.; Qi, J.; Mu, W.; Chen, Z., Biomolecules/Gold Nanowires-Doped Sol-Gel film for Label-Free Electrochemical Immunoassay of Testosterone. *J. Biochem. Biophys. Meth.* **2008,** *70*, 1156-1162.

41. Peng, Y.; Liu, H., Effects of Oxidation by Hydrogen Peroxide on the Structures of Multiwalled Carbon Nanotubes. *Ind. Eng. Chem. Res.* **2006,** *45* (19), 6483-6488.

42. Musameh, M.; Wang, J.; Merkoci, A.; Lin, Y., Low-Potential Stable NADH Detection at Carbon Nanotube-Modified Glassy Carbon Electrodes. *Electrochem. Commun.* **2002,** *4*, 743-746.

43. Wang, J.; Musameh, M., Carbon Nanotube/Teflon Composite Electrochemical Sensors and Biosensors. *J. Am. Chem. Soc.* **2003,** *125*, 2408-2409.

44. Wang, J.; Li, M.; Shi, Z.; Li, N.; Gu, Z., Direct Electrochemistry of Cytochrome C at a Glassy Carbon Electrode Modified with Single-Wall Carbon Nanotubes. *Anal .Chem.* **2002,** *74*, 1993-1997.

45. Wang, Z.; Liu, J.; Liang, Y.; Wang, Y.; Luo, G., Carbon Nanotube-Modified Electrodes for the Simultaneous Determination of Dopamine and Ascorbic Acid. *Analyst* **2002,** *127*, 653-658.

46. Nguyen-Vu, T. D. B.; Chen, H.; Cassell, A. M.; Andrews, R.; Meyyappan, M.; Li, J., Vertically Aligned Carbon Nanofiber Arrays: An Advance toward Electrical-Neural Interfaces. *Small* **2006,** *2*, 89-94.

47. Syed, L. U.; Liu, J.; Prior, A. M.; Hua, D. H.; Li, J., Enhanced Electron Transfer Rates by AC Voltammetry for Ferrocenes Attached to the End of Embedded Carbon Nanofiber Nanoelectrode Arrays. *Electroanalysis* **2011,** *23* (7), 1709-1717.

48. Carmeliet, P., Angiogenesis in Health and Disease. *Nat. Med.* **2003,** *9* (6), 653-660.

49. Koblinski, J. E.; Ahram, M.; Sloane, B. F., Unraveling the Role of Proteases in Cancer. *Clin. Chim. Acta* **2000,** *291* (2), 113-135.

50. Puente, X. S.; Sanchez, L. M.; Overall, C. M.; Lopez-Otin, C., Human and Mouse Proteases: a Comparative Genomic Approach. *Nat. Rev. Genet.* **2003,** *4* (7), 544-558.

51. Rakashanda, S.; Rana, F.; Rafiq, S.; Masood, A.; Amin, S., Role of Proteases in Cancer: A Review. *Biotech. Mol. Bio. Rev.* **2012,** *7* (4), 90-101.

52. Koontongkaew, S., The Tumor Microenvironment Contribution to Development, Growth, Invasion and Metastasis of Head and Neck Squamous Cell Carbinomas. *J. Cancer* **2013,** *4* (1), 66-83.

53. Zucker, S.; Cao, J.; Chen, W., Critical Appraisal of the Use of Matrix Metalloproteinase Inhibitors in Cancer Treatment. *Oncogene* **2000,** *19* (56), 6642-6650.

54. Poole, A. R.; Tiltman, K. J.; Recklies, A. D.; Stoker, T., Difference in Secretion of the proteinase Cathepsin B at the Edges of Human Breast Carcinomas and Fibroadenomas. *Nature* **1978,** *273*, 545-547.

55. Campo, E.; Munoz, J.; Miquel, R., Cathepsin B Expression in Colorectal Carcinomas Correlates with Tumor Progression and Shortened Patient survival. *Am. J. Pathol.* **1994,** *145*, 301-309.

56. Watanabe, M.; Higashi, T.; Watanabe, A.; Osawa, T.; Sato, Y.; Kimura, Y.; Tominaga, S.; Hashimoto, N.; Yoshida, Y.; Morimoto, S.; Shito, S.; Hasinoto, M.; Kobayashi, M.; Tomoda, J.; Tsuji, T., Cathepsin B and L Activities in Gastric Cancer Tissue: Correlation with Histological Findings. . *Biochem. Med. Metab. Biol.* **1989,** *42*, 21-29.

57. Sukoh, N.; Abe, S.; Ogura, S., Immunohistochemical Study of Cathepsin B. Prognostic Significance in Human Lung Cancer. *Cancer* **1994,** *74*, 46-51.

58. Sinha, A.; Wilson, J.; Gleason, D.; Reddy, P.; Sameni, M.; Sloane, B., Immunohistochemical Localization of Cathepsin B in Neoplastic Human Prostate. *Prostate* **1995,** *26*, 171-178.

59. Saleem, M.; Vaqar, M.; Weixiong, Z., A Novel Biomarker for Staging Human Prostate Adenocarcinoma: Overexpression of Matriptase with Concomitant Loss of its Inhibitor, Hepatocyte Growth Factor Activitor Inhibitor-1. *Cancer Epidemiol. Biomarkers. Prev.* **2006,** *15*, 217-227.

60. Yamamoto, H.; Ikv, S.; Adachi, Y.; Imsumran, A.; Taniguchi, H.; Nosho, K.; Min, Y.; Horiuchi, S.; Yoshida, M.; Itoh, F.; Imai, K., Association of Trypsin Expression with Tumor Progression and Matrilysin Expression in Human Colorectal Cancer. *J. Pathol.* **2003,** *199*, 176-184.

61. Truong, K.; Ikura, M., The Use of FRET Imaging Microscopy to Detect Protein-Protein Interactions and Protein Conformational Changes *in vivo*. *Curr.Opin. Struct. Bio.* **2001,** *11*, 573-578.

62. Kim, G. B.; Kim, Y.-P., Analysis of Protease Activity Using Quantum Dots and Resonance Energy Transfer. *Theranostics* **2012,** *2* (2), 127-138.

63. Mahmoud, K. A.; Hrapovic, S.; Luong, J. H. T., Picomolar Detection of Protease Using Peptide/Single Walled Carbon Nanotube/Gold Nanoparticle-Modified Electrode. *ACS Nano* **2008,** *2*, 1051-1057.

64. Adjémian, J.; Anne, A.; Cauet, G.; Demaille, C., Cleavage-Sensing Redox Peptide Monolayers for the Rapid Measurement of the Proteolytic Activity of Trypsin and α-Thrombin Enzymes. *Langmuir* **2010,** *26* (12), 10347-10356.

65. Mahmoud, K. A.; Luong, J. H. T., Impedance Method for Detecting HIV-1 Protease and Screening for Its Inhibitors Using Ferrocene-Peptide Conjugate/Au Nanoparticle/Single-Walled Carbon Nanotube Modified Electrode. *Anal .Chem.* **2008,** *80*, 7056-7062.

66. Park, K.; Ahn, J.; Yi, S. Y.; Kim, M.; Chung, B. H., SPR Imaging-Based Monitoring of Caspase-3 Activation. *Biochem. Biophys. Res. Comm.* **2008,** *368* (3), 684-689.

67. Burokerkilgore, M.; Wang, K. K. W., A Coomassie Brilliant Blue G-250-Based Colorimetric Assay for Measuring Activity of Calpain and Other Proteases. *Anal. Biochem.* **1993,** *208* (2), 387-392.

68. Ebinuma, H.; Miyazaki, O.; Yago, H.; Hara, K.; Yamauchi, T.; Kadowaki, T., A Novel ELISA System for Selective Measurement of Human Adiponectin Multimers by Using Proteases. *Clin. Chim. Acta* **2006,** *372* (1–2), 47-53.

69. Cenac, N.; Andrews, C. N.; Holzhausen, M.; Chapman, K.; Cottrell, G.; Andrade-Gordon, P.; Steinhoff, M.; Barbara, G.; Beck, P.; Bunnett, N. W.; Sharkey, K. A.; Ferraz, J. G. P.; Shaffer, E.; Vergnolle, N., Role for Protease Activity in Visceral Pain in Irritable Bowel Syndrome. *J. Clin. Invest.* **2007,** *117* (3), 636-647.

70. Guan, Y.; Wang, J.; Sun, J., A Method for Determination of Hexokinase Activity by RP-HPLC. *Wuhan U of J of Nat. Sci.* **2011,** *16*, 535-540.

71. Schilling, O.; Overall, C., Proteome-Derived, Database-Searchable Peptide Libraries for Identifying Protease Cleavage Sites. *Nat. Biotechnol.* **2008,** *26*, 685-694.

72. Thomas, D.; Francis, P.; Smith, C.; Ratcliffe, S.; Ede, N.; Kay, C., A Broad-Spectrum Fluorescence-Based Peptide Librara for the Rapid Identification of Protease Substrate. . *Proteomics* **2006,** *6*, 2006.

73. Nagai, T.; Miyawaki, A., A High-Throughput Method for Development of FRET-Based Indicators for Proteolysis. *Biochem. Bioph. Res. Co.* **2004,** *319*, 72-77.

74. Mahajan, N.; Harrison-Shostak, D.; Michaux, J.; Herman, B., Novel Mutant Green Fluorescent Protein Protease Substrates Reveal the Activation of Specific Caspases during Apoptosis. *Chem. Biol.* **1999,** *6*, 401-409.

75. Hulkower, K.; Butler, C. C.; Linebaugh, B. E.; Klaus, J. L.; Keppler, D.; Giranda, V. L.; Sloane, B. F., Fluorescent Microplate Assay for Cancer Cell-Associated Cathepsin B. *Eur. J. Biochem.* **2000,** *267*, 4165-4170.

76. Helms, V., *Fluorescence Resonance Energy Transfer*. Wiley-VCH: Weinheim, 2008.

77. Harris, D., *Applications of Spectrophotometry*. 8th ed.; W. H. Freeman and Co.: New York, 2010.

78. Hawrylak, P.; Narvaez, G.; Bayer, M.; Forchel, A., Excitonic Absorption in a Quantum Dot. *Phys. Rev. Lett.* **2000,** *85*, 389-392.

79. Moreels, I.; Hens, Z., On the Interpretation of Colloidal Quantum-Dot Absorption Spectra. *Small* **2008,** *4*, 1866-1868.

80. Gao, X.; Cui, Y.; Levenson, R.; Chung, L.; Nie, S., In Vivo Cancer Targeting and Imaging with Semiconductor Quantum Dots. *Nat. Biotechnol.* **2004,** *22*, 969-976.

81. chan, W.; Maxwell, D.; Gao, X.; Bailey, R.; Han, M.; Nie, S., Luminescent Quantum Dots for Multiplexing Biological Detection and Imaging. *Curr. Opin. Biotech.* **2002,** *13*, 40-46.

82. Wu, X.; Liu, H.; Liu, J.; Haley, K.; Treadway, J.; Larson, J., Immunofluorescent Labeling of Carcer Marker Her2 and Other Cellular Targets with Semiconductor Quantum Dots. *Nat. Biotechnol.* **2002,** *21*, 41-46.

83. M. Bruchez, J.; Moronne, M.; Gin, P.; Weiss, S.; Alivisatos, A., Semiconductor Nanocrystals as Fluorescent Biological Labels. *Science* **1998,** *281*, 2013-2016.

84. Hines, M.; Guyot-Sionnest, P., Synthesis and Characterization of Strongly Luminescing ZnS-Capped CdSe Nanocrystals. *J. Phys. Chem.* **1996,** *100*, 468-471.

85. Shi, L.; Paoli, V. D.; Rosenzweig, N.; Rosenzweig, Z., Synthesis and Application of Quantum Dots FRET-Based Protease Sensors. *J. Am. Chem. Soc.* **2006,** *128*, 10378-10379.

86. Rosenzweig, Z.; Shi, L.; Rosenzweig, N., Luminescent Quantum Dots Fluorescence Resonance Energy Transfer-Based Probes for Enzymatic Activity and Enzyme Inhibitors. *Anal .Chem.* **2007,** *79*, 208-214.

87. Gan, S. D.; Patel, K. R., Enzyme Immunoassay and Enzyme-Linked Immunosorbent Assay. *J. Invest. Dermatol.* **2013,** *133* (9), e12.

88. Baptista, P.; Pereira, E.; Eaton, P.; Doria, G.; Miranda, A.; Gomes, I.; Quaresma, P.; Franco, R., Gold Nanoparticles for the Development of Clinical Diagnosis Methods. *Anal. Bioanal. Chem.* **2008,** *391* (3), 943-950.

89. Sanger, F.; Coulson, A. R., A Rapid Method for Determining Sequences in DNA by Primed Synthesis with DNA Polymerase. *J. Molec. Biol.* **1975,** *94*, 441-448.

90. Sanger, F.; Nicklen, S.; Coulson, A. R., DNA Sequencing with Chain-Terminating Inhibitors. *Proc. Natn. Aced. Sci. USA* **1977,** *74*, 5463-5467.

91. Maxam, A. M.; Gilbert, W., A New Method for Sequencing DNA. *Proc. Natn. Aced. Sci. USA* **1977,** *74*, 560-564.

92. Maxam, A. M.; Gilbert, W., Sequencing endlabled DNA with Base-Specific Chemical Cleavages. *Meth. Enzym.* **1980,** *65*, 499-560.

93. Nyren, P.; Lundin, A., Enzymatic Method for Continuos Monitoring of Inorganic Pyrophosphate Synthesis. *Anal. Biochem.* **1985,** *151*, 504-509.

94. Hyman, E. D., A New Method of Sequencing DNA. *Analyt. Biochem.* **1988,** *174*, 423-436.

95. Ronaghi, M.; Karamohamed, S.; Pettersson, B.; Uhlen, M.; Nyren, P., Real-Time DNA Sequencing Using Detection of Pyrophosphate Release. *Anal. Biochem.* **1996,** *242*, 84-89.

96. Shera, E. B.; Seitzinger, N. K.; Davis, L. M.; Keller, R. A.; Soper, S. A., Detection of Single Fluorescent Molecules. *Chem. Phys. Lett.* **1990,** *174*, 553-557.

97. Harding, J. D.; Keller, R. A., Single-Molecule Detection as an Approach to Rapid DNA Sequencing. *Trends Biotechnol.* **1992,** *10*, 55-57.

98. Mackay, I. M., Real-Time PCR in the Microbiology Laboratory. *Clin. Microbiol. Infect.* **2004,** *10*, 190-212.

99. Mikkelsen, S. R., Electrochemical Biosensors for DNA Sequence Detection. *Electroanalysis* **1996,** *8* (1), 15-19.

100. Palek, E.; Fojta, M., Electrochemists are Developing Fast and Easy Methods for Determining Nucleic Acid Sequences and DNA Damage. *Anal .Chem.* **2001,** *73* (3), 74A-83A.

101. Wang, J., Electrochemical Nucleic Acid Biosensors. *Anal. Chim. Acta.* **2002,** *469* (1), 63-71.

102. Li, J.; Ng, H. T.; Cassell, A.; Fan, W.; Chen, H.; Ye, Q.; Koehne, J.; Han, J.; Meyyappan, M., Carbon Nanotube Nanoelectrode Array for Ultrasensitive DNA Detection. *Nano Lett.* **2003,** *3*, 597-602.

103. Palecek, E.; Jelen, F.; Trnkova, L., Cyclic Voltammetry of DNA at a Mercury Electrode: an Anodic Peak Specific for Quanine. *Gen. Physiol. Biophys.* **1986,** *5* (3), 315-329.

104. Li, J.; Ng, H. T.; Cassell, A.; Fan, W.; Chen, H.; Ye, Q.; Koehne, J.; Han, J.; Meyyappan, M., Carbon Nanotube Nanoelectrode Array for Ultrasensitive DNA Detection. *Nano Lett.* **2003,** *3* (5), 597-602.

105. Sigal, G. B.; Mrksich, M.; Whitesides, G. M., Using Surface Plasmon Resonance Spectroscopy to Measure the Association of Detergens with Self-Assembled Monolayers of Hexadecanethiolate on Gold. *Langmuir* **1997,** *13*, 2749-2755.

106. Patching, S. G., Surface Plasmon Resonance Spectroscopy for Characterisation of Membrane Protein–Ligand Interactions and Its Potential for Drug Discovery. *Biochim. Biophy. Acta - Biomembranes* **2014,** *1838* (1, Part A), 43-55.

107. Bakhtiar, R., Surface Plasmon Resonance Spectroscopy: A Versatile Technique in a Biochemist's Toolbox. *J. Chem. Edu.* **2012,** *90* (2), 203-209.

108. Kick, A.; Bonsch, M.; Katzschner, B.; Viogt, J.; Herr, A.; Brabetz, W.; Jung, M.; Sonntag, F.; Klotzbach, U.; Danz, N.; Howitz, S.; Mertig, M., DNA Microarrays for Hybridization Detection by Surface Plasmon Resonance Spectroscopy. *Biosens. Bioelectron.* **2010,** *26*, 1543-1547.

109. Rich, R. L.; Myszka, D. G., Why You Should be Using More SPR Biosensor Technology. *Drug Discov. Today Technol.* **2004,** *5*, 1-8.

110. Melechko, A. V.; Merkulov, V. I.; Mcknight, T. E.; Guillorn, M. A.; Klein, K. L.; Lowndes, D. H.; Simpson, M. L., Vertically Aligned Carbon Nanofibers and Related Structures: Controlled Synthesis and Directed Assembly. *J. App. Phys.* **2005,** *97*, 041301.

111. Huang, J.; Liu, Y.; You, T., Carbon Nanofiber Based Electrochemical Biosensors: A Review. *Anal. Med.* **2010,** *2*, 202-211.

112. Serp, P.; Corrias, M.; Kalck, P., Carbon Nanotubes and Nanofibers in Catalysis. *Appl. Catal. A: General* **2003,** *253* (2), 337-358.

113. Vamvakaki, V.; Tsagaraki, K.; Chaniotakis, N., Carbon Nanofiber-Based Glucose Biosensor. *Anal. Chem.* **2006,** *78* (15), 5538-5542.

114. Kim, S.-U.; Lee, K.-H., Carbon Nanofiber Composites for the Electrodes of Electrochemical Capacitors. *Chem. Phys. Lett.* **2004,** *400* (1–3), 253-257.

115. Wang, J.; Lin, Y., Functionalized Carbon Nanotubes and Nanofibers for Biosensing Applications. *Trends Anal. Chem.* **2008,** *27* (7), 619-626.

116. Merkulov, V. I.; Melechko, A. V.; Guillorn, M. A.; Lowndes, D. H.; Simpson, M. L., Alignment Mechanism of Carbon Nanofibers Produced by Plasma-Enhanced Chemical-Vapor Deposition. *Appl. Phys. Lett.* **2001,** *79* (18), 2970-2972.

117. Li, J.; Koehne, J. E.; Cassell, A. M.; Chen, H.; Ng, H. T.; Ye, Q.; Fan, W.; Han, J.; Meyyappan, M., Inlaid Multi-Walled Carbon Nanotube Nanoelectrode Arrays for Electroanalysis. *Electroanalysis* **2005,** *17* (1), 15-27.

118. Arrigan, D. W. M., Nanoelectrodes, Nanoelectrode Arrays and Their Applications. *Analyst* **2004,** *129* (12), 1157-1165.

119. Arumugam, P. U.; Chen, H.; Siddiqui, S.; Weinrich, J. A. P.; Jejelowo, A.; Li, J.; Meyyappan, M., Wafer-Scale Fabrication of Patterned Carbon Nanofiber Nanoelectrode Arrays:

A Route for Development of Multiplexed, Ultrasensitive Disposable Biosensors. *Biosens. Bioelectron.* **2009,** *24* (9), 2818-2824.

120. Murthy, R. V.; Arbman, G.; Gao, J.; Roodman, G. D.; Sun, X.-F., Legumain Expression in Relation to Clinicopathologic and Biological Variables in Colorectal Cancer. *Clin. Cancer Res.* **2005,** *11* (6), 2293-2299.

121. Shirahama-Noda, K.; Yamamoto, A.; Sugihara, K.; Hashimoto, N.; Asano, M.; Nishimura, M.; Hara-Nishimura, I., Biosynthetic Processing of Cathepsins and Lysosomal Degradation are Abolished in Asparaginyl Endopeptidase-Deficient Mice. *J. Biol. Chem.* **2003,** *278* (35), 33194-33199.

122. Mattock, K. L.; Gough, P. J.; Humphries, J.; Burnand, K.; Patel, L.; Suckling, K. E.; Cuello, F.; Watts, C.; Gautel, M.; Avkiran, M.; Smith, A., Legumain and Cathepsin-L Expression in Human Unstable Carotid Plaque. *Atherosclerosis* **2010,** *208* (1), 83-89.

123. Gawenda, J.; Traub, F.; Lück, H.; Kreipe, H.; von Wasielewski, R., Legumain Expression as a Prognostic Factor in Breast Cancer Patients. *Breast Cancer Res. Treat.* **2007,** *102* (1), 1-6.

124. Briggs, J.; Haugen, M.; Johansen, H.; Riker, A.; Abrahamson, M.; Fodstad, O.; Maelandsmo, G.; Solberg, R., Cystatin E/M Suppresses Legumain Activity and Invasion of Human Melanoma. *BMC Cancer* **2010,** *10* (1), 17.

125. Turk, B., Targeting Proteases: Successes, Failures and Future Prospects. *Nat. Rev. Drug Discov.* **2006,** *5* (9), 785-799.

126. Tang, Z.; Wu, H.; Zhang, Y.; Li, Z.; Lin, Y., Enzyme-Mimic Activity of Ferric Nano-Core Residing in Ferritin and Its Biosensing Applications. *Anal. Chem.* **2011,** *83* (22), 8611-8616.

127. Shimura, K.; Kasai, K.-i.; Matsumoto, H., Assay of Trypsin Activity by Capillary Isoelectric Focusing with Laser-Induced Fluorescence Detection. *Electrophoresis* **1998,** *19* (13), 2296-2300.

128. Vestling, M. M.; Murphy, C. M.; Fenselau, C., Recognition of Trypsin Autolysis Products by High-Performance Liquid Chromatography and Mass Spectrometry. *Anal. Chem.* **1990,** *62* (21), 2391-2394.

129. Orosco, M. M.; Pacholski, C.; Miskelly, G. M.; Sailor, M. J., Protein-Coated Porous-Silicon Photonic Crystals for Amplified Optical Detection of Protease Activity. *Adv. Mater.* **2006,** *18* (11), 1393-1396.

130. Hook, V. Y. H. S., M. R. ; Nguye, C. ; Yasothornsrikul, S. , Production of Radiolabeled Neuropeptide Precursors by in Vitro Transcription and Translation. *Pept. Res.* **1996,** *9*, 183-187.

131. Ohtsuka, K.; Maekawa, I.; Waki, M.; Takenaka, S., Electrochemical Assay of Plasmin Activity and Its Kinetic Analysis. *Anal. Biochem.* **2009,** *385* (2), 293-299.

132. Penner, R. M.; Heben, M. J.; Longin, T. L.; Lewis, N. S., Fabrication and Use of Nanometer-Sized Electrodes in Electrochemistry. *Science* **1990,** *250*, 1118-1121.

133. Fan, F.-R. F.; Bard, A. J., Electrochemical Detection of Single Molecules. *Science* **1995,** *267*, 871-874.

134. Menon, V. P.; Martin, C. R., Fabrication and Evaluation of Nanoelectrode Ensembles. *Anal. Chem.* **1995,** *67* (13), 1920-1928.

135. Wei, D.; Bailey, M. J. A.; Andrew, P.; Ryhanen, T., Electrochemical Biosensors at The Nanoscale. *Lab Chip* **2009,** *9* (15), 2123-2131.

136. Lapierre-Devlin, M. A.; Asher, C. L.; Taft, B. J.; Gasparac, R.; Roberts, M. A.; Kelley, S. O., Amplified Electrocatalysis at DNA-Modified Nanowires. *Nano Lett.* **2005,** *5* (6), 1051-1055.

137. Lanyon, Y. H.; De Marzi, G.; Watson, Y. E.; Quinn, A. J.; Gleeson, J. P.; Redmond, G.; Arrigan, D. W. M., Fabrication of Nanopore Array Electrodes by Focused Ion Beam Milling. *Anal. Chem.* **2007,** *79* (8), 3048-3055.

138. Huaqing, L.; Nianqiang, W., A Large-Area Nanoscale Gold Hemisphere Pattern as a Nanoelectrode Array. *Nanotechnology* **2008,** *19* (27), 275301.

139. Lin, Y. H.; Lu, F.; Tu, Y.; Ren, Z. F., Glucose Biosensors Based On Carbon Nanotube Nanoelectrode Ensembles. *Nano Lett.* **2004,** *4* (2), 191-195.

140. Baker, S. E.; Tse, K. Y.; Lee, C. S.; Hamers, R. J., Fabrication and Characterization of Vertically Aligned Carbon Nanofiber Electrodes for Biosensing Applications. *Diamond Relat. Mater.* **2006,** *15* (2-3), 433-439.

141. Arumugam, P. U.; Chen, H.; Siddiqui, S.; Weinrich, J. A. P.; Jejelowo, A.; Li, J.; Meyyappan, M., Wafer-scale Fabrication of Patterned Carbon Nanofiber Nanoelectrode Arrays: A route for Development of Multiplexed, Ultrasensitive Disposable Biosensors. *Biosens. Bioelectron.* **2009,** *24* (9), 2818-2824.

142. Koehne, J. E.; Marsh, M.; Boakye, A.; Douglas, B.; Kim, I. Y.; Chang, S.-Y.; Jang, D.-P.; Bennet, K. E.; Kimble, C.; Andrews, R.; Meyyappan, M.; Lee, K. H., Carbon Nanofiber Electrode Array for Electrochemical Detection of Dopamine Using Fast Scan Cyclic Voltammetry. *Analyst* **2010,** *136* (9), 1802-1805.

143. Yu, Z.; McKnight, T. E.; Ericson, M. N.; Melechko, A. V.; Simpson, M. L.; Morrison, B., Vertically Aligned Carbon Nanofiber Arrays Record Electrophysiological Signals From Hippocampal Slices. *Nano Lett.* **2007,** *7* (8), 2188-2195.

144. McKnight, T. E.; Melechko, A. V.; Hensley, D. K.; Mann, D. G. J.; Griffin, G. D.; Simpson, M. L., Tracking Gene Expression After DNA Delivery Using Spatially Indexed Nanofiber Arrays. *Nano Lett.* **2004,** *4* (7), 1213-1219.

145. Koehne, J.; Li, J.; Cassell, A. M.; Chen, H.; Ye, Q.; Ng, H. T.; Han, J.; Meyyappan, M., The Fabrication and Electrochemical Characterization of Carbon Nanotube Nanoelectrode Arrays. *J. Mater. Chem.* **2004,** *14* (4), 676-684.

146. Banks, C. E.; Davies, T. J.; Wildgoose, G. G.; Compton, R. G., Electrocatalysis at Graphite and Carbon Nanotube Modified Electrodes: Edge-Plane sites and Tube Ends are the Reactive Sites. *Chem. Commun.* **2005,** *2005* (7), 829-841.

147. Gutiérrez, O. A.; Chavez, M.; Lissi, E., A Theoretical Approach to Some Analytical Properties of Heterogeneous Enzymatic Assays. *Anal. Chem.* **2004,** *76* (9), 2664-2668.

148. Creager, S.; Yu, C. J.; Bamdad, C.; O'Connor, S.; MacLean, T.; Lam, E.; Chong, Y.; Olsen, G. T.; Luo, J. Y.; Gozin, M.; Kayyem, J. F., Electron Transfer at Electrodes Through Conjugated "Molecular Wire" Bridges. *J. Am. Chem. Soc.* **1999,** *121* (5), 1059-1064.

149. Almeida, P. C.; Oliveira, V.; Chagas, J. R.; Meldal, M.; Juliano, M. A.; Juliano, L., Hydrolysis by Cathepsin B of Fluorescent Peptides Derived From Human Prorenin. *Hypertension* **2000,** *35* (6), 1278-1283.

150. Nägler, D. K.; Storer, A. C.; Portaro, F. C. V.; Carmona, E.; Juliano, L.; Ménard, R., Major increase in endopeptidase activity of human cathepsin B upon removal of occluding loop contacts. *Biochem.* **1997,** *36* (41), 12608-12615.

151. Therrien, C.; Lachance, P.; Sulea, T.; Purisima, E. O.; Qi, H. T.; Ziomek, E.; Alvarez-Hernandez, A.; Roush, W. R.; Menard, R., Cathepsins X and B Can Be Differentiated Through

Their Respective Mono- and Dipeptidyl Carboxypeptidase Activities. *Biochem.* **2001,** *40* (9), 2702-2711.

152. Saleh, Y.; Wnukeiwicz, J.; Andrzeijak, R.; Trziszka, T.; Siewinski, M.; Ziolkowski, P.; Kopec, W., Cathepsin B and Cysteine Protease Inhibitors in Human Tongue Cancer: Correlation with Tumor Staging and In Vitro Inhibition of Cathepsin B by Chicken Cystatin. *J. Cancer Mol.* **2006,** *2* (2), 67-72.

153. Fujise, N.; Nanashima, A.; Taniguchi, Y.; Matsuo, S.; Hatano, K.; Matsumoto, Y.; Tagawa, Y.; Ayabe, H., Prognostic Impact of Cathepsin B and Matrix Metalloproteinase-9 in Pulmonary Adenocarcinomas by Immunohistochemical Study. *Lung Cancer* **2000,** *27* (1), 19-26.

154. Tumminello, F.; Leto, G.; Pizzolanti, G.; Candiloro, V.; Crescimanno, M.; Crosta, L.; Flandina, C.; Montalto, G.; Soresi, M.; Carroccio, A.; Bascone, F.; Ruggeri, I.; Ippolito, S.; Gebbia, N., Cathepsin D, B and L Circulating Levels as Prognostic Markers of Malignant Progression. *Anticancer Res.* **1996,** *16*, 2315-2320.

155. Kos, J.; Lah, T. T., Cysteine Proteinases and Their Endogenous Inhibitors: Target Proteins for Prognosis, Diagnosis and Therapy in Cancer (Review). *Oncol. Rep.* **1998,** *5* (6), 1349-1361.

156. Duffy, M. J., Proteases as Prognostic Markers in Cancer. *Clin. Cancer Res.* **1996,** *2* (4), 613-618.

157. Kandalaft, P. L.; Chang, K. L.; Ahn, C. W.; Traweek, S. T.; Mehta, P.; Battifora, H., Prognostic Significance of Immunohistochemical Analysis of Cathepsin D in Low-Stage Breast Cancer. *Cancer* **1993,** *71* (9), 2756-2763.

158. Hirai, K.; Yokoyama, M.; Asano, G.; Tanaka, S., Expression of Cathepsin B and Cystatin C in Human Colorectal Cancer. *Hum. Path.* **1999,** *30* (6), 680-686.

159. Kawasaki, G.; Kato, Y.; Mizuno, A., Cathepsin Expression in Oral Squamous Cell Carcinoma: Relationship with Clinicopathologic Factors. *Oral Surg., Oral Med., Oral Pathol., Oral Radiol. Endod.* **2002,** *93* (4), 446-454.

160. Macabeo-Ong, M.; Shiboski, C. H.; Silverman, S.; Ginzinger, D. G.; Dekker, N.; Wong, D. T. W.; Jordan, R. C. K., Quantitative Analysis of Cathepsin L mRNA and Protein Expression During Oral Cancer Progression. *Oral Oncol.* **2003,** *39* (7), 638-686.

161. Lah, T. T.; Cercek, M.; Blejec, A.; Kos, J.; Gorodetsky, E.; Somers, R.; Daskal, I., Cathepsin B, a Prognostic Indicator in Lymph Node-negative Breast Carcinoma Patients: Comparison with Cathepsin D, Cathepsin L, and Other Clinical Indicators. *Clin. Cancer Res.* **2000,** *6* (2), 578-584.

162. Li, J.; Li, Y.-F.; Swisher, L. Z.; Syed, L. U.; Prior, A. M.; Nguyen, T. A.; Hua, D. H., In *SPIE Proc. on Biosensing and Nanomedicine V*, SPIE: San Diego, CA, 2012; Vol. 8460, pp 84600L-84600L.

163. Kotaska, K.; Dusek, P.; Prusa, R.; Vesely, S.; Babjuk, M., Urine and Serum Cathepsin B Concentrations in the Transitional Cell Carcinoma of the Bladder. *J. Clin. Lab Anal.* **2012,** *26*, 61-65.

164. Sahai, E., Mechanisms of Cancer Cell Invasion. *Curr. Opin. Genet. Dev.* **2005,** *15* (1), 87-96.

165. Lee, M.; Fridman, R.; Mobashery, S., Extracellular Proteases as Targets for Treatment of Cancer Metastases. *Chem. Soc. Rev.* **2004,** *33*, 401-409.

166. Nouh, M. A.; Mohamed, M. M.; El-Shinawi, M.; Shaalan, M. A.; Cavallo-Medved, D.; Khaled, H. M.; Sloane, B. F., Cathepsin B: a Potential Prognostic Marker for Inflammatory Breast Cancer. *J. Tans. Med.* **2011,** *9*, 1-8.

167. Mort, J. S., Chapter 406 - Cathepsin B. In *Handbook of Proteolytic Enzymes*, 3th ed.; Rawlings, N. D.; Salvesen, G., Eds. Academic Press: San Diego, 2013; Vol. 2, pp 1784-1791.

168. Barrett, A. J.; Kirschke, H., Cathepsin B, Cathepsin H, and Cathepsin L. *Methods Enzymol.* **1981,** *80*, 535-561.

169. Elliott, E.; Sloane, B. F., The Cysteine Protease Cathepsin B in Cancer. *Perspect. Drug Discov.* **1996,** *6*, 12-32.

170. Chen, Q.; Fei, J.; Wu, L.; Jiang, Z.; Wu, Y.; Zheng, Y.; Lu, G., Detection of Cathepsin B, Cathepsin L, Cystatin C, Urokinase Plasminogen Activator and Urokinase Plasminogen Activator Receptor in the Sera of Lung Cancer Patients. *Oncol. lett.* **2011,** *2*, 693-99.

171. Emmert-Buck, M. R.; Roth, M. J.; Zhuang, Z.; Campo, E.; Rozhin, J.; Sloane, B. F.; Liotta, L. A.; Stetler-Stevenson, W. G., Increased Gelatinanse A (MMP-2) and Cathepsin B Activity in Invasive Tumor Regions of Human Colon Cancer Samples. *Am. J. Pathol.* **1994,** *145*, 1285-1290.

172. Muss, H. B., Endocrine Therapy for Advanced Breast Cancer: a Review. *Breast Cancer Res. Treat.* **1992,** *21*, 15-26.

173. Santen, R. J.; Manni, A.; Harvey, H.; Redmond, C., Endocrine Treatment of Breast Cancer in Women. *Endocr. Rev.* **1990,** *11*, 221-265.

174. Lerner, L. J.; C., J. V., Development of Antiestrogens and Their Use in Breast Cancer: Eighth Cain Memorial Award Lecture. *Cancer Res.* **1990,** *50*, 4177-4189.

175. Jordan, V. C., Alternate Antiestrogens and Approaches to the Prevention of Breast Cancer. *J. Cell Biochem. Suppl.* **1995,** *22*, 51-57.

176. Morrow, M.; Jordan, V. C., Molecular Mechanisms of Resistance to Tamoxifen Therapy in Breast Cancer. *Arch. Surg.* **1993,** *128*, 1187-1191.

177. Clark, G. M.; G., H. S.; Ravdin, P. M.; De Laurentiis, M.; Osborne, C. K., Prognostic Factors: Rationale and Methods of Analysis and Integration. *Breast Cancer Res. Treat.* **1994,** *32*, 105-112.

178. Ethier, S. P., Growth Factor Synthesis and Human Breast Cancer Progression. *J. Natl. Cancer Inst.* **1995,** *87*, 964-973.

179. Dickson, R. B.; Lippman, M. E., Growth Factors in Breast Cancer. *Endocr. Rev.* **1995,** *16*, 559-589.

180. King, M. C., Breast Cancer Genes: How many, Where and Who are They? *Nat. Genet.* **1992,** *2*, 89-90.

181. Cotrin, S. S.; Puzer, L.; de Souza Judice, W. A.; Juliano, L.; Carmona, A. K.; Juliano, M. A., Positional-Scanning Combinatorial Libraries of Fluorescence Resonance Energy Transfer Peptides to Define Substrate Specificity of Carboxydipeptidases: Assays with Human Cathepsin B. *Anal. Biochem.* **2004,** *335* (2), 244-252.

182. Su, Y.; Chen, H.; Wang, Z.; Lv, Y., Recent Advances in Chemiluminescence. *Appl. Spectrosc. Rev.* **2007,** *42* (2), 139-176.

183. Barni, F.; Lewis, S. W.; Berti, A.; Miskelly, G. M.; Lago, G., Forensic Application of the Luminol Reaction as a Presumptive Test for Latent Blood Detection. *Talanta* **2007,** *72* (3), 896-913.

184. Rechberger, W.; Hohenau, A.; Leitner, A.; Krenn, J. R.; Lamprecht, B.; Aussenegg, F. R., Optical Properties of Two Interacting Gold Nanoparticles. *Opt. Commun.* **2003,** *220* (1-3), 137-141.

185. Schmid, G.; Simon, U., Gold Nanoparticles: Assembly and Electrical Properties in 1-3 Dimensions. *Chem. Commun.* **2005,** (6), 697-710.

186. Jain, P. K.; Lee, K. S.; El-Sayed, I. H.; El-Sayed, M. A., Calculated Absorption and Scattering Properties of Gold Nanoparticles of Different Size, Shape, and Composition: Applications in Biological Imaging and Biomedicine. *J. Phys. Chem. B* **2006,** *110* (14), 7238-7248.

187. Abad, J. M.; Mertens, S. F. L.; Pita, M.; Fernández, V. M.; Schiffrin, D. J., Functionalization of Thioctic Acid-Capped Gold Nanoparticles for Specific Immobilization of Histidine-Tagged Proteins. *J. Am. Chem. Soc.* **2005,** *127* (15), 5689-5694.

188. Hostetler, M. J.; Green, S. J.; Stokes, J. J.; Murray, R. W., Monolayers in Three Dimensions: Synthesis and Electrochemistry of ω-Functionalized Alkanethiolate-Stabilized Gold Cluster Compounds. *J. Am. Chem. Soc.* **1996,** *118* (17), 4212-4213.

189. Hostetler, M. J.; Wingate, J. E.; Zhong, C.-J.; Harris, J. E.; Vachet, R. W.; Clark, M. R.; Londono, J. D.; Green, S. J.; Stokes, J. J.; Wignall, G. D.; Glish, G. L.; Porter, M. D.; Evans, N. D.; Murray, R. W., Alkanethiolate Gold Cluster Molecules with Core Diameters from 1.5 to 5.2 nm: Core and Monolayer Properties as a Function of Core Size. *Langmuir* **1998,** *14* (1), 17-30.

190. Bartz, M.; Kuther, J.; Nelles, G.; Weber, N.; Seshadri, R.; Tremel, W., Monothiols Derived from Glycols as Agents for Stabilizing Gold Colloids in Water: Synthesis, Self-Assembly and Use as Crystallization Templates. *J. Mater. Chem.* **1999,** *9* (5), 1121-1125.

191. Mirkin, C. A.; Letsinger, R. L.; Mucic, R. C.; Storhoff, J. J., A DNA-Based Method for Rationally Assembling Nanoparticles into Macroscopic Materials. *Nature* **1996,** *382* (6592), 607-609.

192. Alivisatos, A. P.; Johnsson, K. P.; Peng, X.; Wilson, T. E.; Loweth, C. J.; Bruchez, M. P.; Schultz, P. G., Organization of 'nanocrystal molecules' using DNA. *Nature* **1996,** *382* (6592), 609-611.

193. Lee, J.-S.; Ulmann, P. A.; Han, M. S.; Mirkin, C. A., A DNA-Gold Nanoparticle-Based Colorimetric Competition Assay for the Detection of Cysteine. *Nano Lett.* **2008,** *8* (2), 529-533.

194. Su, X.; Kanjanawarut, R., Control of Metal Nanoparticles Aggregation and Dispersion by PNA and PNAâ^'DNA Complexes, and Its Application for Colorimetric DNA Detection. *ACS Nano* **2009,** *3* (9), 2751-2759.

195. Kim, J.-Y.; Lee, J.-S., Synthesis and Thermally Reversible Assembly of DNA@Gold Nanoparticle Cluster Conjugates. *Nano Lett.* **2009,** *9* (12), 4564-4569.

196. Yang, X.; Guo, Y.; Wang, A., Luminol/antibody Labeled Gold Nanoparticles for Chemiluminescence Immunoassay of Carcinoembryonic Antigen. *Anal. Chim. Acta* **2010,** *666* (1-2), 91-96.

197. Prilutsky, D.; Shneider, E.; Shefer, A.; Rogachev, B.; Lobel, L.; Last, M.; Marks, R. S., Differentiation between Viral and Bacterial Acute Infections Using Chemiluminescent Signatures of Circulating Phagocytes. *Anal. Chem.* **2011,** *83* (11), 4258-4265.

198. Tsukagoshi, K.; Nakahama, K.; Nakajima, R., Direct Detection of Biomolecules in a Capillary Electrophoresis−Chemiluminescence Detection System. *Anal. Chem.* **2004,** *76* (15), 4410-4415.

199. Liu, B.-F.; Ozaki, M.; Utsumi, Y.; Hattori, T.; Terabe, S., Chemiluminescence Detection for a Microchip Capillary Electrophoresis System Fabricated in Poly(dimethylsiloxane). *Anal. Chem.* **2002,** *75* (1), 36-41.

200. Bergervoet, P. W. M.; van Riessen, N.; Sebens, F. W.; van der Zwet, W. C., Application of the Forensic Luminol for Blood in Infection Control. *J. Hosp. Infect.* **2008,** *68* (4), 329-333.

201. Kim, H.-S.; Pyun, J.-C., Hyper Sensitive Strip Test with Chemi-luminescence Signal Band. *Procedia Chem.* **2009,** *1* (1), 1043-1046.

202. Zhang, Z.-F.; Cui, H.; Lai, C.-Z.; Liu, L.-J., Gold Nanoparticle-Catalyzed Luminol Chemiluminescence and Its Analytical Applications. *Anal. Chem.* **2005,** *77* (10), 3324-3329.

203. Duan, C. F.; Cui, H.; Zhang, Z. F.; Liu, B.; Guo, J. Z.; Wang, W., Size-Dependent Inhibition and Enhancement by Gold Nanoparticles of Luminol-Ferricyanide Chemiluminescence. *J. Phys. Chem. C* **2007,** *111* (12), 4561-4566.

204. Zhao, L.; Sun, L.; Chu, X., Chemiluminescence Immunoassay. *Trends Anal. Chem.* **2009,** *28* (4), 404-415.

205. Brown, L.; Koerner, T.; Horton, J. H.; Oleschuk, R. D., Fabrication and Characterization of Poly(methylmethacrylate) Microfluidic Devices Bonded Using Surface Modifications and Solvents. *Lab Chip* **2006,** *6* (1), 66-73.

206. Li, D.; He, Q.; Cui, Y.; Duan, L.; Li, J., Immobilization of Glucose Oxidase onto Gold Nanoparticles with Enhanced Thermostability. *Biochem. Biophys. Res. Commun.* **2007,** *355* (2), 488-493.

207. Silverstein, R. M.; Bassler, G. C.; Morrill, T. C., *Spectrometric Identification of Organic Compounds. 4th ed.* . John Wiley and Sons: New York, 1981.

208. Cui, H.; Wang, W.; Duan, C.-F.; Dong, Y.-P.; Guo, J.-Z., Synthesis, Characterization, and Electrochemiluminescence of Luminol-Reduced Gold Nanoparticles and Their Application in a Hydrogen Peroxide Sensor. *Chem. Eur. J.* **2007,** *13* (24), 6975-6984.

209. White, E. H.; Zafiriou, O.; Kagi, H. H.; Hill, J. H. M., Chemilunimescence of Luminol: The Chemcial Reaction. *J. Am. Chem. Soc.* **1964,** *86* (5), 940-941.

210. White, E. H.; Roswell, D. F., Chemiluminescence of Organic Hydrazides. *Acc. Chem. Res.* **1970,** *3* (2), 54-62.

211. Knox Van Dyke, C. V. D., Karen Woodfork, *Luminescence Biotechnology: Instrumentation and Applications*. CRC Press, New York: 2001.

212. Singh, M. P.; Strouse, G. F., Involvement of the LSPR Spectral Overlap for Energy Transfer between a Dye and Au Nanoparticle. *J. Am. Chem. Soc.* **2010,** *132* (27), 9383-9391.

213. Yun, C. S.; Javier, A.; Jennings, T.; Fisher, M.; Hira, S.; Peterson, S.; Hopkins, B.; Reich, N. O.; Strouse, G. F., Nanometal Surface Energy Transfer in Optical Rulers, Breaking the FRET Barrier. *J. Am. Chem. Soc.* **2005,** *127* (9), 3115-3119.

Appendix A - Supporting Information for Chapter 2&3

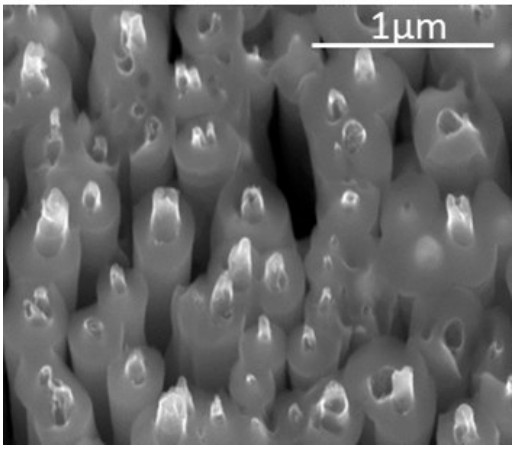

Figure A.1 Field-emission scanning electron microscopy image at 45° perspective view shows that VACNFs of ~150 nm in average diameter are encapsulated in SiO_2 matrix leaving only the tips exposed.

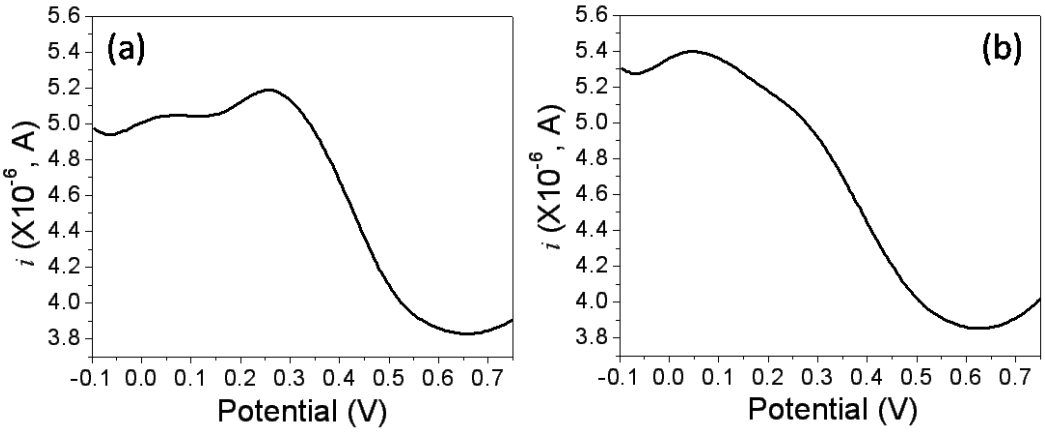

Figure A.2 The ACV of H_2N-$(CH_2)_4$-CO-Leu-Arg-Phe-Gly-NH-CH_2-Fc immobilized on the GCE (a) from the initial measurement and (b) from the measurement after 20 minutes. The AC frequency was 30 Hz and the amplitude was 25 mV. The measurement was done in 250 µL of 25 mM MES solution (pH 5.0).

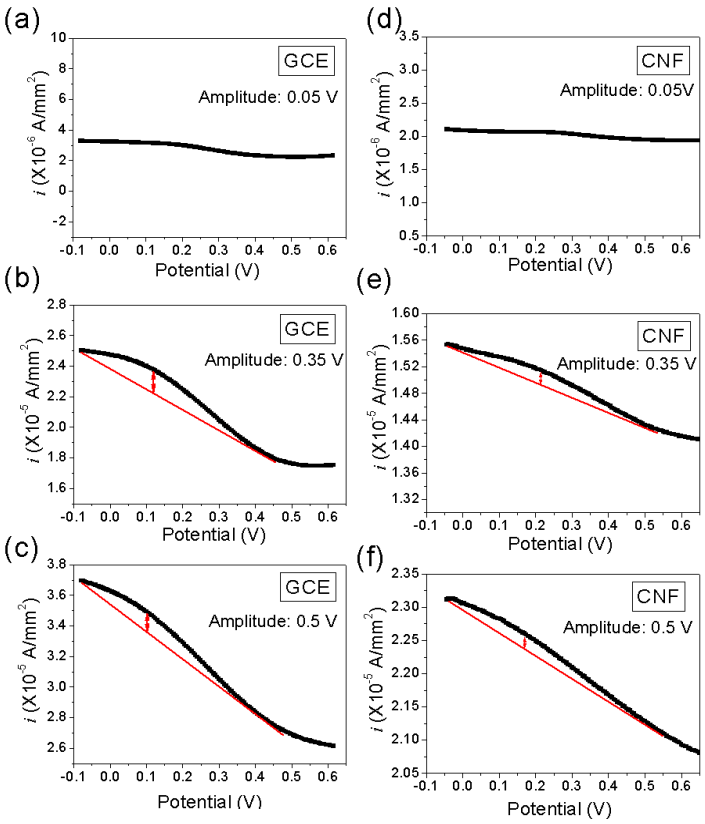

Figure A.3 Comparison of AC voltammograms (ACVs) of H_2N-$(CH_2)_4$-CO-Ala-Ala-Asn-Leu-NH-CH_2-Fc immobilized on a macroscopic glassy carbon electrode (GCE) (a–c) and a VACNF NEA (d–f) at the AC voltage amplitude of 0.05, 0.35 and 0.5 V. All the measurements were done in 500 µL of 50 mM MES (pH 5.0) and 250 mM NaCl. Sinusoidal waves with fixed frequency of 40 Hz for GCE and frequency of 1750 Hz for CNF NEA were superimposed on a DC staircase ramp from -0.05 to 0.65 V at a scan rate of 10 mV/s. The measured average AC current at each point was normalized by the 7.1 mm^2 geometric surface area defined by the 3-mm i.d. O-ring. The real CNF surface area is ~100 times less.

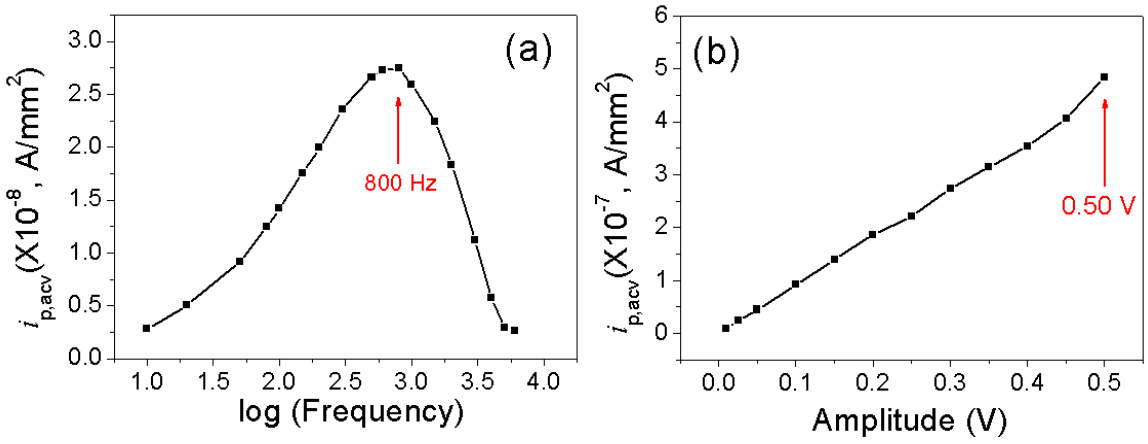

Figure A.4 (a) Background-corrected ACV peak current density $i_{p,acv}$ (normalized to the 7.1 mm^2 geometric electrode area) of H_2N-$(CH_2)_4$-CO-Leu-Arg-Phe-Gly-NH-CH_2-Fc immobilized on a VACNF NEA plotted against the logarithm of the frequency. (b) Background-corrected ACV peak current density $i_{p,acv}$ (normalized to the 7.1 mm^2 geometric electrode area) of H_2N-$(CH_2)_4$-CO-Leu-Arg-Phe-Gly-NH-CH_2-Fc immobilized on a VACNF NEA plotted against the amplitude. All the measurements were done in 250 µL of 25 mM MES (pH 5.0). Note: The real CNF surface area is ~100 times less than the geometric surface area defined by the O-ring.

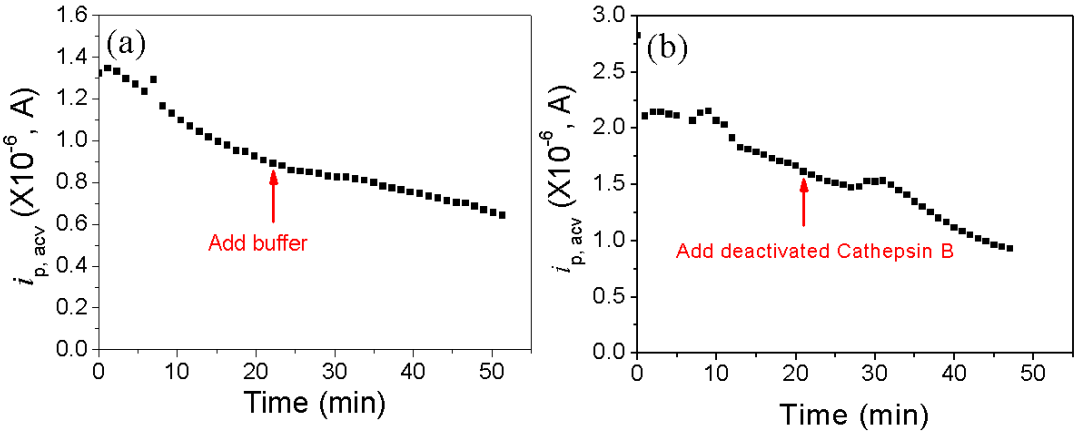

Figure A.5 Negative control experiments. The change of the peak current ($i_{p,acv}$) of H_2N-$(CH_2)_4$-CO-Leu-Arg-Phe-Gly-NH-CH_2-Fc immobilized on a VACNF NEA in continuously repeated

ACV measurements while (a) 25 µL of activation buffer consisting of 5 mM DTT and 25 mM MES (pH 5.0) and (b) the same buffer containing 9.8 ng μL^{-1} (338 nM) deactivated cathepsin B were added into the electrochemical cell containing 250 µL of 25 mM MES (pH 5.0). All ACV measurements were carried out at f = 800 Hz and AC voltage amplitude V_0 = 150 mV.

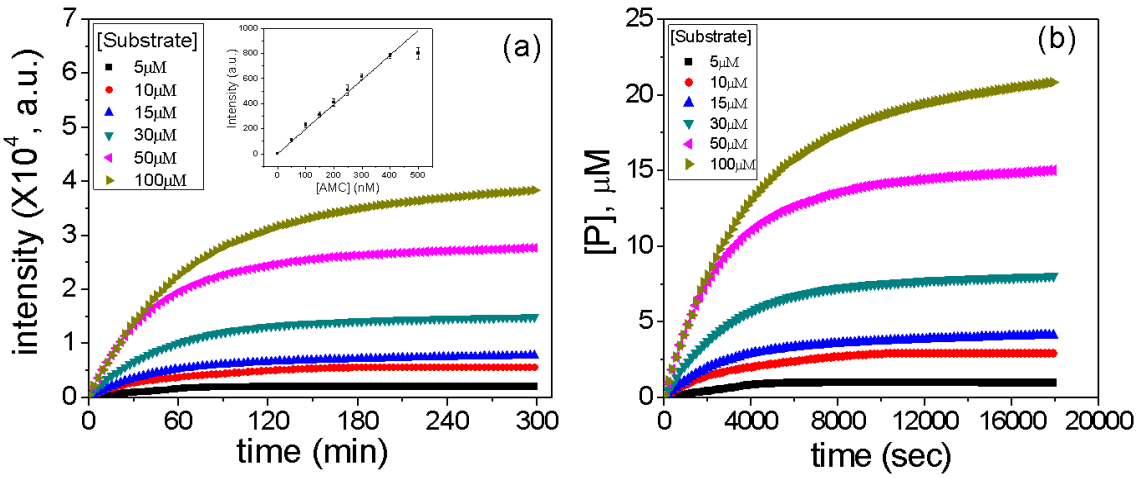

Figure A.6 (a) The kinetic curves of the fluorescence intensity of 0.1 ng μL^{-1} (3.45 nM) cathespin B reacting with different concentrations of substrate Z-Leu-Arg-AMC in 25 mM MES (pH 5.0). The cleavage between Arg and AMC released free AMC products which were strongly fluorescent and gave the increased fluorescence intensity. Inset: calibration curve of the fluorometer. (Excitation wavelength: 365 nm, emission wavelength: 410–460 nm) (b) The calibrated concentration of free AMC product during cathepsin B cleavage of various concentrations of substrate Z-Leu-Arg-AMC.

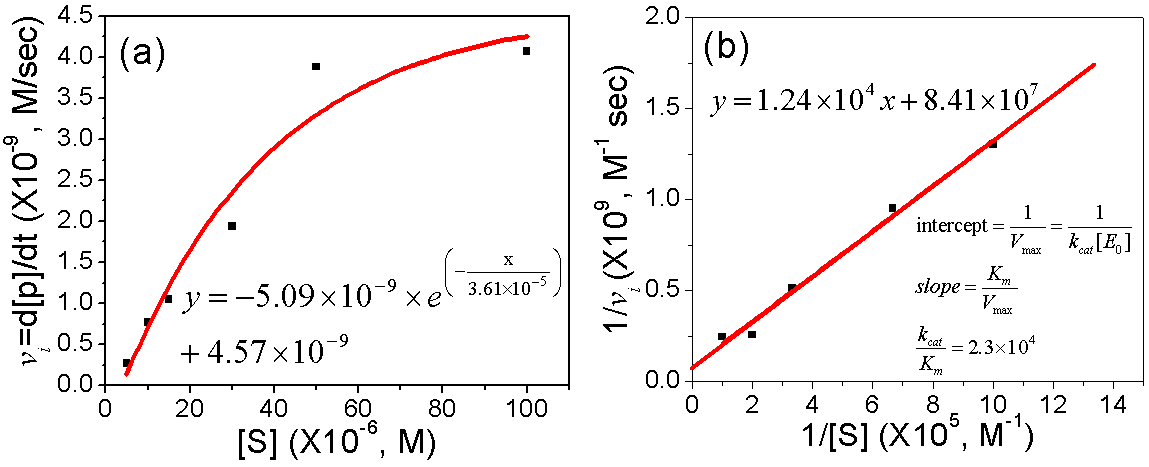

Figure A.7 (a) The initial proteolysis reaction rate v_i of cathepsin B plotted against the starting concentration of the substrate Z-Leu-Arg-AMC. The reaction rate was calculated from the slope of the tangent of the initial segment of the curves shown in Figure S8b. (b) Replot of the data presented in (a) and derivation of various catalytic constants. The value of k_{cat}/K$_m$ for cathepsin B was calculated as 2.3 x 10^4 $M^{-1}s^{-1}$.

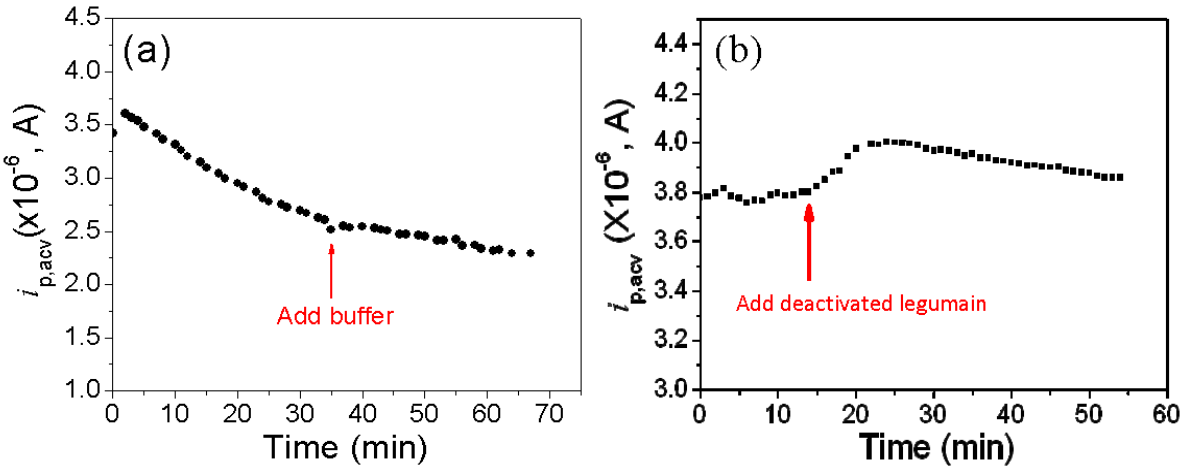

Figure A.8 Negative control experiments for legumain proteolysis. The change of the peak current ($i_{p,acv}$) of H_2N-$(CH_2)_4$-CO-Ala-Ala-Asn-Leu-NH-CH_2-Fc immobilized on a VACNF NEA in continuously repeated ACV measurements (a) while 11 µL of activation buffer

consisting of 50 mM CH_3COONa (pH = 4.0, adjusted by adding acetic acid) and 100 mM NaCl was added into the electrochemical cell containing 250 µL of 50 mM MES (pH 5.0) and 250 mM NaCl; (b) similar experiments by including 90.9 ng μL^{-1} (1.90 µM) deactivated legumain in the activation buffer. All ACV measurements were carried out at f = 1750 Hz and AC voltage amplitude V_0 = 150 mV.

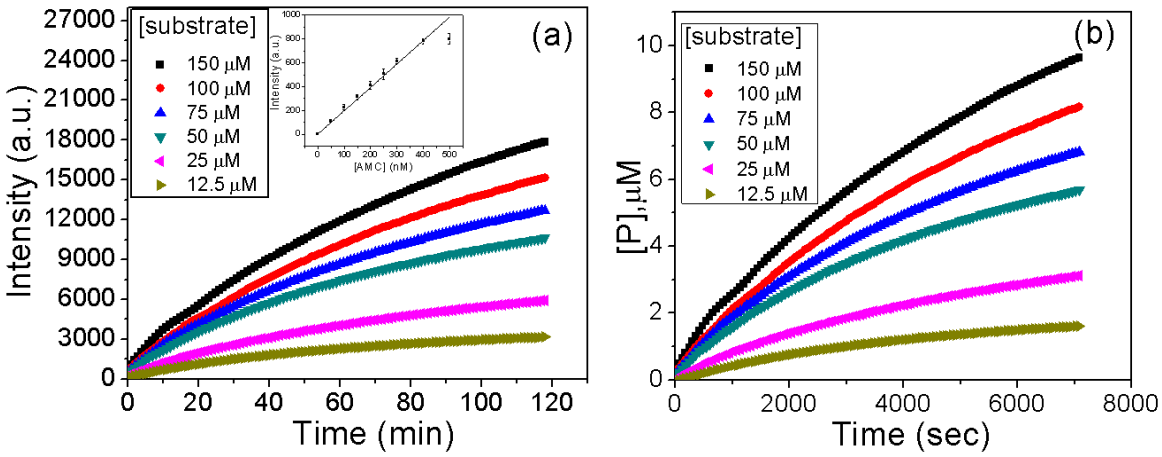

Figure A.9 (a) The fluorescence intensity curves of 0.5 ng μL^{-1} (10.2 nM) legumain reacting with different concentration of substrate Z-Ala-Ala-Asn-AMC in the assay buffer consisting of 50 mM MES (pH 5.0) and 250 mM NaCl. Inset: calibration curve of the fluorometer. (excitation wavelength: 365 nm, emission wavelength: 410–460 nm). (b) The calibrated free AMC product concentration during legumain cleavage the substrate Z-Ala-Ala-Asn-AMC.

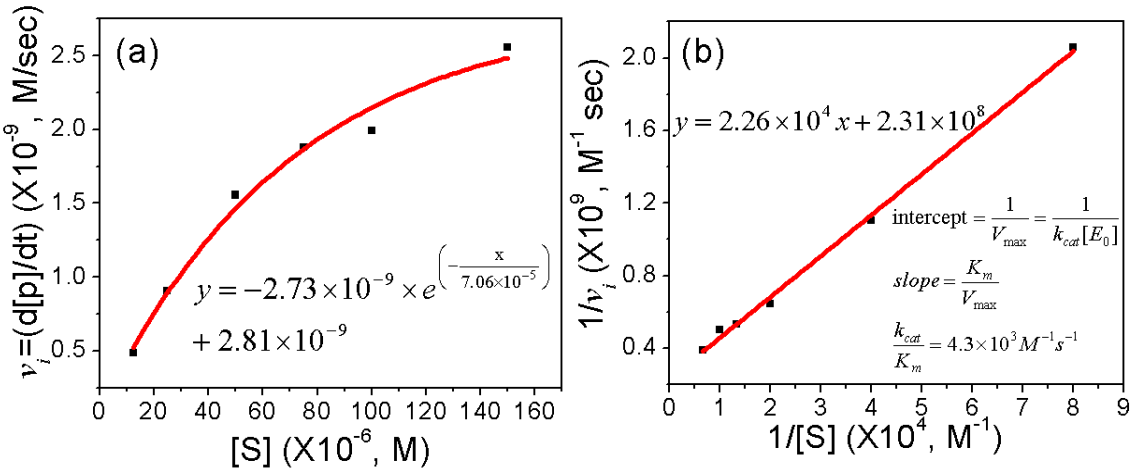

Figure A.10 (a) The initial proteolysis reaction rate v_i of legumain plotted against the concentration of the substrate Z-Ala-Ala-Asn-AMC. The reaction rate was calculated from the slope of the tangent of the initial segment of the curves shown in Figure S11b. (b) Replot of the data presented in (a) and the derivation of various catalytic constants. The value of k_{cat}/K$_m$ for legumain was calculated as 4.3 x 10^3 M^{-1}s^{-1}.

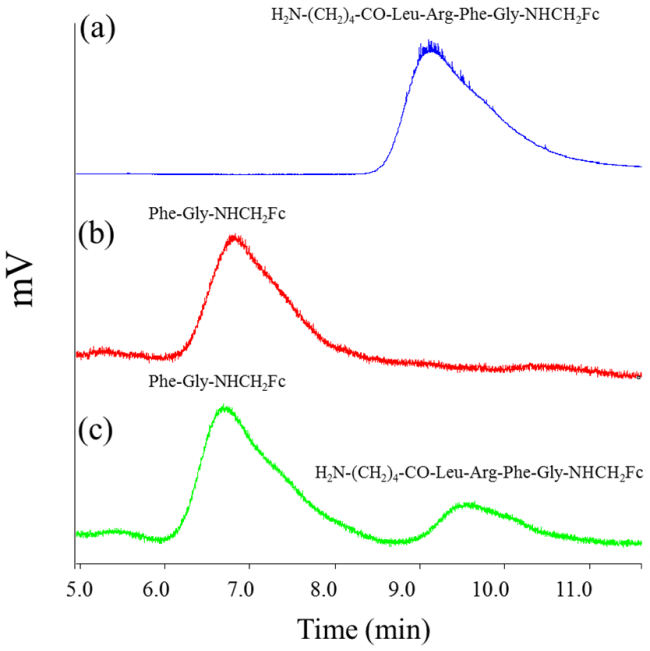

Figure A.11 (a) HPLC chart of H_2N-$(CH_2)_4$-CO-Leu-Arg-Phe-Gly-$NHCH_2Fc$ in 25 mM MES (pH 5.0) buffer. The tetrapeptide appeared at 9.4 minute in the HPLC chart and its structure was verified by mass spectrometry analysis. (b) HPLC chart of Phe-Gly-$NHCH_2Fc$ in 25 mM MES (pH 5.0) buffer. The dipeptide appeared at 6.7 minute in the HPLC chart and its structure was verified by mass spectrometry analysis. (c) HPLC chart of 6.35 mM H_2N-$(CH_2)_4$-CO-Leu-Arg-Phe-Gly-$NHCH_2Fc$ in 25 mM MES (pH 5.0) buffer incubated with 4.95 ng μl^{-1} (0.17 μM) *cathepsin B* for 2 hours. Absorbance peak at 6.7 minute was collected and lyophilized and mass spectrometry analysis showed it to be Phe-Gly-$NHCH_2Fc$. HPLC Method: a gradient elution from 10% to 50% of acetonitrile in 0.1 M phosphate buffer (pH = 6) over 40 minutes was used with a flow rate of 10 ml/min and detection wavelength λ at 254 nm. The column is Xperchrom AEGIS C18 120A 10 μm (Phenomenex).

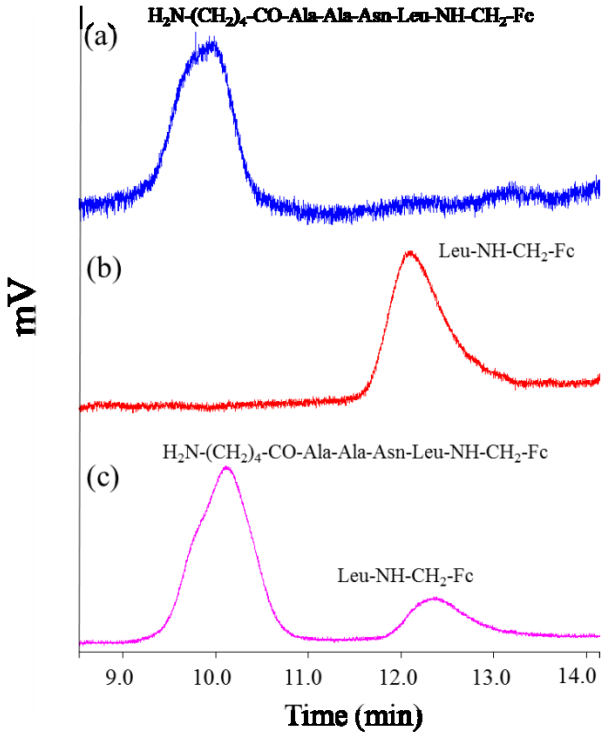

Figure A.12 (a) HPLC chart of H_2N-$(CH_2)_4$-CO-Ala-Ala-Asn-Leu-$NHCH_2Fc$ in 50 mM MES (pH 5.0) and 250 mM NaCl. The tetrapeptide appeared at 9.7 minute in the HPLC chart and its structure was verified by mass spectrometry analysis. (b) HPLC chart of Leu-$NHCH_2Fc$ in 50 mM MES (pH 5.0) and 250 mM NaCl. The Leu-$NHCH_2Fc$ appeared at 12.2 min in the HPLC chart and its structure was verified by mass spectrometry analysis. (c) HPLC chart of 100 μM H_2N-$(CH_2)_4$-CO-Ala-Ala-Asn-Leu-$NHCH_2Fc$ in 50 mM MES (pH 5.0) and 250 mM NaCl incubated with 98.7 ng/μL (2.01 μM) *legumain* for 2 hours. Absorbance peak at 12.2 min was collected and lyophilized and mass spectrometry analysis showed it to be Leu-$NHCH_2Fc$. HPLC Method: a gradient elution from 10% to 50% of acetonitrile in 0.1 M phosphate buffer (pH=6) over 40 minutes was used with a flow rate of 10 ml/min and detection wavelength λ at 254 nm. The column is Xperchrom AEGIS C18 120A 10 μm (Phenomenex).

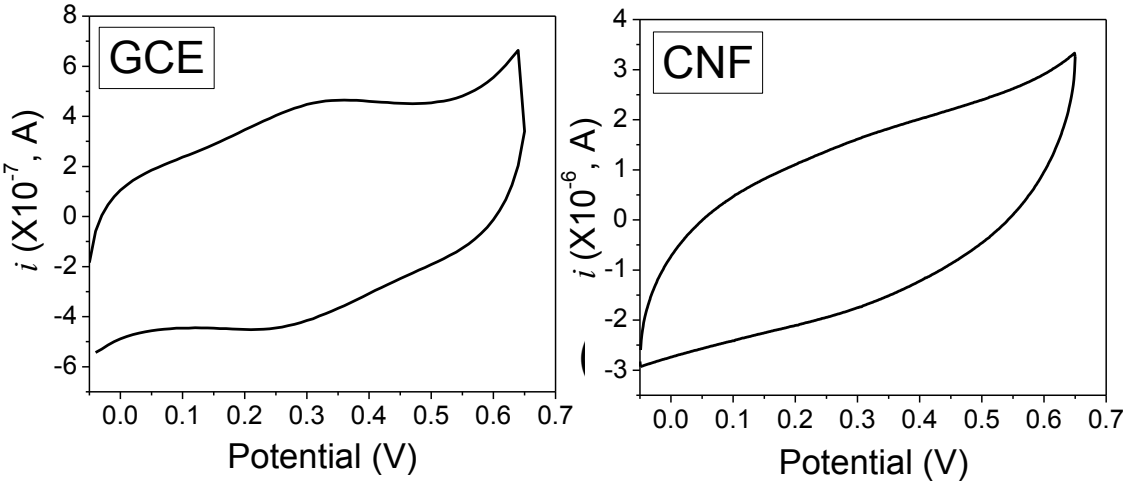

Figure A.13 Comparison of cyclic voltammetric measurements of H_2N-$(CH_2)_4$-CO-Ala-Ala-Asn-Leu-$NHCH_2$-Fc immobilized on (a) a macro-GCE and (b) a VACNF NEA. The measurements were carried out at the scan rate of 50 mV s^{-1} in 1 mL of 1.0 M KCl.

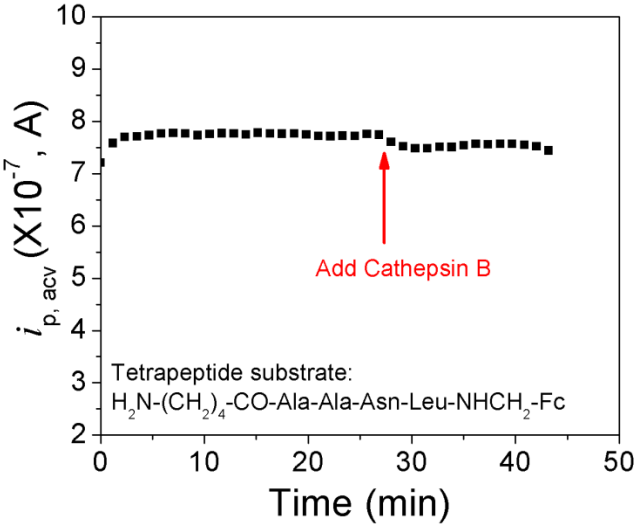

Figure A.14 Preliminary specificity testing result. The change of the peak current ($i_{p,acv}$) of H_2N-$(CH_2)_4$-CO-Ala-Ala-Asn-Leu-NH-CH_2-Fc immobilized on a VACNF NEA in continuously repeated ACV measurements while 9.8 ng μL^{-1} (338 nM) activated cathepsin B in 25 µL of activation buffer consisting of 5 mM DTT and 25 mM MES (pH 5.0) was added into the electrochemical cell containing 250 µL of 25 mM MES (pH 5.0).

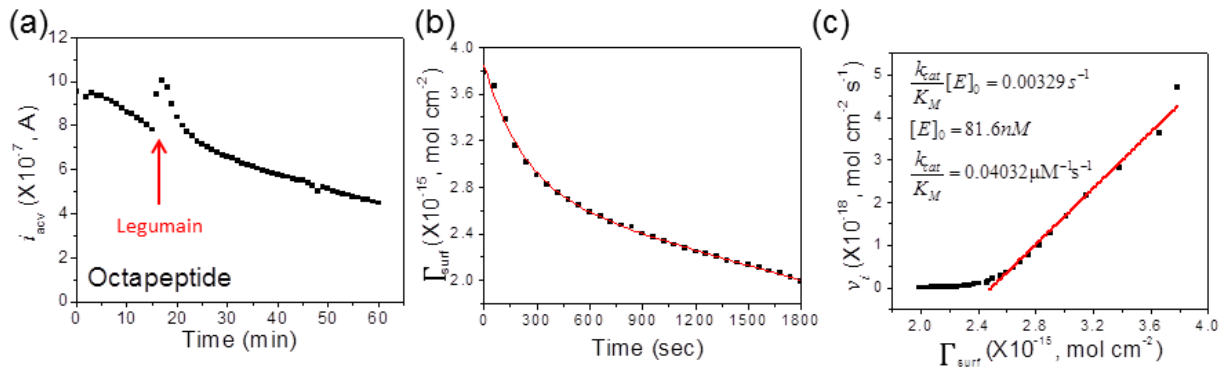

Figure A.15 (a) The change of the peak current ($i_{p,acv}$) of octapeptide H_2N-$(CH_2)_4$-CO-Pro-Ala-Ala-Asn-Leu-Ile-Arg-Leu-NH-CH_2-Fc immobilized on a VACNF NEA in continuously repeated

ACV measurements while 90.9 ng μL^{-1} (1.90 μM) legumain in the activation buffer consisting of 50 mM CH_3COONa (pH = 4.0, adjusted by adding acetic acid) and 100 mM NaCl was added into the electrochemical cell containing 250 μL of 50 mM MES (pH 5.0) and 250 mM NaCl. ACV measurements were carried out at f = 1750 Hz and AC voltage amplitude V_0 = 150 mV. (b) Replot of the data presented in figure (a) showing the reduction of the quantity of surface adsorbed Fc (i.e. Γ_{surf}) during enzymatic cleavage of the octapeptide after adding the legumain. (c) Plot of the reaction rate (v_i) versus the quantity of surface adsorbed Fc (Γ_{surf}) during the enzymatic reaction.

Verification of the inactivity of the guanidine NH function of arginine residue of Boc-HN-$(CH_2)_4$CO-Leu-Arg-Phe-Gly-$NHCH_2$-Fc.

The following reaction has been carried out to verify that the guanidine NH function of arginine residue of Boc-HN-$(CH_2)_4$CO-Leu-Arg-Phe-Gly-$NHCH_2$-Fc does not form amide bond with the carboxylic function on carbon nanofibers. To a 1 mL aqueous solution of Boc-HN-$(CH_2)_4$CO-Leu-Arg-Phe-Gly-$NHCH_2$-Fc (3 mg, 3.4 μmol), benzoic acid (0.4 mg, 3.4 μmol), and *N*-hydroxysuccinimide (0.4 mg, 3.4 μmol) was added with 1-ethyl-3-(3-dimethylaminopropyl)carbodiimide hydrochloride (0.66 mg, 3.4 μmol), and the resulting solution was stirred at room temperature for 2 hours. Mass spectrometry analysis showed that no reaction took place between the NH group of arginine residue and the carboxylic acid moiety of benzoic acid. Boc-HN-$(CH_2)_4$CO-Leu-Arg-Phe-Gly-$NHCH_2$-Fc remained unchanged. The test suggested that the NH moieties in the side chain of arginine residue does not react with the carboxylic acid function of carbon nanofibers. The most likely route for the peptide to be attached to the VACNF NEA is by forming the amide bond through the $-NH_2$ group at the distal end of the linker.

Appendix B - Supporting Information for Chapter 4

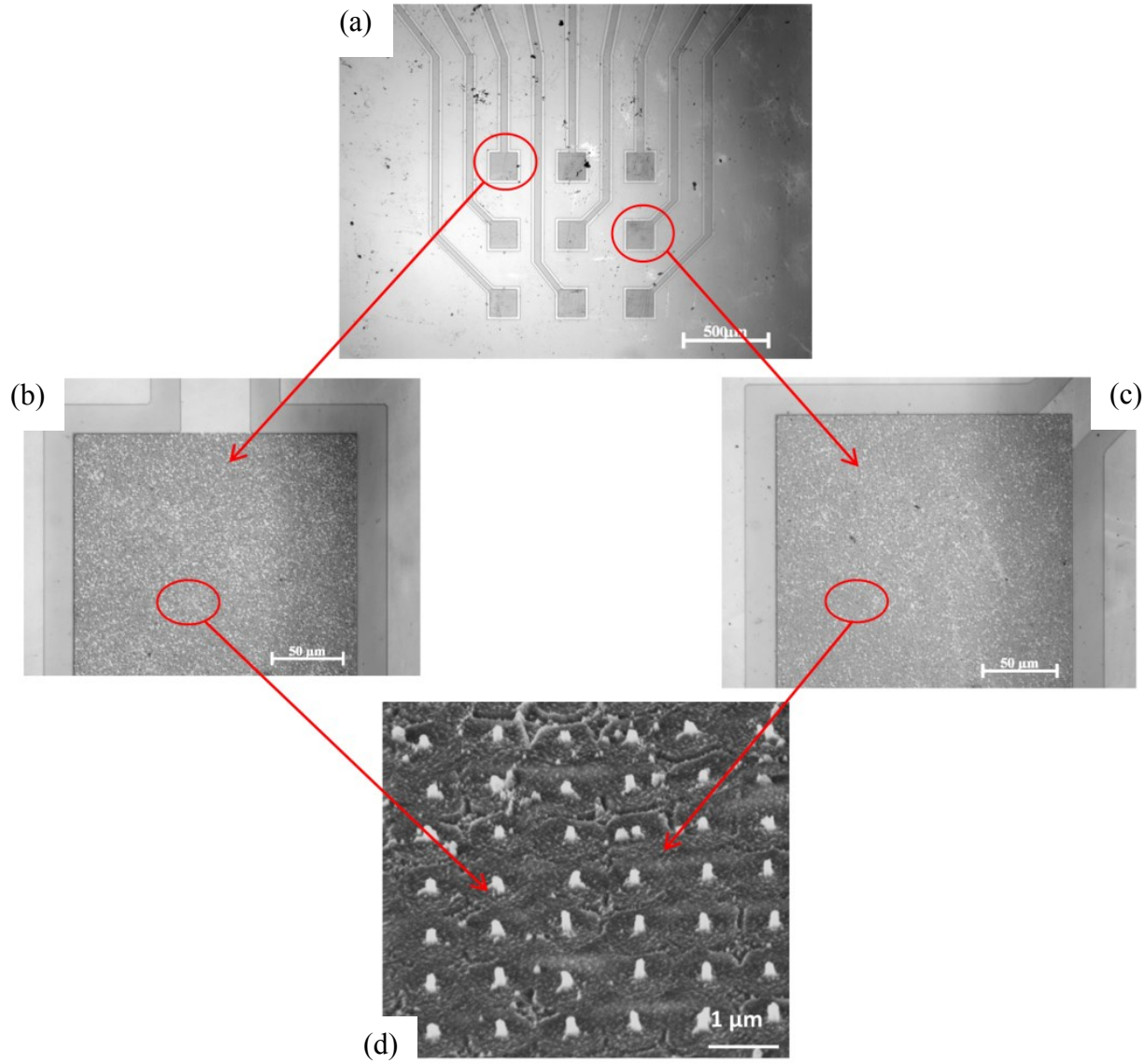

Figure B.1 Bright field microscope images of patterned VACNF NEAs with (a) using a 4x objective lens, (b) and (c) using a 50x objective lens. (d) Field-emission scanning electron microscopy image at 45° perspective view of the patterned VACNF NEAs. The scale bars are 500, 50, 50, and 1 µm, respectively.

Table B.1 The fitting parameters of the ACV signal $i_{p,acv}$ vs. the reaction time t corresponding to Fig. 1E–G after the cathepsin B solution at different concentrations were added to the electrochemical cell.

[Cathepsin B] (nM)	Fitting Equation: $i_t = i_0 \exp(-t/\tau) + bt + c$			
	i_0 (A)	b (A/s)	c (A)	τ (s)
15.5	6.69×10^{-7}	-4.12×10^{-11}	8.11×10^{-7}	2935
30.7	8.35×10^{-7}	-3.33×10^{-11}	1.03×10^{-7}	1287
62.1	7.22×10^{-7}	-4.55×10^{-11}	4.35×10^{-7}	448

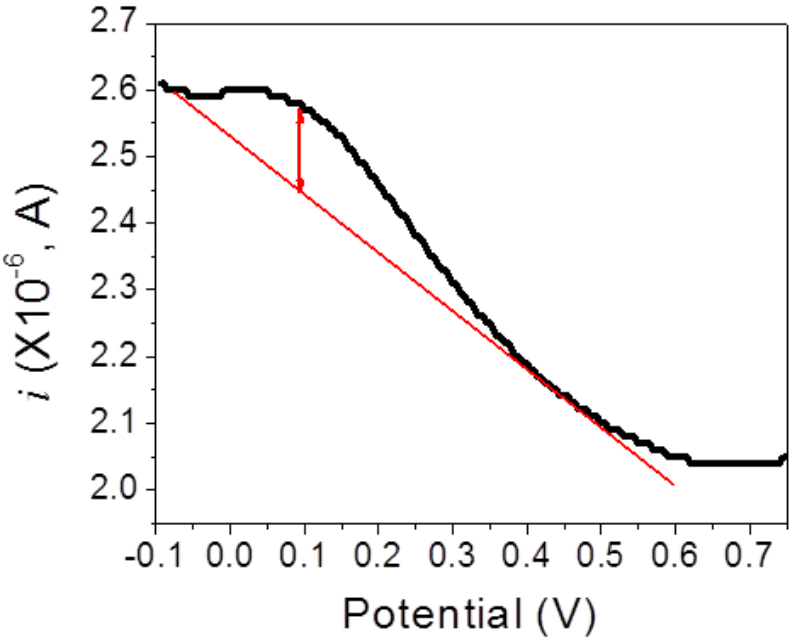

Figure B.2 ACV of a random VACNF NEA after being soaked in the solution of 1.0 mM H_2N-$(CH_2)_4$-CO-Leu-Asn-Phe-Gly-NH-CH_2-Fc for 2 hr.

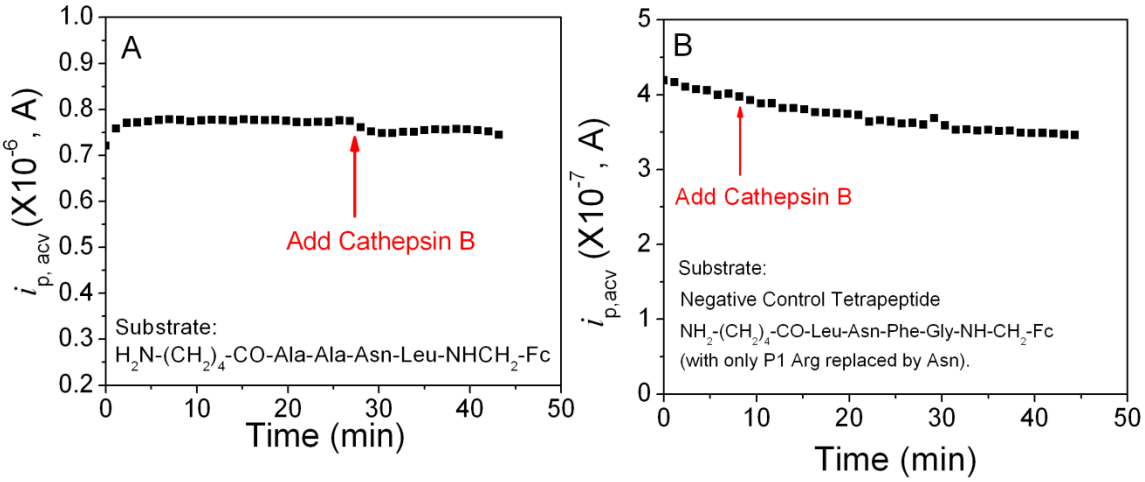

Figure B.3 Negative control experiments. (A) activated cathepsin B added to non-relevant tetrapeptide substrate H_2N-$(CH_2)_4$-CO-Ala-Ala-Asn-Leu-NH-CH_2-Fc. (B) activated cathepsin B added to modified tetrapeptide H_2N-$(CH_2)_4$-CO-Leu-Asn-Phe-Gly-NH-CH_2-Fc where the cleavage site Arg was replaced with Asn. All tetrapeptides were covalently attached to the exposed CNF tips in random VACNF NEAs and the proteolyses were measured with continuously repeated ACV measurements. In (A) and (B), 25 μL of 9.8 ng·μL^{-1} (338 nM) *activated* cathepsin B in the activation buffer consisting of 5 mM DTT and 25 mM MES (pH 5.0) was added into the electrochemical cell containing 250 μL of 25 mM MES (pH 5.0). The final cathepsin B concentration was 30.7 nM. ACV measurements were carried out at f = 800 Hz with the AC voltage amplitude V_0 = 150 mV.

Table B.2 Comparison of k_{cat}/K_M values of cathepsin B from literatures and our electrochemical method.

Methods	Substrate	Resources	k_{cat}/K_M ($M^{-1}s^{-1}$)
ACV	H_2N-$(CH_2)_4$-CO-L-R-F-G-NH-CH_2-Fc	Our manuscript	$(3.68 \pm 0.05) \times 10^4$
Fluorescence	Z-L-R-AMC	R & D system	1.2×10^5
FRET	Abz-GIVRAK(Dnp)-OH	Anal. Biochem. (2004), 335(2), 244-252.	7.288×10^6
Fluorescence	Abz-FSQPMKRLTLGNTTQ-EDDnp	Hypertension (2000), 35(6), 1278-1283.	7.5×10^4
Fluorescence	Abz-AFRSAAQ-EDDnp	Biochem. (1997), 36(41), 12608-12615.	$(1.95 \pm 0.05) \times 10^3$
Fluorescence	Abz-QVVAGA-EDDnp	Biochem. (1997), 36(41), 12608-12615.	$(3.0 \pm 0.2) \times 10^4$
Fluorescence	Cbz-FR-AMC	Biochem. (1997), 36(41), 12608-12615.	$(4.25 \pm 0.3) \times 10^5$
Fluorescence	Boc-Val-Leu-Lys-AMC	J. Agri. & Food Chem. (1996), 44(3), 774-8.	1.5×10^6
Fluorescence	Abz-QVVA-EDDnp	Protein. Chem. (1995) 14, 645-653	2.4×10^4
Fluorescence	Abz-QVVAG-EDDnp	Protein. Chem. (1995) 14, 645-653	2.5×10^4
Fluorescence	Abz-QVVAGG-EDDnp	Biochem. J. (1996), 313(3), 951-6.	6×10^3
Fluorescence	Abz-QVVAGP-EDDnp	Biochem. J. (1996), 313(3), 951-6.	5×10^3
Fluorescence	Abz-LVGGP-EDDnp	Biochem. J. (1996), 313(3), 951-6.	1.7×10^4
Fluorescence	Abz-VVGGP-EDDnp	Biochem. J. (1996), 313(3), 951-6.	5.4×10^4
Fluorescence		J. Enzyme Inhibition (1992), 6(3), 181-94.	5×10^3
Fluorescence	Z-F-R-pNA	Biochem. J. (1992), 285(2), 427-34.	$(5.460 \pm 0.116) \times 10^4$
Fluorescence	Z-R-R-pNA	Biochem. J. (1992), 285(2), 427-34.	$(1.480 \pm 0.069) \times 10^4$

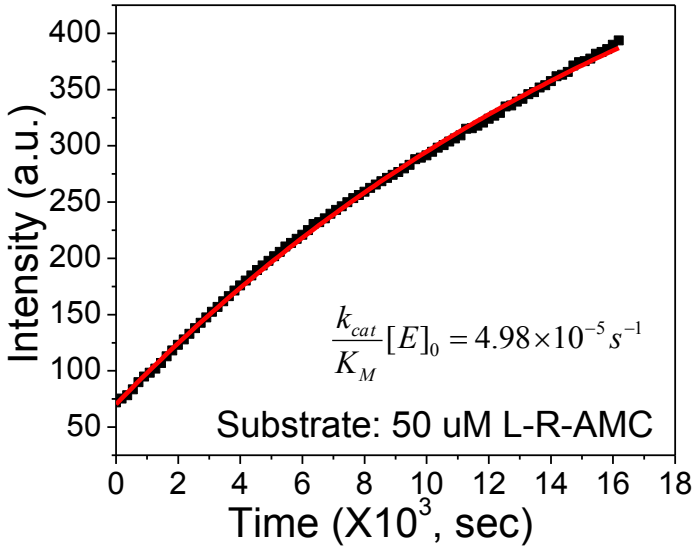

Figure B.4 The kinetic curve of the fluorescence intensity of 50 µL of 0.48 mg·mL^{-1} *activated* human breast whole tissue lysate (adult normal) reacting with 50 µL of 100 µM peptide substrate Z-Leu-Arg-AMC in 25 mM MES (pH 5.0). The final tissue lysate concentration was 0.24 mg·mL^{-1}.

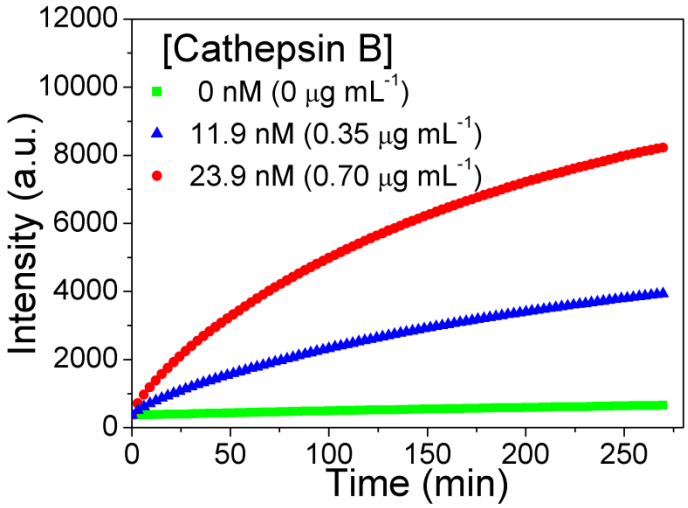

Figure B.5 The kinetic curve of the fluorescence intensity of 0.25 mg·mL^{-1} human breast whole tissue lysate (adult normal) spiked with different concentrations of activated purified cathepsin B reacting with 100 µM substrate Z-Leu-Arg-AMC in 25 mM MES (pH 5.0). The final purified

cathepsin B concentrations were 0 μg·mL^{-1} (light green), 0.35 μg·mL^{-1} (11.9 nM) (blue) and 0.70 μg·mL^{-1} (23.9 nM) (red), respectively.

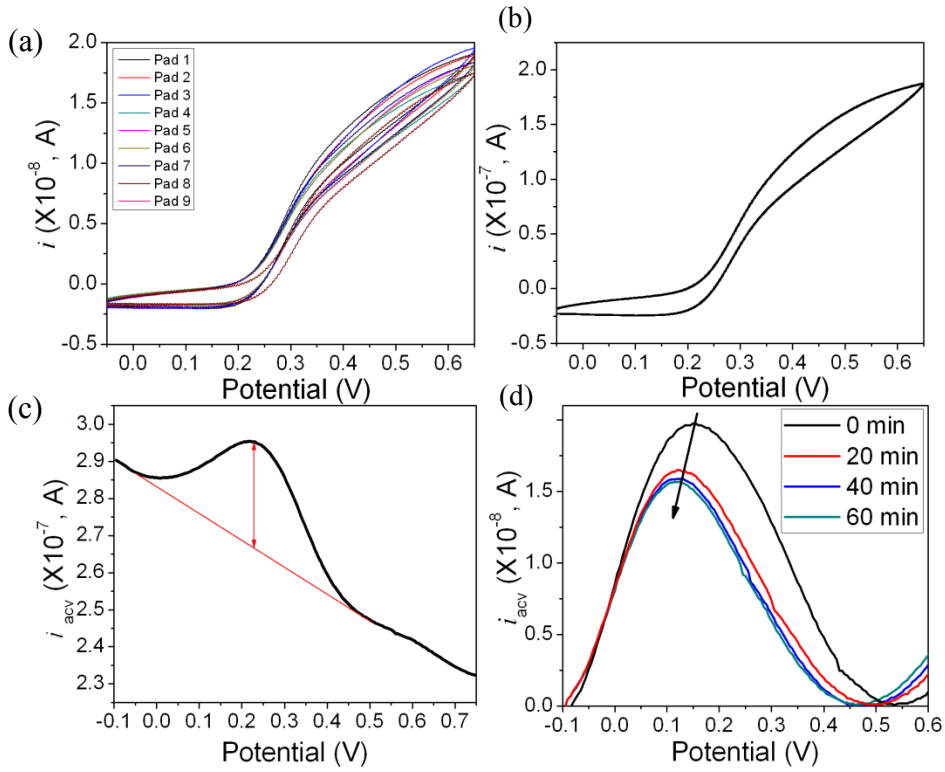

Figure B.6 (a) CV of the patterned VACNF NEAs on each single microelectrode pads. (b) CV of patterned VACNF NEAs with all nine microelectrode pads connected together. The measurements were done in 50 mM $K_3Fe(CN)_6$ and 1.0 M KCl electrolyte at a scan rate of 50 mV·s^{-1}. (c) The average ACV curve from the regular VACNF NEA on a single 200 μm x 200 μm microelectrode pad with the tetrapeptide H_2N-$(CH_2)_4$-CO-Leu-Arg-Phe-Gly-NH-CH_2-Fc covalently functionalized on the exposed CNF tips. The electrochemical cell was filled with 250 μL of 25 mM MES (pH 5.0). (d) Four representative background-subtracted ACV curves measured at 0 (black), 20 (red), 40 (blue) and 60 min (green) after 25 μL of activated purified cathepsin B was added into the electrochemical cell. The final concentration of cathepsin B in

the cell was 30.7 nM (0.9 ng·μL^{-1}). All ACV measurements were carried out at f = 800 Hz and AC voltage amplitude V_0 = 150 mV.

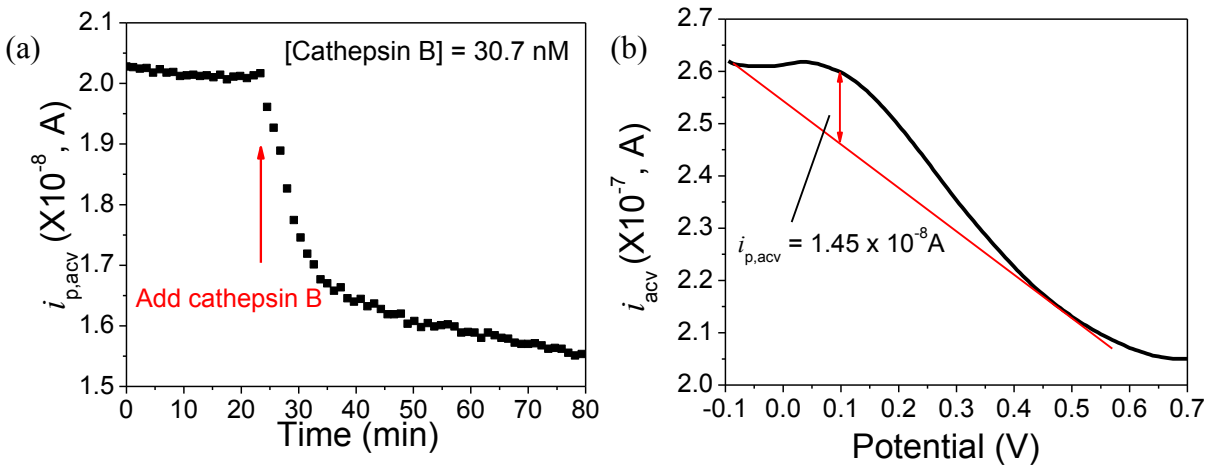

Figure B.7 (a) The kinetic ACV peak current $i_{p,acv}$ of H_2N-$(CH_2)_4$-CO-Leu-Asn-Phe-Gly-NH-CH_2-Fc functionalized at the patterned VACNF NEA on a single 200 μm x 200 μm microelectrode pad versus the reaction time after 30.7 nM cathepsin B was added into the electrode chemical cell. (b) ACV from an e-beam patterned VACNF NEA on a single microelectrode pad which was soaked in 1.0 mM H_2N-$(CH_2)_4$-CO-Leu-Asn-Phe-Gly-NH-CH_2-Fc solution for 2 hr without forming covalent bonds. The faradaic signal from the physically trapped Fc moieties was significant.

Appendix C - Supporting Information for Chapter 5

Cell lines and correlation with cancer stages

The selected cell lines were used in representing different stages of cancer formation. Human mammary epithelial cells (HMEC), obtained from Lonza (Annandale, NJ, USA), are primary cells, derived from adult female breast tissue. HMECs are positive for cytokertins 14 and 18 and negative for cytokeratin 19. MCF-10A cell line, obtained from American Type Cell Culture (ATCC) (Manassas, MA, USA), is a non-tumorigenic epithelial cell line derived from a 36 year old female. These cells have no signs of terminal differentiation or senescence. They respond to insulin, epidermal growth factor (EGF), and glucocorticoids. T47D cell line, obtained from ATCC, was isolated by I. Keydar from a pleural effusion obtained from a 54 year old female patient with an infiltrating ductal carcinoma of the breast. MDA-MB-231 cell line, obtained from ATCC, was isolated from a metastatic site of a 51 year old female patient with breast adenocarcinoma.

Western blot and immunoprecipitation of cancer cell lysates

Cells were harvested and lysed in lysis buffer (20 mM Tris pH 7.5, 0.5 mM EDTA, 0.5 mM EGTA, 0.5% Triton X-100) at 1:1,000 dilution of protease inhibitors (Sigma-Aldrich, Saint Louis, MO, USA). Whole-cell extract (25 μg) was resolved by 10% SDS-PAGE and transferred to nitrocellulose membrane (Midwest Scientific, Saint Louis, MO, USA) that was blocked in 5% milk for an hour at room temperature and then incubated with monoclonal antibodies (1:1,000). Western blots were detected by enhanced chemiluminescence detection reagents (Pierce, Rockford, IL, USA) and visualized by Fluorchem E imaging system (ProteinSimple, Santa Clara, CA, USA).

The procedure for obtaining whole-cell extract (WCE) for immunoprecipitation (IP) was the same as that in Western blotting. First, 500 μg WCE was pre-cleared with 20 μL of protein A/G-agarose beads from Santa Cruz Biotechnology (Santa Cruz, CA, USA) for 30 minutes. Then, the mixture was centrifuged at 2,000 rpm for 5 minutes. The supernatant was collected and incubated with the primary antibody of cathepsin B (1:1000, giving the total amount of 1.4 μg) from Santa Cruz Biotechnologies (Santa Cruz, CA, USA) overnight at 4ºC. Twenty μl of protein A/G-agarose beads was added and incubated for additional 2 h at 4ºC on a rocker. Samples were centrifuged at 2,000 rpm for 5 minutes and pellet (A/G-agarose complex) was washed three times with lysis buffer (20 mM Tris pH 7.5, 0.5 mM EDTA, 0.5 mM EGTA, 0.5% Triton X-100). Samples were run on 10% SDS-PAGE and immunoblotted with cathepsin B as described in Western blot analysis. In case of multiple steps of IP, samples were incubated with cathepsin B antibodies for 2 or 3 times prior to Western blot analysis. This repeated step allows the complete removal of cathepsin B in whole cell lysate. Intensities of the bands were digitized using Un-Scan-It software (Silk Scientific Inc., Orem, Utah, USA). The supernatant after the IP procedure was used in some proteolysis experiments as a blank control.

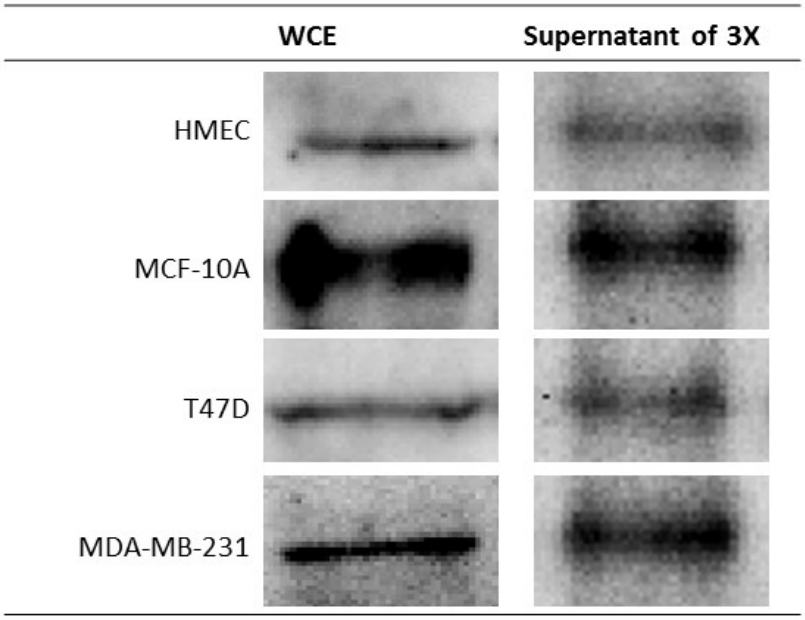

Figure C.1 Western blot analysis of actin in four types of breast cell lysates. Whole cell extract and supernatant after three rounds of immunoprecipitation showed a detection of actin at 43 kDa.

Table C.1 Integrated pixel intensity obtained from Western blot of 0.5 mg pellet collected from immunoprecipitation of the whole cell extracts. The proenzyme cathepsin B is ~ 37 kDa and the active cathepsin B is ~ 25 kDa.

	Integrated Pixel Intensity		
Cell Line	37 kDa	25 kDa	Total
HMEC	1766956	1293768	3060724
MCF-10A	1778380	1291818	3070198
T47-D	1765820	1589108	3354928
MDA-MB-231	2701916	1137183	3839099

(a)

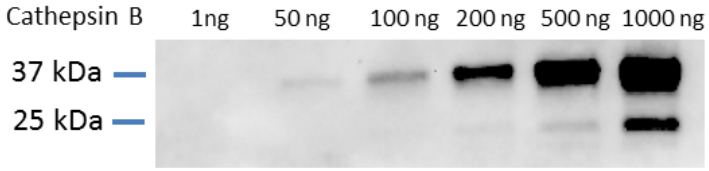

(b)

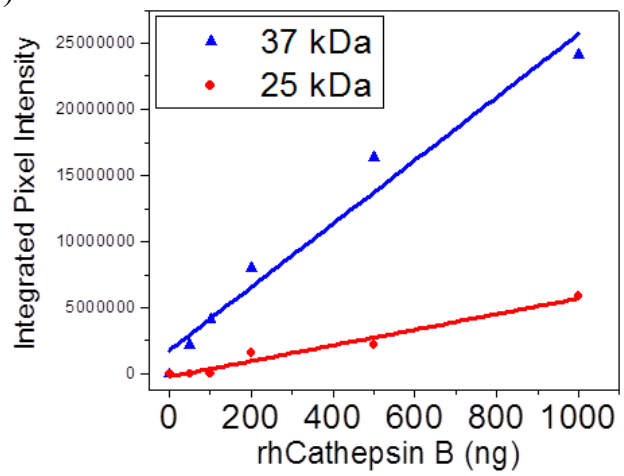

Figure C.2 (a) Western blot of different amount of purified recombinant cathepsin B using 1.4 µg of cathepsin B antibody. The proenzyme cathepsin B is ~ 37 kDa and the active cathepsin B is ~ 25 kDa. (b) Plot of integrated pixel intensity from both bands versus the amount of cathepsin B.

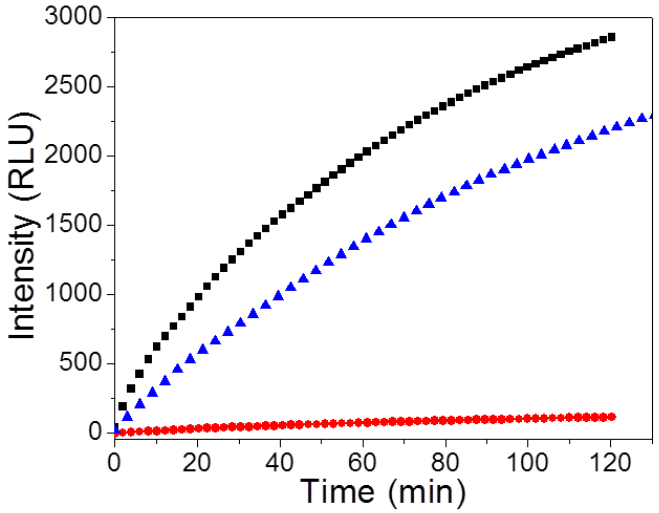

Figure C.3 The kinetic curves of the fluorescence intensity during proteolysis of Z-Leu-Arg-AMC in 25 mM MES (pH 5.0) with 0.05 ng·μL^{-1} purified cathepsin B after (1) normal activation procedure by incubation in activation buffer 15 min (blue triangle); (2) normal activation followed by 30 min additional incubation (black square); and (3) adding 0.6 μM inhibitor GC373 during the 30 min additional incubation period (red dot). The final concentrations of the substrate are 50 μM and all incubation was at room temperature.

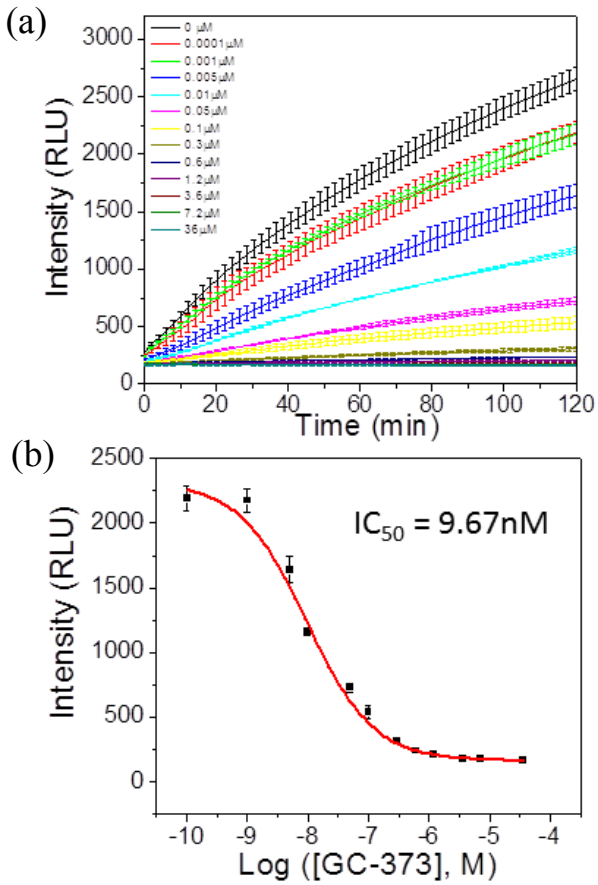

Figure C.4 (a) The kinetic curves of the fluorescence intensity during proteolysis of 50 μM Z-Leu-Arg-AMC in 25 mM MES (pH 5.0) with 0.05 ng·μL^{-1} purified cathepsin B which inhibited by inhibitor GC-373 in different concentrations. The final concentrations of the inhibitor are varied from 0 to 36 μM. (b) IC_{50} curve of the inhibitor GC-373. The vertical axis represents the

fluorescence intensity (in relative light unit) at 120 min at each inhibitor concentration. The IC_{50} value of GC-373 was determined to be 9.7 nM by fitting the IC_{50} curve with the dose response function $y = A_1 + (A_2 - A_1)/(1 + 10\text{^}((LOGx_0 - x)*p))$, where the fitting parameter $LOGx_0$ represents the value of $\log(IC_{50})$.

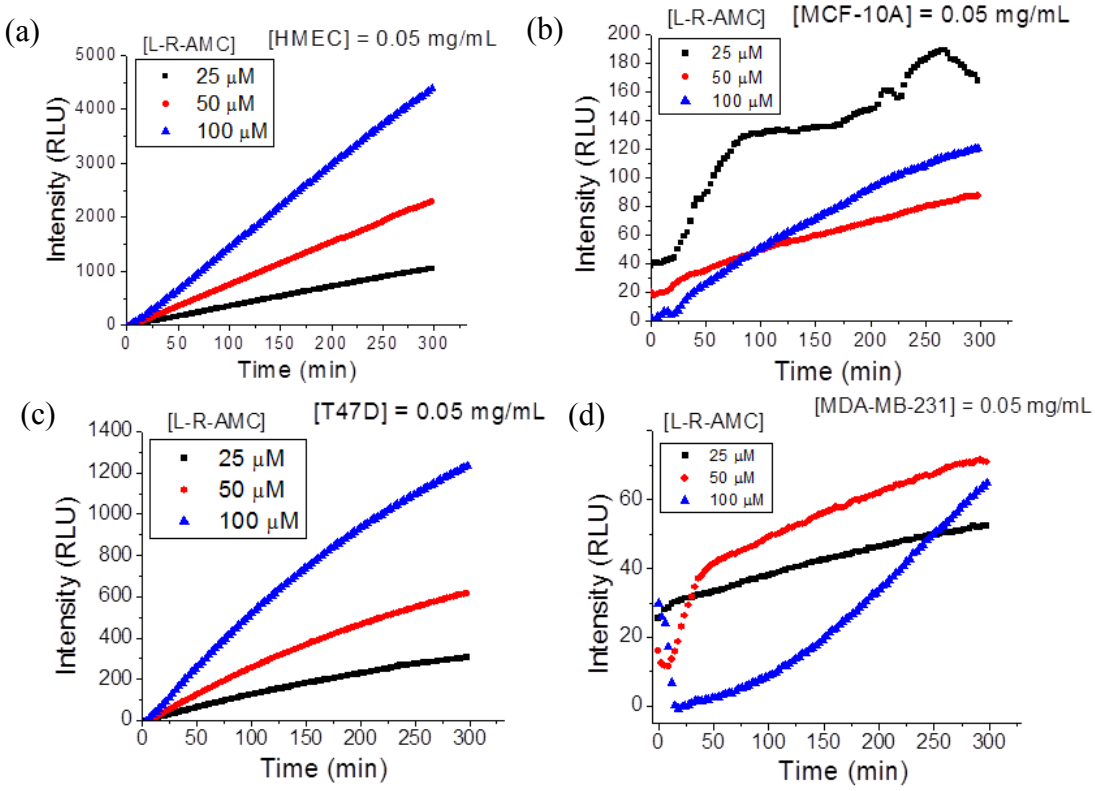

Figure C.5 The kinetic curves of the fluorescence intensity during proteolysis of Z-Leu-Arg-AMC in 25 mM MES (pH 5.0) with 0.05 mg·mL^{-1} human mammary epithelial cells (HMEC), transformed breast cells (MCF-10A), breast cancer cells (T47D and MDA-MB-231). The final concentrations of the substrate are 25 μM (black), 50 μM (red) and 100 μM (blue), respectively.

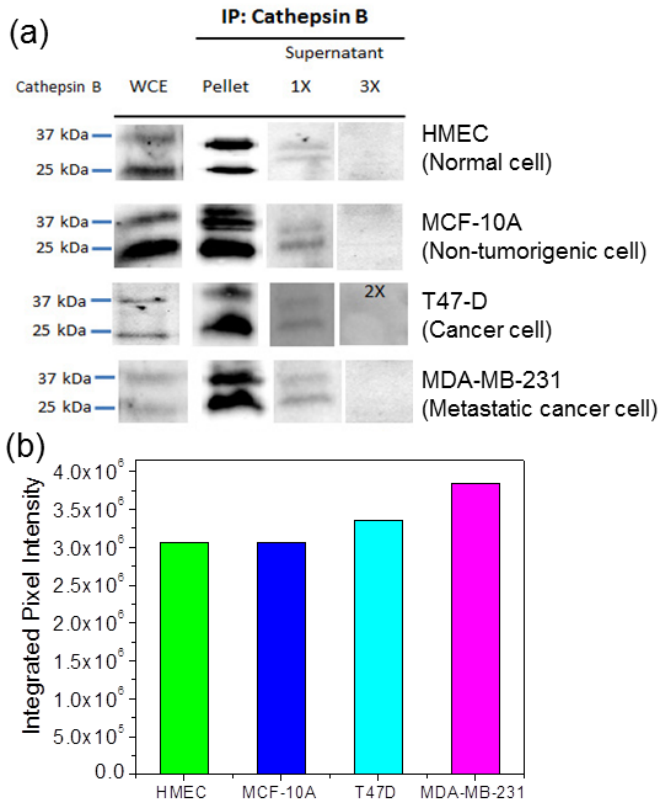

Figure C.6 (a) Western blot analysis of cathepsin B expression in four types of breast cells: Normal breast cells (HMEC), transformed breast cells (MCF-10A), breast cancer cells (T47D), and metastatic breast cancer cells (MDA-MB-231). The first column shows that the whole cell extract (WCE) of all 4 types of cells consist both proenzyme (~ 37 kDa) and active (~ 25 kDa) cathepsin B. (Note that the experimental conditions were varied and thus this set of data is only for qualitative assessment). About 0.5 mg of WCE was used for immunoprecipitation (IP) assay with 1.4 µg of cathepsin B antibody. The immunoprecipitated fraction was subjected to Western blot analysis using cathepsin B antibody. Pellet includes pulldown complex with cathepsin B antibody. Supernatant with one round of immunoprecipitation denotes as 1X and supernatant with two and three rounds of immunoprecipitation denotes as 2X and 3X, respectively. (b) The quantitative cathepsin B expression represented by the total integrated pixel intensity of

cathepsin B bands in a set of Western blot analyses under the same conditions from the same HMEC, MCF-10A, T47D, and MDA-MB-231 cell lysate loading. The cathepsin B level increased in cancer cell lysates.

Appendix D - ELISA Results of Breast Cell Lysates

Quantikine® ELISA kit of human pro-cathepsin B was purchased from R&D systems (Minneapolis, MN, USA).

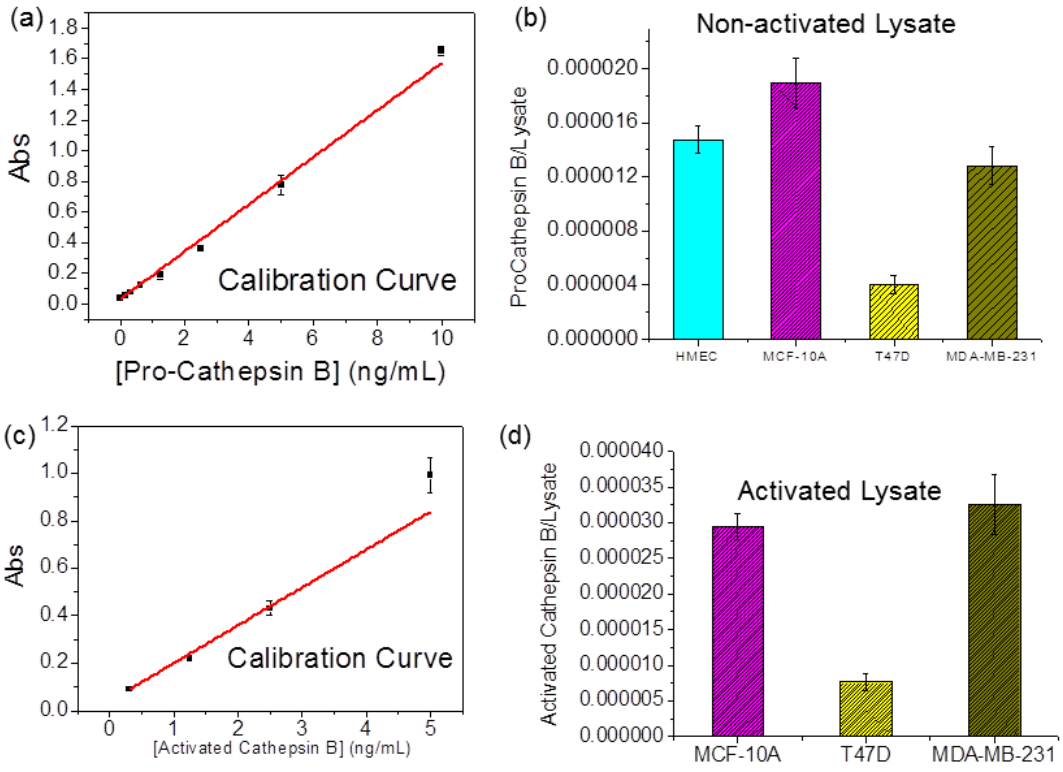

Figure D.1 Calibration curve of absorbance vs the concentration of (a) pro-cathepsin B and (c) activated cathepsin B. (b) Bar graph of mass percentage of procathepsin B in the breast cell lysates from HMEC, MCF-10A, T47D and MDA-MB-231, based on the calibration curve in (a). (d) Bar graph of mass percentage of activated cathepsin B in the breast cell lysates from MCF-10A, T47D and MDA-MB-231, based on the calibration curve in (c).

Appendix E - Chemiluminescence Measurement Using Built-in-House Handheld Luminometer

All the chemiluminescence experiments using built-in-house luminometer was conducted by Dr. Jianwei Liu, Cas LeMaster and Caleb Christainson from professor Judy Wu's lab in Department of Physics and Astronomy, University of Kansas.

The miniaturized luminometer is comprised of a small metal box (approximately 10 cm x 20 cm) containing a TEFLON sample well with integrated 30-fiber bundle optical fiber (Figure B.1). The sample solution is injected through the opening on the top of the box by a pipette. The detector is a head-on PMT for photo counting. The spectral range is from 350 to 650 nm and the peak wavelength is at 420 nm. The detection limit of the PMT is 3 x 10^{-21} mol of luciferase or 1 x 10^{-18} mol of ATP.

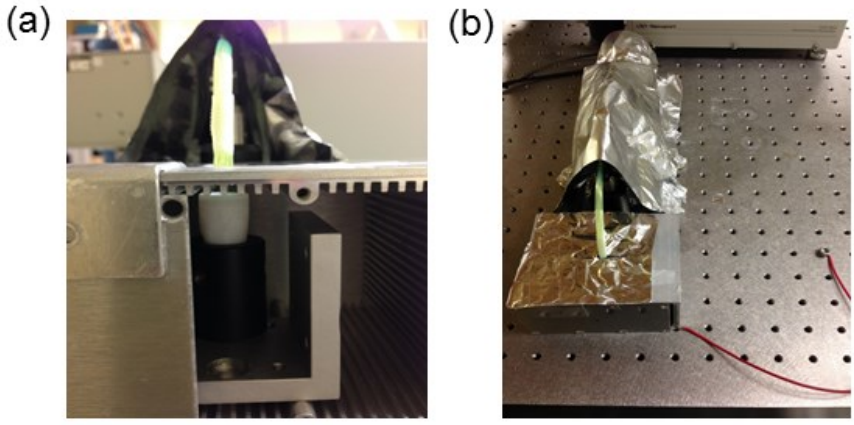

Figure E.1 (a) Optical fiber bundle inserts into the opening on the top of the metal dark box to collect the photons from the reaction in the TEFLON sample well. (b) The overall view of the setup of the built-in-house luminometer.

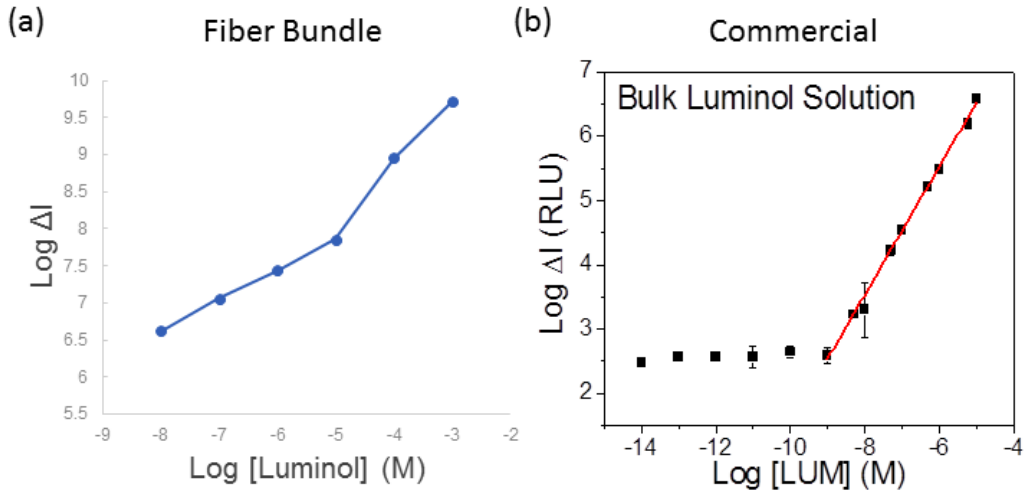

Figure E.2 Calibration curves of the background-subtracted chemiluminescence signal vs. the concentration of bulk luminol solution using (a) optical fiber bundles and (b) commercial luminometer.

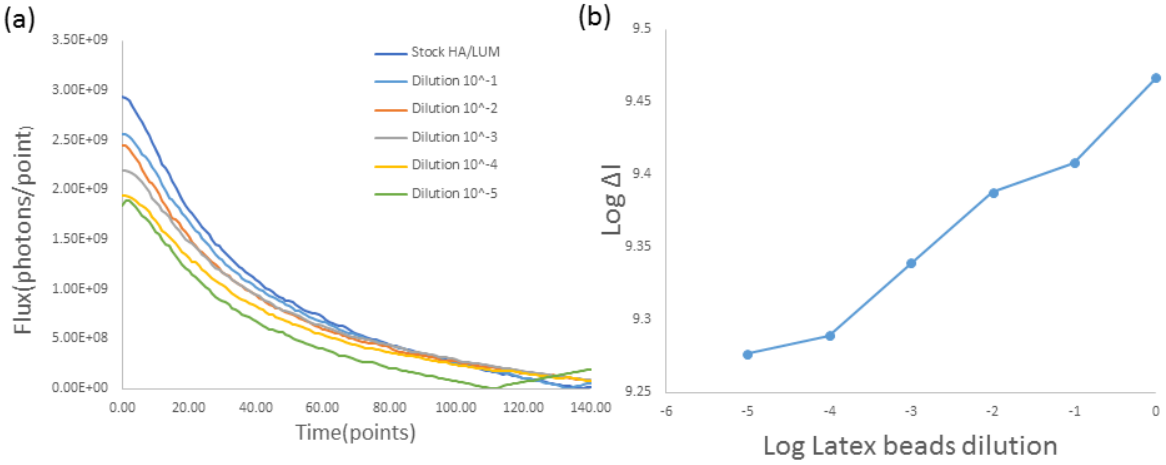

Figure E.3 (a) The kinetic CL measurements with luminol and HA target DNA-attached latex beads (latex beads-HA target/LUM) solution at varied concentrations using built-in-house luminometer. (b) The background-subtracted chemiluminescence signal vs. the concentration of latex beads-HA target/LUM solution. About 50 µL of 0.10 M NaOH, 50 µL of 1.41 M H_2O_2 and 50 µL of 1.0 mM $K_3Fe(CN)_6$ solution were preloaded in a TEFLON well. Then 50 µL of latex

beads-HA target/LUM solution with varied concentration was added using a pipette to initialize the CL reaction. The concentration of the stock solution is 4.75×10^{10} mL^{-1} (stock HA/LUM). Dilution 10^{-1} to dilution 10^{-5} corresponds to concentration from 4.75×10^{9} mL^{-1} to 4.75×10^{5} mL^{-1}.

Appendix F - List of Publications and Presentations

Publications

1. Li, J.; Madiyar, F. R.; Swisher, L. Z., Carbon Nanomaterials with special architectures for biomedical applications. *Carbon Nanomaterials for Biomedical Applications*, editors Liming Dai, Rajesh Naik, Mei Zhang, Springer, Submitted.
2. Swisher, L. Z.; Prior, A. M.; Gunaratna, M. J.; Shishido, S.; Madiyar, F. R.; Nguyen, T. A.; Hua, D. H.; Li, J., Quantitative Electrochemical Detection of Cathepsin B Activity in Breast Cancer Cell Lysates Using Carbon Nanofiber Nanolelectrode Arrays toward Identification of Cancer Formation. *Nanomedicine: NBM*, under review.
3. Madiyar, F. R.; Bhana, S.; Swisher, L. Z.; Huang, X.; Culberson, C.; Li, J., Integration of Nanostructured Dielectrophoretic Device and Surface-Enhanced Raman Probe for Highly Sensitive Rapid Bacteria Detection. *Nanoscale*, **2015**, *7*, 3726-3736.
4. Swisher, L. Z.; Prior, A. M.; Nguyen, T. A.; Hua, D. H.; Li, J., Quantitative Electrochemical Detection of Cathepsin B Activity in Complex Tissue Lysates Using Enhanced AC Voltammetry at Carbon Nanofiber Nanoelectrode Arrays. *Biosens. Bioelectron.*, **2014**, *56*, 129-136. (Highlighted in *Global Medical Discovery*, Aug. 2014)
5. Lu, J.; Maezawa, I.; Weerasekara, S.; Erenler, R.; Nguyen, T.; Nguyen, J.; Swisher, L. Z.; Li, J.; Jin, L.; Ranjan, A.; Srivastava, S.; Hua, D. H., Syntheses, Neural Protective Activities, and Inhibition of Glycogen Synthase Kinase-3β of Substituted Quinolines. *Bioorg. Med. Chem. Lett.*, **2014**, *24*, 3392-3397.
6. Swisher, L. Z.; Syed, L. U.; Prior, A. M.; Madiyar, F. R.; Carlson K. R.; Nguyen, T. A.; Hua, D. H.; Li, J., Electrochemical Protease Biosensor Based on Enhanced AC

Voltammetry Using Carbon Nanofiber Nanoelectrode Arrays. *J. Phys. Chem. C*, **2013**, *117*, 4268-4277.

7. Syed, L. U.; Swisher, L. Z.; Huff, H.; Rochford, C.; Wang, F.; Liu, J.; Wu, J.; Richter, M.; Balivada, S.; Troyer, D.; Li, J., Luminol-Labeled Gold Nanoparticles for Ultrasensitive Chemiluminescence-based Chemical Analyses. *Analyst*, **2013**, *138*, 5600-5609. (Featured article)
8. Li, J.; Li, Y.; Swisher, L. Z.; Syed, L. U.; Prior, A. M.; Nguyen, T. A.; Hua, D. H., *Proc. SPIE* on Biosensing and Nanomedicine V, pp. 84600L, SPIE, San Diego, CA, **2012**a.

Presentations

POSTER

Swisher, L. Z.; Syed, L. U.; Prior, A. M.; Carlson, K.; Nguyen, T. A.; Hua, D. H.; Li, J. (2011); "Real-time Electrochemical Monitoring of Cancerous Protease Activity Using Nanoelectrode Arrays". Research and the State, Graduate Student Poster Session, Kansas State University, Manhattan, KS.

ORAL

1. Syed, L. U.; Swisher, L. Z.; Prior, A. M.; Hua, D. H.; Li, J. (2011); "Real-Time AC Voltammetry Based Detection of Cancerous Protease (Legumain) Using Nanoelectrode Arrays". Abstracts, 46th Midwest Regional Meeting of the American Chemical Society, St Louis, MO.

2. Syed, L. U.; Swisher, L. Z.; Prior, A. M.; Hua, D. H.; Li, J. (Fall-2011); “High-Performance Electrochemical Sensing of Cancerous Protease (Legumain) Using Nanoelectrode Arrays”. Abstracts, Materials Research Society, Boston, MA.